Soft-templating Sol-gel Synthesis of Multifuctional Metal Oxide Nanoparticles

연질 주형법을 이용한 다기능성 금속산화물
나노입자의 졸−겔 합성

2013년 2월

서울대학교 대학원

화학생물공학부

오 명 환

Abstract

Soft-templating Sol-gel Synthesis of Multifuctional Metal Oxide Nanoparticles

Myoung Hwan Oh

School of Chemical and Biological Engineering

The Graduate School

Seoul National University

Significant progress has been made in the synthesis of metal oxide nanoparticles using solution-based approaches. The broadened scope in the synthesis with control over size, structure, morphology and composition, endows the nanoparticles with versatile and exclusive properties as compared to their bulk counterparts. Sol-gel chemistry has been recognized as the most affordable and fundamental tool to carryout conversion of metal precursors into metal oxide nanoparticles, which is generalized to nanoparticles of nearly all transition metals.

However, for the fine-tuning of the microstructures, chemical, physical, and technical modulations are required in the sol-gel process. For example, nonaqueous sol-gel chemistries were proposed to control nucleation and growth rate of oxide nanoparticles, while soft-template method using amphiphilic molecules either as unit of organic assembly or as structure directing agent was employed to restrict the growth of metal oxides at the nanoscale.

Aqueous phase sol-gel reactions have difficulties in the synthesis of uniform-sized oxide nanoparticles. The inorganic polymerizations induced by water are too fast to restrict irreversible flocculation or to stall oligomerization during the growth process. Consequently various nonaqueous sol-gel routes have been used to synthesize uniform-sized oxide nanoparticles in large scale. However, aqueous sol-gel routes, which employ low reaction temperature and are consequently cost-effective, are more facile and environment friendly to synthesize metal oxide nanoparticles. Furthermore unique solvating property of water offers advantages in the preparation of homogeneous synthetic solution and high-yield production of ionic crystals. Furthermore, in aqueous media, reduction and oxidation potentials can be tuned by acids, bases or dissolved oxygen, which are key factors to determine the

dissolution/precipitation of the metal oxide nanoparticles.

Semi-permeable soft-templates, which consist of amphiphilc molecules, can function as organic ligands, essential in both nonaqueous and aqueous sol-gel chemistry. These templates turn out to be very useful for synthesizing nanoparticles due to their wide availability, simple fabrication processes under mild conditions, and their easy removal with little damage to the final structures. Numerous kinds of ordered molecular aggregates such as microemulsions, vesicles, liquid crystals, and lipid nanotubes have been used as templates or structure directing agents to control the growth and assembly of inorganic materials. Due to their semi-permeable and semi-rigid property these templates can promote heterodeposition or dissolution at the nanoscale. Unique shapes and properties of templates with nanoscale dimensions enabled the synthesis of various functional nanomaterials by maintaining their structure at non-equilibrium state. The resulting nanomaterials with various structures including porous-, hollow-, core-shell-, york-shell-, and hetero-structures are promising candidates to be used as catalysts, energy materials, and in biomedicine.

In the present thesis, we have synthesized noble functional metal oxide nanoparticles by soft templating sol-gel routes. These oxide

nanomaterials have been successfully applied to multimodal biomedical contrast agents and lithium ion battery anodes. The synthetic procedures can be readily applied to large-scale production of uniform-sized oxide nanoparticles.

In Chapter 2, I report on facile and large-scale synthesis of uniform-sized tantalum oxide nanoparticles using microemulsion method and their successful applications to in vivo X-ray CT contrast agent for angiography and bimodal image-guided lymph-node mapping. Gram-scale synthesis of uniform-sized TaO_x nanoparticles was achieved using a simple microemulsion method. One-pot surface modification using various silane derivatives was successfully integrated to the microemulsion synthetic system, providing PEGylated and dye-immobilized TaO_x nanoparticles with anti-fouling and multimodal capabilities. In vivo X-ray CT imaging using RITC-conjugated and PEGylated TaO_x nanoparticles resulted in bright and well-resolved CT images with long circulation time. Time-course of histological studies and liver toxicity test revealed no adverse effect of the nanoparticles, possibly due to their bioinertness. Bimodal image-guided surgery using the particles was also advantageous in the resection of lymph nodes.

In Chapter 3, I report on the preparation of multifunctional

Fe_3O_4/TaO_x core/shell nanoparticles using microemulsion method and their application to biomodal CT/MR imaging. Multifunctional Fe_3O_4/TaO_x core/shell nanoparticles were synthesized using a sol-gel reaction of tantalum (V) ethoxide in a microemulsion containing Fe_3O_4 nanoparticles. The resulting nanoparticles were biocompatible and exhibited prolonged circulation time. When the nanoparticles were intravenously injected, the tumor-associated vessel and the microenvironment of the tumor were observed with computed tomography (CT) and magnetic resonance imaging (MRI), respectively.

In Chapter 4, I report on the synthesis of hollow nanoparticles of $Mn_3O_4/\gamma\text{-}Fe_2O_3$ and $\gamma\text{-}Fe_2O_3$ from the reaction of manganese oxide (Mn_3O_4) nanocrystals with iron(II) perchlorate. Owing to their non-equilibrium compositions and unique hollow structures, these hollow multimetallic oxide nanostructures showed excellent performance as anode materials for lithium ion batteries.

Keywords: sol-gel synthesis, metal oxide nanoparticles, soft-template, X-ray CT contrast agent, magnetic resonance imaging, lithium ion battery.

Student Number: 2010-31327

Contents

List of Tables

List of Figures

Chapter 1. Introduction: Synthetic Routes for Metal Oxide Nanoparticles

1.1 Nanochemistry of Metal Oxides

1.1.1 Metal Oxide Nanoparticles

Metal oxides are the most appealing candidates for functional nanomaterials both scientifically and techonologically. Metal oxides are one of the most diverse class of materials due to their unique properties covering almost all aspects of solid state physics. The large variety in their structures and associated properties have made them a primary research subject in solid state chemistry and still provides challenges for designing new materials. Their crystal structures range from simple rock salt to incommensurately modulated structures and the nature of the metal-oxygen bonding varies from nearly ionic to covalent or even metallic.[1] Due to such variation in structure and bonding, oxide materials possess a wide range of electronic and magnetic properties. Certain oxides such as RuO_2 or ReO_3 are metallic, whereas $BaTiO_3$ is an insulator. The magnetic properties found in oxides include ferromagnetic, ferrimagnetic, and antiferromagnetic behavior. Some

oxides possess switchable orientation states as observed in ferroelectric materials (e.g., titanates, niobates, or tantalates). Other attractive classes of materials within the oxide family include the cuprate superconductors and the manganites which display large magnetoresistance or multiferroics combining ferroelectricity and ferromagnetism (e.g., $BiFeO_3$ and $BiMnO_3$). Such exceptionally broad spectrum of properties makes metal oxides highly valuable in a broad range of applications such as in ceramics, electronics, biomedicine, energy conversion and storage, and catalysis.

1.1.2 Sol-gel Chemistry

Bulk metal oxides are most commonly synthesised by ceramic process. Although this process requires harsh conditions in order to obtain thermodynamically stable phases, it has been successfully used to produce various solid materials. However, compared to liquid phase routes in which highly sophisticated synthetic pathways are employed to promote chemical reactions, the ceramic method is a rather crude approach. Thus, liquid-phase routes represent the most promising alternative for the size- and shape-controlled synthesis of nanoparticles.

The liquid-phase synthetic routes enable a better control of structural, compositional, and morphological features of the nanoparticulate products. In contrast to solid-state processes, the liquid-state chemical processes allow synthesis of nanoparticles with well-defined and uniform morphologies.[2]

One of the representative liquid-phase processes for the synthesis of oxide nanoparticles is colloidal chemistry, which includes co-precipitation, hydrolytic and nonhydrolytic sol-gel route, hydro- and solvo-thermal method, template assisted method, and thermal decomposition.[3] Among the various soft-chemistry routes, sol-gel route has been particularly effective in the preparation of bulk metal oxides, such as ceramics, glass films and fibers.[4] Due to such success, sol-gel route has also been applied to nanoparticle synthesis. In particular, aqueous sol-gel method has yielded various oxidic solid materials in environment friendly and cost-effective manner at low temperatures. In spite of significant advancements, the number of oxidic nanoparticles obtained by the aqueous sol-gel chemistry is still small compared to the number of compounds obtained via ceramic process. It appeared that in many cases a synthesis protocol developed for a bulk metal oxide could not be directly utilized in the nano range.

The reason for this incompatibility can be found in complexity of aqueous sol-gel chemistry. High reactivity of the metal oxide precursors towards water, dual role of water as ligand and solvent, and the large number of reaction parameters that have to be strictly controlled, limit its wide applicability. Such reaction parameters include hydrolysis and condensation rate of the metal oxide precursors, pH, temperature, phase of solution, rate of oxidation, and the nature and concentration of cations or anions.[5] These limitations which are not a hinderance for the preparation of bulk metal oxides, portray a major obstacle for nanoparticle synthesis.

1.1.2.1 Aqueous Sol-gel Route

The aqueous sol-gel process can be simply defined as water involved inorganic polymerization reactions of metal precursors such as metal salts or metal organic compounds such as alkoxides.[6] Generally, the process involves i) preparation of homogeneous solution ethier by dissolving metal salt or organometallic compound in an aqueous solution or an organic solvent that can be mixed with water; ii) Conversion of the homogeneous solution into a form of sol in which dispersion of colloidal paritcles in a liquid takes place; iii)

Transformation of sol into gel in which interconnections among the colloidal particles are established by further condensation.[7] The first step is important with regard to chemical reaction dynamics. The homogeneity of synthetic solution is a prerequisite step for atomic scale modulation of the growth of colloidal particles. The second step is a major part of the entire chemical process involving reactions of hydrolysis and condensation. The reaction rates determine both the size and aggregation number of colloidal particles. The end-product of the process, gel, can be manipulated by suitable processes such as aging, shaping, and sintering, in order to fit the desired purposes.

The sol-gel processes utilize mainly metal salts and metal organic compounds such as metal alkoxides, acetates, and acetylacetonates as precursors (Figure 1.1). The organic constituents as compared to metal salts with ionic ligands are better precursors because of their well-established and predictable reaction pathways. It is well known that ionic ligand introduced with the metal salts plays multiple roles during the formation of metal oxide nanoparticles including the reaction rate, oxidation potential, and morphological evolution. Such complexity gives rise to many unpredictable factors that need to be controlled for the growth of nanoparticles. In aqueous systems, metal alkoxides are

the most widely used precursors, and their chemical transformation into the oxidic network is achieved via hydrolysis and condensation reactions (Figure 1.2).
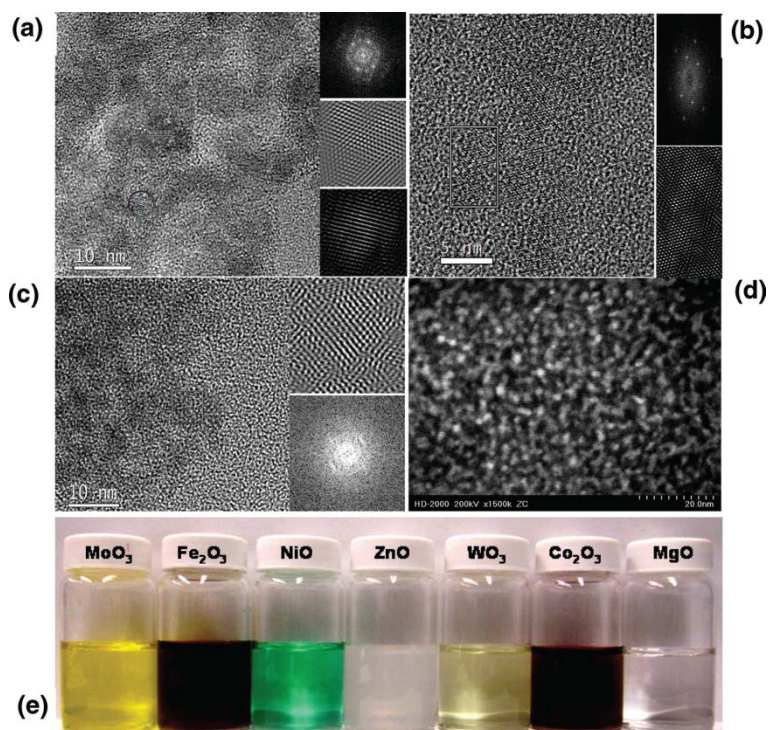
Figure 1.1. Various metal oxide nanocrystals synthesized by aqueous sol-gel route. HRTEM: left columns show the fast Fourier transform (FFT) of a selected squre or rectangular region in the images and its inverse FTT of a) Zn $\rightarrow$ ZnO$_2$ nanocrystals; b) Fe $\rightarrow$ Fe$_2$O$_3$ nanocrystals; c) Mg + 2Zn $\rightarrow$ MgZn$_2$O nanocrystals, and a STEM image of d) Ni $\rightarrow$ NiO nanocrystals. e) Photograph of representative metal oxide nanocrystals aqueous dispersions. (from Ref. [50] Redel, E.; Petrov, S.; Dag, O.; Moir, J.; Huai, C.; Mirtchev, P.; Ozin, G. a *Small* **2012**, *8*, 68.)

—Si—OR + HOH ⇌ (Hydrolysis / Reesterification) —Si—OH + ROH   1

—Si—OH + —Si—OH ⇌ (Water Condensation / Hydrolysis) —Si—O—Si— + HOH   2a

—Si—OH + —Si—OR ⇌ (Alcohol Condensation / Alcoholysis) —Si—O—Si— + ROH   2b
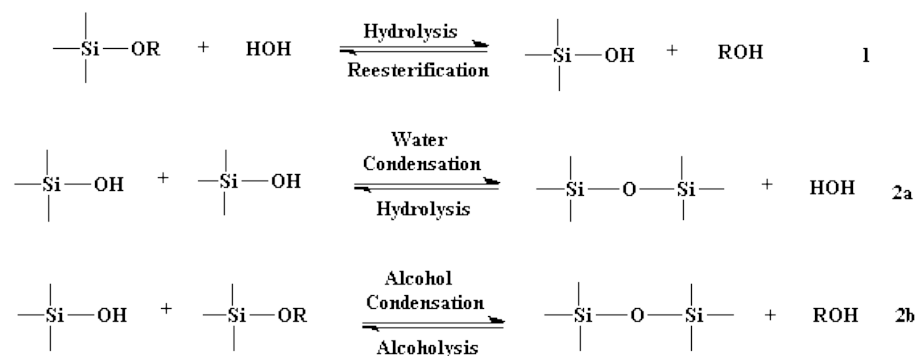
Figure 1.2. The sol-gel process of silicon alkoxide showing hydrolysis (Eq. 1) and condensation, involving oxolation (Eq. 2a) and alkoxolation (Eq. 2b).

1.1.2.2 Nonaqueous Sol-gel Routes

Nonaqueous sol-gel processes involving organic solvents overcome some of the major limitations of aqueous systems. This is because the organic components not only act as oxygen-supplying agents for the metal oxide but also play a critical role in determining particle size, shape, nature of surface, and even composition and crystal structure, in some cases (Figure 1.3).[6]   In aqueous sol-gel processes, oxygen for the formation of the oxidic compound is supplied by water molecules while in nonaqueous systems, oxygen is provided by solvents (ethers, alcohols, ketones, or aldehydes) or by the organic constituent of the precursors (alkoxides or acetylacetonates).[7] The general condensation steps in the formation of a metal-oxygen-metal bond are summarized in Figure 1.4.
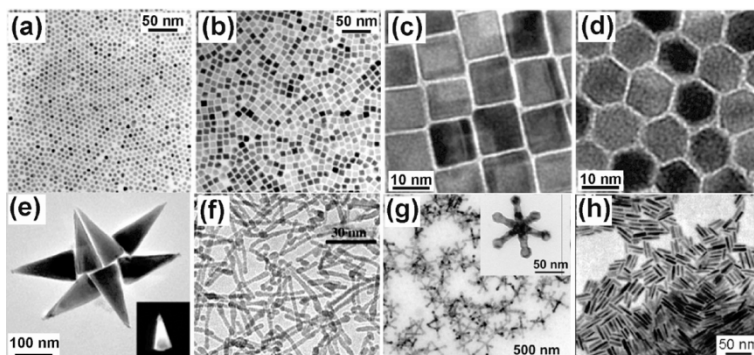
Figure 1.3. Various metal oxide nanocrystals synthesized by nonaqueous sol-gel routes. TEM images of (a) 8-nm-sized spherical $CoFe_2O_4$ nanoparticles used as seeds and (b) cubelike $CoFe_2O_4$ nanocrystals. TEM images of (c) cubelike and (d) polyhedron-shaped $MnFe_2O_4$ nanocrystals.(e) TEM image of conelike ZnO nanocrystals (inset, dark field TEM image of one crystal). (f) TEM image of TiO_2 nanorods. (g) TEM image of MnO multipods (inset, hexapod). (h) TEM image of tungsten oxide nanorods. (from Ref. [3] Niederberger, M. *Acc. Chem. Res.* **2007**, *40*, 793.)

$$\equiv M-X \ + \ R-O-M\equiv \ \longrightarrow \ \equiv M-O-M\equiv \ + \ R-X \qquad (Eq.\ 1)$$

$$\equiv M-OR \ + \ RO-M\equiv \ \longrightarrow \ \equiv M-O-M\equiv \ + \ R-O-R \qquad (Eq.\ 2)$$

$$\equiv M-O-\overset{O}{\overset{\|}{C}}R' \ + \ R-O-M\equiv \ \longrightarrow \ \equiv M-O-M\equiv \ + \ RO-\overset{O}{\overset{\|}{C}}R' \qquad (Eq.\ 3)$$

$$2 \equiv M-OR \ + \ 2\ O{=}\!\!\!< \ \xrightarrow{-2\ ROH} \ \equiv M-O-M\equiv \ + \ O{=}\!\!\!<\!\!\!\!= \qquad (Eq.\ 4)$$
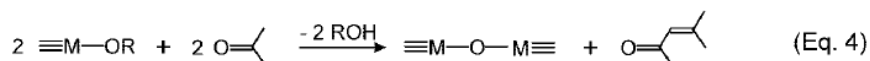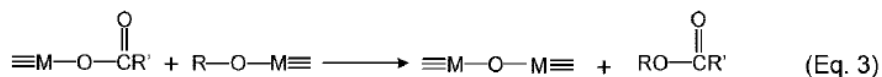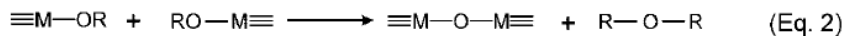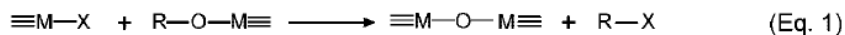
Figure 1.4. Condensation steps leading to M-O-M bonds in nonaqueous sol-gel processes [alkyl halide elimination (eq 1), ether elimination (eq 2), ester elimination (eq 3), and aldol-like condensation (eq 4).] (from Ref. [3] Niederberger, M. *Acc. Chem. Res*. **2007**, *40*, 793.)

1.2 Soft-templates as Nanoreactors for Aqueous Sol-gel Routes

Soft-templates generally include structures formed by surfactants, long-chain polymers, and lipids; which are usually amphiphilic molecules that contain hydrophilic head groups and hydrophobic tails. These materials self-assemble into well-defined aggregates on substrate or in solution in the form of normal and reverse micelles, emulsions, vesicles, or liquid crystals. The aggregates are capable of restricting and directing the growth of nanomaterials (Figuer 1.5). Precursor species react in the confined space or on the outer surface of the soft-templates, producing structures that replicate the original shape of the templates. Therefore, soft-template approaches exhibit intrinsic advantages for preparing metal oxide nanostructures by aqueous sol-gel reaction. For instance, with soft templates, the rate of growth or aggregation of nanoparticles can be restricted which is too fast to be controlled in aqueous phase reaction. Furthermore, the amphiphiles could also act as ligands in the sol-gel reaction influencing chemical and structural features of the final product.
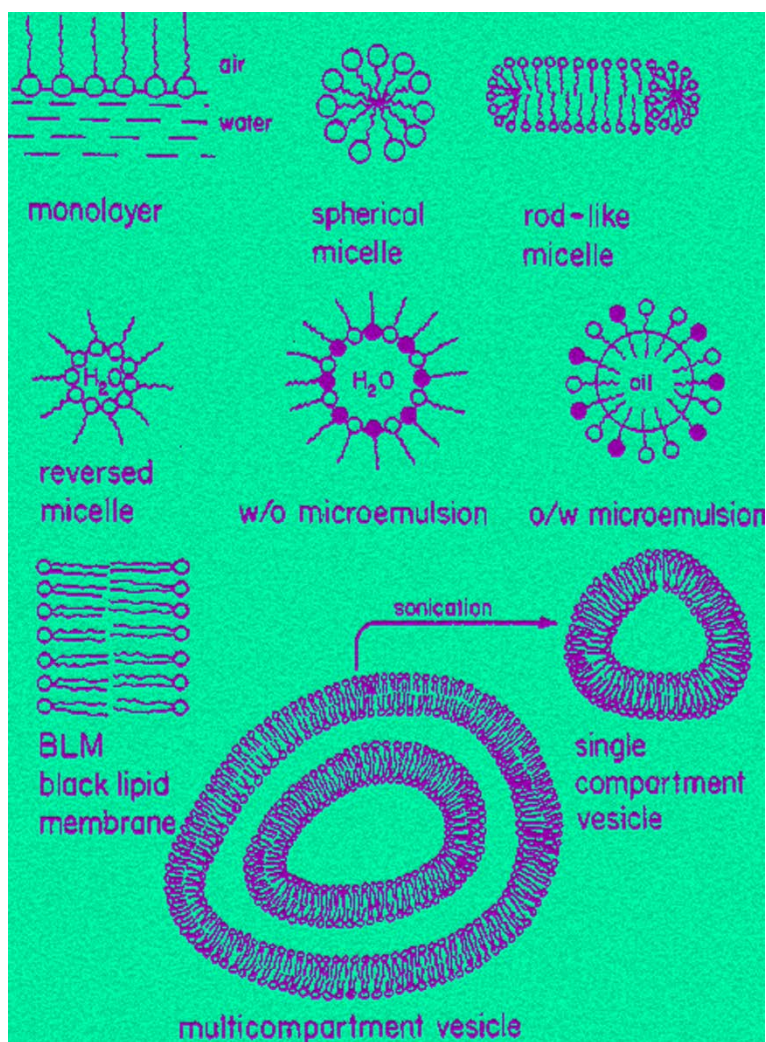
Figure 1.5. An oversimplified representation of organized structures of surfactants in different media. (from Ref. [51] Fendler, J. H. *J. Phys. Chem.* **1980**, *84*, 1485.)

1.2.1 Microemulsions

Certain combinations of water, oil, surfactant, and alcohol- or amine-based cosurfactant yield homogeneous solutions which are termed "microemulsions".[8] The surfactant featured in the first ever microemulsion study by the Schulman group was cetyltrimethylammonium bromide (CTAB), which is still being used (Figure 1.6).[11] The amphiphilic nature of the surfactants such as CTAB enables them to be mixed in both hydrocarbons and water. However, when such surfactant is mixed with a hydrocarbon, the resulting mixture, although optically isotropic, cannot be defined as solution. As shown by Schulman, the orientation of such surfactant molecules seems to have an order. In other words, the surfactant forms spherical aggregates, in which the polar (ionic) ends of the surfactant molecules point toward the center, via ion-dipole interactions with the polar cosurfactant. The cosurfactant here plays a role as an electronegative "spacer" that minimizes coulombic repulsions between the positively charged surfactant heads. The introduction of water molecules to the system causes the aggregates to swell as the water molecules enter the center of the sphere (Figure 1.7). Later, it has been demonstrated that the orientation of the amphiphiles in the microemulsions minimizes

interfacial tension between different phases, making microemulsions thermodynamically stable. This stability is what differentiates microemulsions from traditional macroemulsions, which are, by definition, thermodynamically unstable.[9]
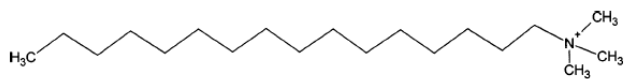
CTAB

Figure 1.6. Structure of cetyltrimethylammonium bromide (CTAB), a common surfactant used in microemulsions.
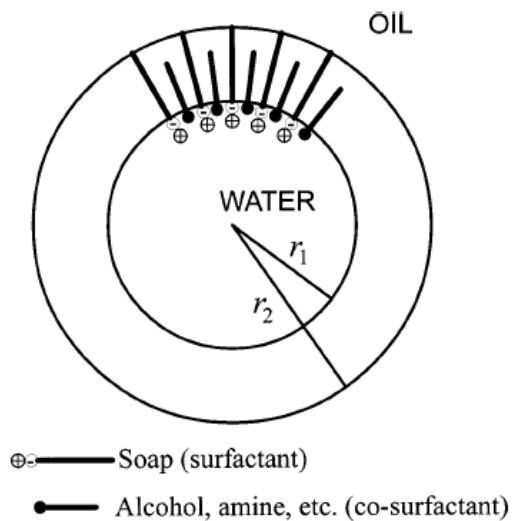
Figuer 1.7. Schulman's model of the reverse micelle, as published in 1943. (from Ref. [8] Hoar, T. P.; Schulman, J. H. *Nature* **1943**, *152*, 102.)

Since Schulman's exploration of CTAB in 1943, other surfactants have emerged, most notably sodium bis(2-ethylhexyl)sulfosuccinate (generally referred to by its trade name, Aerosol OT or AOT) (Figure 1.8).[12] AOT is an ionic amphiphilewith an anion as the head group. The fundamental properties of AOT and AOT-based microemulsions have been studied extensively.[13-16] Other less commonly used surfactants are nonionic surfactants, mostly based on polyethylene ethers such as pentaethylene glycol dodecyl ether (PEGDE), $CH_3(CH_2)_{11}$-O-(CH_2-CH_2-O-)$_5$-H, or Triton-X.
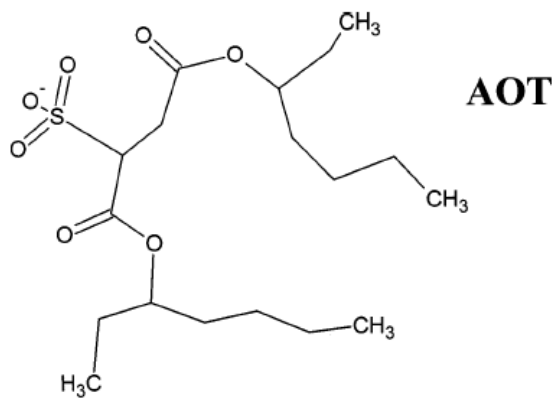
Figure 1.8. Structure of AOT (sodium bis(2-ethylhexyl)-sulfosuccinate).

The spherical aggregates represented in Figure 1.7 are commonly known as reverse micelles and are characterized by ω_0, the molar ratio of water to surfactant, S:

$$\omega_0 = [H_2O]/[S]$$

The size of the water pool at the reverse micelle core can be controlled by adjusting the $[H_2O]/[S]$ ratio, provided $\omega_0 \geq 10$.[10] However, simply changing the size of the reverse micelles does not resolve the issue of micelle formation. As a mixture with four components, oil-water-surfactant-cosurfactant, the phase equilibria of reverse micelle systems are inherently complex. Such phase relationships are normally described using Gibbs triangles; a representative example is given in Figure 1.9, where O_m (oil-continuous micelle phase) represents the region of interest.[13] Note that solutions containing low volume fractions of oil form liquid crystalline (LC) phases and solutions containing more than 50% H_2O versus AOT tend to contain both an O_m and a water phase.
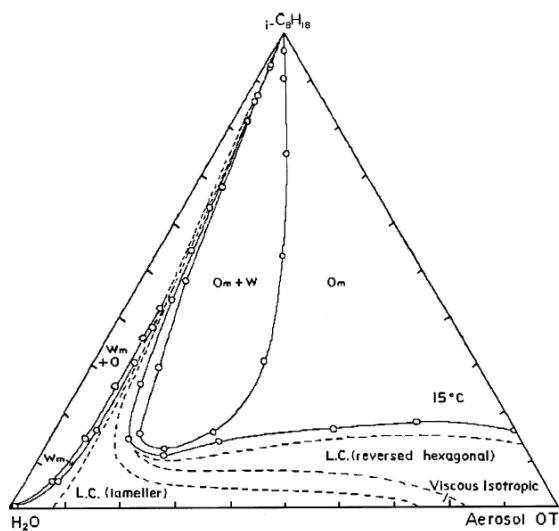
Figure 1.9. Phase diagram for the H$_2$O-AOT-isooctane microemulsion system at 15 °C. Om denotes the reverse micellar region. (from Ref. [13] Kunieda, H.; Shinoda, K. *J. Colloid Interface Sci.* **1979**, *70*, 577.)
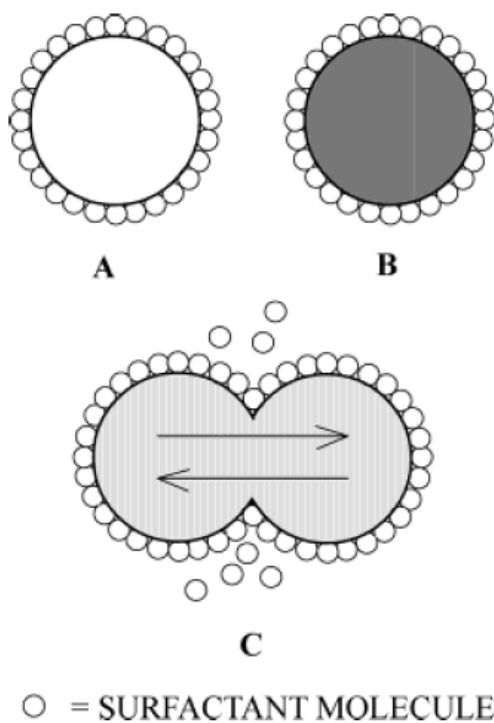
Figure 1.10. Schematic of a collision between two reverse micelles with dissimilar cores. The micelles form a short- lived dimer, as some surfactant molecules are released into the oil phase and the contents of the micellar cores are exchanged. (from Ref. [16] Robinson, B. H.; Toprakcioglu, C.; Dore, J. C.; Chieux, P. J. *J. Chem. Soc., Faraday Trans*. **1984**, *80*, 13.)

Reverse micelles, due to their small size, have continuous Brownian motion, even at room temperature. Collisions between micelles are frequent. Approximately one collision in every thousand produces a short-lived dimer, formed by the expulsion of some surfactant molecules into the bulk oil phase (Figure 1.10).[17] During the ～100 ns lifetime of the dimer, the contents of aqueous cores will exchange before decoalescencing, resulting in the equilibrium distribution of contents.[16] Given the above model of reverse micelle interaction, the suitability of reverse micelles as nanoreactors becomes evident. The Brownian motion of the particles leads to the distribution of reactantstriggering reactionsinside the cores, leading to uniform size and shape of resulting products. However, the complexity of reverse micelle systems present challenges especially after dissociation of ionic salts in the cores.[18] Solvated ions generally affect both the stability of reverse micelles and the phase equilibria.[19] In particular, solvated ions from ionic surfactants reduce radious of the reverse micelle, R_M, due to interaction with the charged surfactant heads, and tend to make the micelles more spherical.[20] Moreover, the influence of solvated ions on R_M increases with increasing concentration and charge.[14] Also, interactions with surfactants also results in changes in

physicochemical properties of the solvated ions.

It is observed that the water molecules in close proximity to the surfactant are greatly influenced by dipole-dipole and ion-dipole interactions with the ionic surfactants and polar cosurfactants, and are largely immobilized.[21] Moreover, it seems that the presence of the surfactant molecules in the reverse micelles, which act as capping agents to some extent, may serve to prevent flocculation of the products but does not alleviate the issue of Ostwald ripening.[22]

The synthesis of metal oxides using reverse micelles requires the coprecipitation of one or more metal ions and is largely similar to the precipitation of oxides from aqueous solutions. Typically, precipitation of hydroxides is triggered by mixing reverse micelle solutions containing dilute NH_4OH with that containing aqueous metal ions. On the other hand, dilute NH_4OH can simply be added directly to a micelle solution of the metal ions. The resulting metal hydroxides are centrifuged and heated to remove water and/or improve crystallinity. This technique has been highly effective in preparing mixed-metal ferrites:[23]

$$M^{2+} + 2Fe^{2+} + OH^- \text{ (excess)} \xrightarrow{\Delta, \ O_2} MFe_2O_4 + xH_2O \uparrow$$
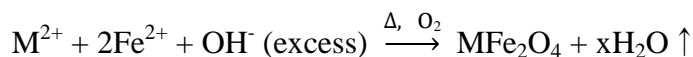
where M = Fe, Mn, or Co. The oxidation of Fe^{2+} to Fe^{3+} has been performed in air in this case, although other researchers prefer to use Fe^{3+} as a starting material.[24,25] If a transition metal cation is either not soluble or not stable in aqueous solution, nanoparticles may be prepared by hydrolysis of a metal organic precursor, which is used in the sol-gel method. TiO_2, for example, has been prepared from tetraisopropyl titanate:[26]

$$Ti(O^iPr_4) + 2H_2O \rightarrow TiO_2 + 4(^iPr-OH)$$
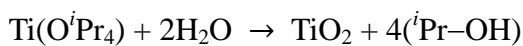
In this case, the reverse micelles containing the precursor were prepared in the absence of water; hydrolysis is induced when a second water-containing reverse micelle solution is added. Recently, a series of mixed-metal ferrites have been produced by precipitating the precursors in a H_2O-AOT-isooctane system and calcining the products at 300-600 °C.[27] Also, combining a micellar solution of Y^{3+},Ba^{2+}, and Cu^{2+} prepared in an Igepal CO-430-cyclohexane system with a second micellar solution containing oxalic acid in the aqueous cores has resulted in 10 nm-sized nanoparticles of $YBa_2Cu_3O_{7-\delta}$

superconductor.[28] The precipitate was then centrifuged and calcined at 800 °C. Recently, similar processes have produced nanoparticles of Al_2O_3,[29] LaMnO,[30] $BaFe_{12}O_{19}$,[31] $Cu_2L_2O_5$ (L = Ho, Er),[32] and $LiNi_{0.8}Co_{0.2}O_2$.[33] Also, as compared to traditional coprecipitation method of preparation, the $BaFe_{12}O_{19}$ prepared in this way is particularly interesting because it exhibits a higher coercivity and saturation magnetization.[34] A representative sampling of various oxides produced by coprecipitation in microemulsions is listed in Table 1.1.

oxide	starting material	surfactant	precipitating agent	reaction conditions	product size (nm)
$LiNi_{0.8}Co_{0.2}O_2$	$LiNO_3$ $Ni(NO_3)_2$ $Co(NO_3)_2$	NP-10	kerosene	calcined 400−800 °C	19−100
Al_2O_3	$AlCl_3$	Triton X-114	NH_4OH	calcined 600−900 °C	50−60
TiO_2	$Ti(O^iPr)_4$	AOT	H_2O		20−200
$Mn_{1-x}Zn_xFe_2O_4$	$Mn(NO_3)_2$ $Zn(NO_3)_2$ $Fe(NO_3)_3$	AOT	NH_4OH	calcined 300−600 °C	5−37
Fe_3O_4	$FeCl_2$ $FeCl_3$	AOT	NH_4OH		~2
Fe_3O_4	$FeSO_4$	AOT	NH_4OH		10
$CoCrFeO_4$	$CoCl_2$ $CrCl_3$ $Fe(NO_3)_3$	SDS	CH_3NH_2	calcined 600 °C	6−16
$CoFe_2O_4$	$CoCl_2$ $FeCl_3$	SDS	CH_3NH_2	dried 100 °C	6−9
$Ni_{1-x}Zn_xFe_2O_4$	$Ni(NO_3)_2$ $Zn(NO_3)_2$ $Fe(NO_3)_3$	AOT	NH_4OH	calcined 300−600 °C	5−30
CuM_2O_5 (M = Ho, Er)	$Cu(NO_3)_2$ $NO(NO_3)_3$ $Er(NO_3)_3$	CTAB	$(NH_4)_2CO_3$	calcined 900 °C	25−30
$Y_3Fe_5O_{12}$	$Y(NO_3)_3$ $Fe(NO_3)_3$	Igepal CA-520	NH_4OH + $(NH_4)_2CO_3$	calcined 600−1000 °C	3
$YBa_2Cu_3O_{7-\delta}$	$Y(OAc)_3$ $BaCO_3$ $Cu(OAc)_2$	Igepal CA-430	oxalic acid		3−12
SnO_2	$SnCl_4$	AOT	NH_4OH	calcined 600 °C	30−70
$BaFe_{12}O_{19}$	$Ba(NO_3)_2$ $Fe(NO_3)_3$	CTAB	$(NH_4)_2CO_3$	calcined 950 °C	5−25
CeO_2	$Ce(NO_3)_3$	CTAB	NH_4OH	calcined 500−700 °C	6−10

Table 1.1. Survey from the literature of oxides prepared from microemulsions. (form Ref. [2] Cushing, B.L.; Kolesnichenko, V.L.; O'Connor, C.J. *Chem. Rev.* **2004**, *104*, 3893.)

1.2.2 Vesicles

Vesicles can be simply defined as hollow lamellar aggregates enclosed with a curved bilayer membrane consisting of ampiphiles,[35] which are dispersible in water or organic solvents.[36] Vesicles exhibit three morphologies depending on the fabrication method: oligovesicular, multilamellar, and unilamellar. The dimensions of vesicles typically range from 10 nm to 50 μm.[37] Due to the unique architecture of the vesicles they find application in biological membrane models, drug delivery systems, and soft-template synthesis of solid materials.

There are three main methods for the synthesis of nanomaterials via soft vesicles: (i) reaction compartmentalization within hydrophilic vesicular chamber (Figure 1.11, I), (ii) membrane-restricted reaction within the bilayers (Figure 1.11, II), and (iii) surface-reactive templating and synthesis at the vesicle outer surface (Figure 1.11, III).
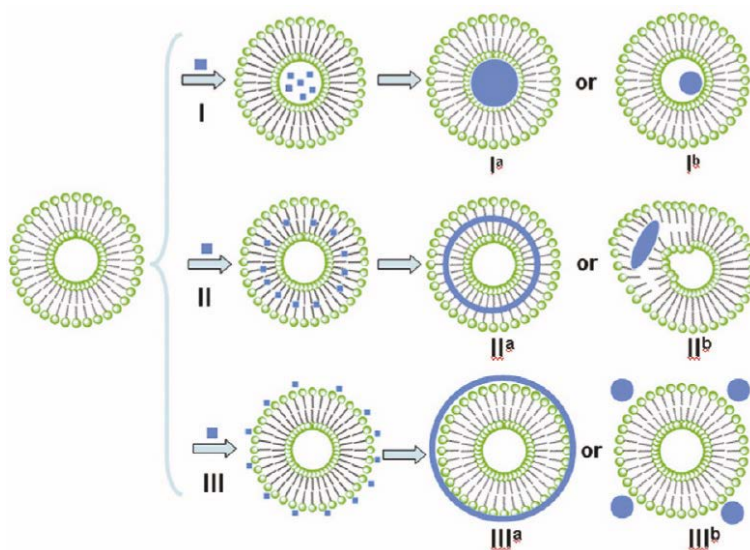
Figure 1.11. Schematic routes of the three principal uses of soft vesicles in the synthesis of nanomaterials: I, reaction compartmentalization; II, membrane-restricted microreactor; III, surface-reactive templating and synthesis. (from Ref. [38] Dong, R.; Liu, W.; Hao, J. *Acc. Chem. Res*. **2012**, *45*, 504.)

1.2.2.1 Synthesis in Vesicle Chamber

The synthesis of nanoparticles in the vesicle chamber was explored by Tricot and Fendler in the mid-1980s.[39] Rh-coated ~ 40 Å diameter CdS nanoparticles were synthesized in situ and stabilized in single-component dihexadecylphosphate vesicles. The vesicles containing nanoparticles were further utilized for transmembrane photoelectron transfer and hydrogen generation. Subsequently, this method has been used successfully for solution synthesis of core-shell metal sulfide nanocrystals.[40] In order to control the synthesis of nanoparticles in the vesicle chamber, three factors need to be considered: (i) the unloaded or unreactive ions external to the vesicles should be removed, leaving only the reactive ions entrapped within the chamber; (ii) the bilayers act as a semipermeable membrane to allow the selective passage of ions; and (iii) the vesicles are stable enough to retain their morphology and contain the reactive ions in their pool. Typically, due to their nearly uniform size, unilamellar vesicles are preferred when synthesizing homogeneous materials. Cryo-TEM has been effectively used tostudy the original morphology of the vesicles and to confirm the location of reaction site.

1.2.2.2 Synthesis within the Vesicle Bilayers

In this method the core of the vesicle bilayer membrane is utilized as a spatially restricted microreactor, producing essentially the same effect on material synthesis as a vesicle chamber (see Figure 1.11, II). However, in aqueous systems, the interior of the bilayers is hydrophobic. In order to accomplish synthesis within vesicle bilayers, it is crucial that the reactive components permeate the hydrophobic core of the bilayer and form expected materials within the bilayer environment.

Synthesis within bilayers offers an effective way to prepare hydrophobic nanoparticles in an aqueous environment. Henceforth, an oil-in-water microemulsion procedure is used to stabilize these nanoparticles in an aqueous phase.[41] The advantage of this method is that the entrapped nanoparticles can be stabilized without using additional surfactants. Nanoparticles with excellent dispersity and uniform sizes have been produced, leading toimproved efficiency in applications such as adsorption, catalysis, and sensors. Gold nanocrystals have been prepared in bilayers after controlling the entrance of the precursor $HAuCl_4$.[42] As a result, a large amount of Au nanoparticles with size of 4.4 $\pm$ 1.6 nm were synthesized within the

copolymer vesicle walls after in situ reduction of $HAuCl_4$ by $NaBH_4$ (Figure 1.12). The incorporation of Au nanoparticles in situ into vesicles produces a potentially versatile hybrid for drug delivery, image tracking, or catalysis.
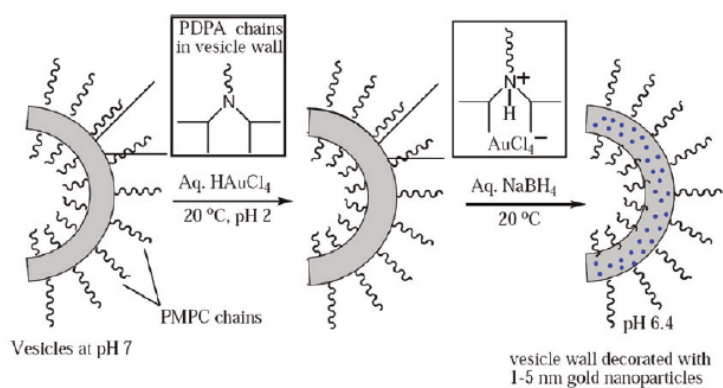
Figure 1.12. Schematic illustration of the formation of PMPC-b-PDPA diblock copolymer vesicles in aqueous phase and subsequent Au NP synthesis within the bilayers. (from Ref. [42] Du, J.; Tang, Y.; Lewis, A. L.; Armes, S. P. *J. Am. Chem. Soc.* **2005**, *127*, 17982.)

1.2.2.3 Vesicles as Reactive Templates

Reactive templates can be defined as vesicles that act not only as templates but also as reactive precursors (Figure 1.13). In previous research, these reactive templates consist of long-chain alkyldimethylamine oxide, e.g. single-chain zwitterionic tetradecyldi methylaminoxide ($C_{14}DMAO$), and multivalent metal anionic surfactant complexes formed via coordination between metal ions and the N–O group.[43,44] These catanionic vesicles are involved in the reaction, but they are preserved and can be produced again after adding acids as a reagent to precipitate the metal ions. A series of metal ligand coordination systems for vesicles has been designed by mixing $C_{14}DMAO$ with different multivalent metal anionic surfactants such as calcium tetradecylamidomethyl sulfate, calcium or barium oleate,[45] and aluminum laurate. Utilizing the Ca^{2+}-ligand vesicles as reactive templates, CaC_2O_4 crystals with different morphologies are produced via the hydrolysis of dimethyl oxalate. During the synthesis, the reaction does not occur in the bulk solution but is limited to the bilayer membranes due to the presence of the metal ions in them. Furthermore since the morphology and size could be precisely controlled, using metal complexes as reactive templates wouldopen up avenues to

prepare a number of inorganic materials.
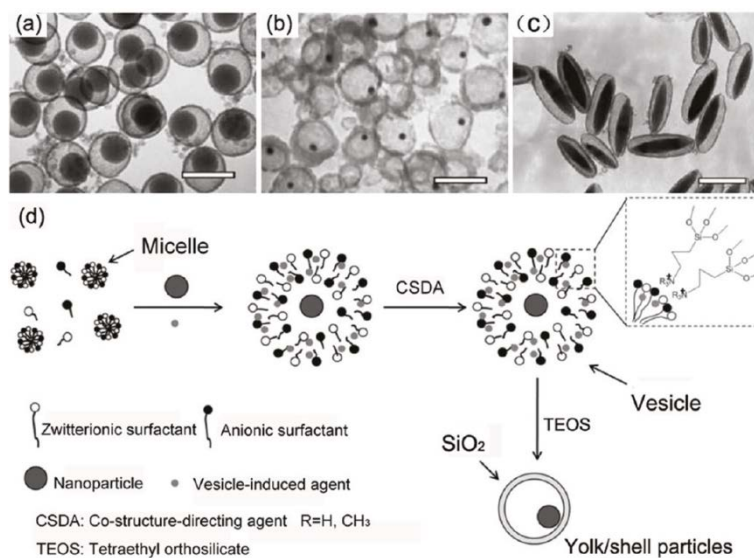
Figure 1.13. TEM images of yolk/SiO$_2$ shell structures encapsulating different kinds of NP cores: (a) 90 nm SiO$_2$ NPs, (b) 10 nm Au NPs, and (c) spindlelike Fe$_2$O$_3$ particles. Scale bars: (a, c) 200 nm; (b) 100 nm. (d) A schematic procedure for producing yolk/SiO$_2$ shell particles using vesicle templates. (from Ref. [38] Dong, R.; Liu, W.; Hao, J. *Acc. Chem. Res*. **2012**, *45*, 504.)

1.2.2.4 Syntheis with Reverse Vesicles

Recently, novel vesicles have been discovered using cationic/anionic (catanionic) surfactant mixtures.[46,47] Similar to micelles and lytropic liquid crystals which have counterparts in nonpolar environments, reverse vesicles were also found to exist in a nonionic surfactant system as a counterpart to vesicles. Amphiphilic molecules in reverse vesicles in a nonpolar organic solvent self-assemble in a direction opposite to vesicles in water i.e. the hydrophilic parts exist inside the bilayer (Figure 1.14). The highly restricted two-dimensional water channels within the bilayers of reverse vesicle can trap guest molecules such as enzymes and inorganic ions, making them ideal for nanoreaction for biological tests and synthesis of inorganic nanomaterials.
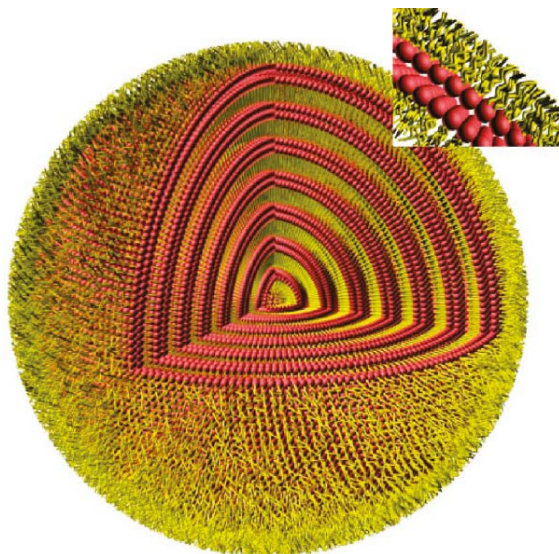
Figuer 1.14. A model of multilamellar giant reverse onions. (from Ref.

[48] Li, H.; Xin, X.; Kalwarczyk, T.; Kalwarczyk, E.; Niton, P.; Hozyst,

R.; Hao, J. *Langmir* **2010**, *26*, 15210.)

Recently, the Hao group have investigated spontaneous construction of stable reverse vesicular phases by mixing a salt-free catanionic surfactant (tetradecyltrimethylammonium laurate, TTAL) and a fatty acid (lauric acid, LA) in nonpolar organic solvents such as cyclohexane.[48,49] In this work they gave the first and detailed confocal fluorescence microscopy observations on these reverse vesicular structures (Figure 1.15).
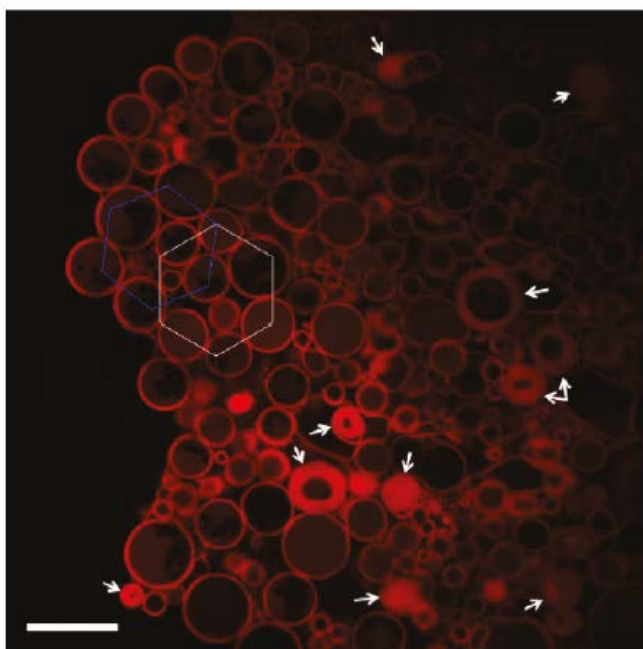
Figure 1.15. Confocal fluorescence micrograph showing a pseudo-two-dimensional network of reverse vesicles. The solid arrows indicate the presence of giant reverse onions. The sample is labeled with rhodamine B, and the scale bar corresponds to 20 μm. (from Ref. [48] Li, H.; Xin, X.; Kalwarczyk, T.; Kalwarczyk, E.; Niton, P.; Hozyst, R.; Hao, J. *Langmir* **2010**, *26*, 15210)

1.3 Dissertation Overview

This thesis encompasses the synthesis of noble multifunctional nanomaterials by applying aqueous sol-gel reaction in soft-templates including microemulsions and reverse vesicles. With unique properties of the soft-templates, we advanced synthetic availabililliy in the formation, surface modification, heterodeposition, and even dissolution of metal oxide nanoparticles (Figure 1.12). Furthermore, intensive evaluations for their usefulness in applications such as biomedical and energy storage fields were examined.

Dissertation is composed of four parts. In the first part (Chapter two) we demonstrate that bioinert tantalum oxide nanoparticles are suitable nanoprobes for high-performance X-ray computed tomography (CT) imaging while simultaneously being cost-effective and meeting the criteria as a biomedical platform. Uniformly sized tantalum oxide nano-particles were prepared using a microemulsion method, and their surfaces were readily modified using various silane derivatives through simple in situ sol-gel reaction. The silane-modified surface enabled facile immobilization of functional moieties such as polyethylene glycol (PEG) and fluorescent dye. PEG was introduced to endow the

nanoparticles with biocompatibility and antifouling activity, whereas immobilized fluorescent dye molecules enabled simultaneous fluorescence imaging as well as X-ray CT imaging. The resulting nanoparticles exhibited remarkable performances in the in vivo X-ray CT angiography and bimodal image-guided lymph node mapping. We also performed an extensive study on in vivo toxicity of tantalum oxide nanoparticles, revealing that the nanoparticles did not affect normal functioning of organs.

Second part (Chapter three) represents multimodal imaging, highly desirable for accurate diagnosis because it can provide complementary information of each imaging modality. Multifunctional Fe_3O_4/TaO_x core/shell nanoparticles were synthesized using a sol-gel reaction of tantalum(V) ethoxide in a microemulsion containing Fe_3O_4 nanoparticles. The resulting nanoparticles were biocompatible and exhibited prolonged circulation time. When the nanoparticles were intravenously injected, the tumor-associated vessel and the microenvironment of the tumor were observed with computed tomography (CT) and magnetic resonance imaging (MRI), respectively.

Third part (Chapter four) is about galvanic replacement reactions providing a simple and versatile route for producing hollow

nanostructures with controllable pore structures and compositions. They have previously been used for the chemical transformation of metallic nanostructures only. We demonstrated that the galvanic replacement reactions can occur in metal oxide nanocrystals as well. When manganese oxide (Mn_3O_4) nanocrystals were reacted with iron(II) perchlorate in reverse vesicle solution, hollow box-shaped nanocrystals of Mn_3O_4/γ-Fe_2O_3 ("nanoboxes") were produced. These nanoboxes ultimately transformed into hollow cage-like nanocrystals of γ-Fe_2O_3 ("nanocages"). These nanoboxes and nanocages showed excellent performance as anode materials for lithium ion batteries owing to their non-equilibrium compositions and unique hollow structures. Our approach of using a galvanic replacement reaction is an effective method for simultaneously manipulating the morphologies and compositions of oxide nanocrystals on a large scale.
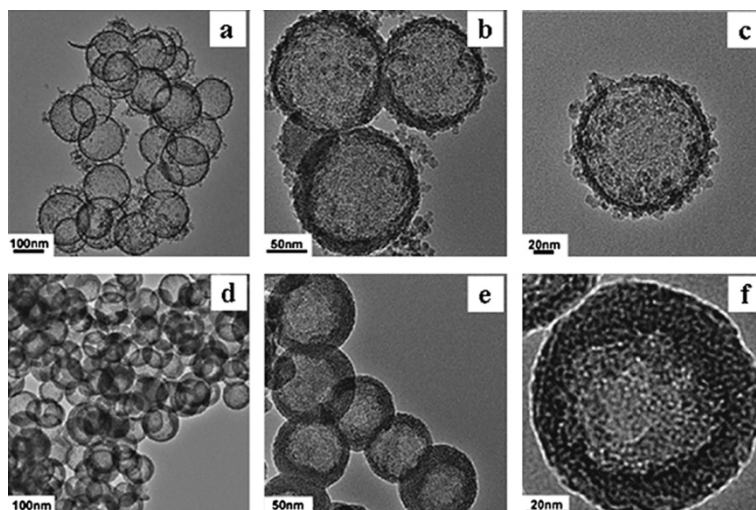
Figure 1.16. Hollow mesoporous SiO_2 synthesized by microemulson method. TEM images of mesoporous SiO_2 nanocapsules prepared with different molar ratios of CSS(carboxylethylsilanetriol sodium salt) : NaOH, (a,b,c) CSS : NaOH = 0.2 : 1.5, (d,e,f) CSS : NaOH = 0.2 : 1.0. (from Ref. [52] Liu, J.; Liu, F.; Gao, K.; Wu, J.; Xue, F. *J. Mater. Chem.*, **2009**, *19*, 6073.)
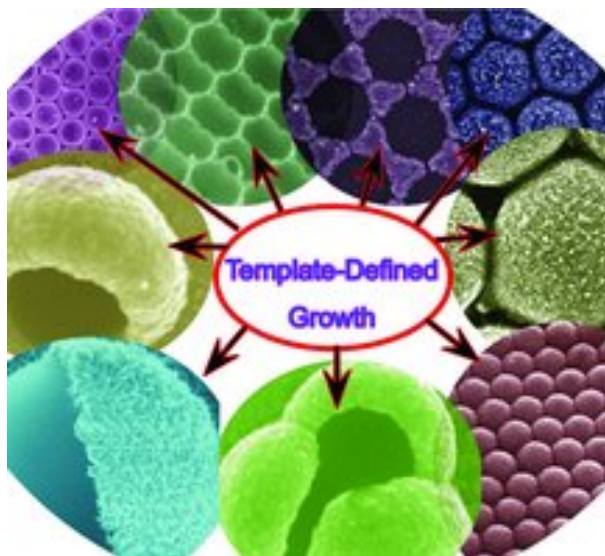
Figure 1.17. Tailoring metal oxide nanostructures via soft-templating sol-gel routes.

1.4 References

[1] RaO, C.N.R. Transition metal oxides. *Annu. Rev. Phys. Chem.* **1989**, *40*, 291.

[2] Cushing, B.L.; Kolesnichenko, V.L.; O'Connor, C.J. *Chem. Rev.* **2004**, *104*, 3893.

[3] Niederberger, M. *Acc. Chem. Res.* **2007**, *40*, 793.

[4] Jun, Y. W.; Choi, J. S.; Cheon, J. *Angew. Chem. Int. Ed.* **2006**, *45*, 3414.

[5] Livage, J.; Henry, M.; Sanchez, C. *Prog. Solid State Chem.* **1988**, *18*, 259.

[6] Bradley, D. C.; Mehrota, R. C.; Rothwell, I. P.; Singh, A. *Academic Press*: London **2001**.

[7] Mehrota, R. C.; Singh, A. *Prog. Inorg. Chem.* **1997**, *46*, 239.

[8] Hoar, T. P.; Schulman, J. H. *Nature* **1943**, *152*, 102.

[9] Gillberg, G.; Lehtinen, H.; Friberg, S. *J. Colloid Interface Sci.* **1970**, *33*, 40.

[10] Prince, L. M. *J. Soc. Cosmet. Chem.* **1970**, *21*, 193.

[11] Li, F.; Li, G.-Z.; Wang, H.-Q.; Xue, A.-J. *Colloids Surf., A* **1997**, *127*, 89.

[12] Chang, G. X.; Shen, F.; Yang, L. F.; Ma, L. R.; Tang, Y.; Yao, K. D.; Sun, P. C. *Mater. Chem. Phys.* **1998**, *56*, 97.

[13] Kunieda, H.; Shinoda, K. *J. Colloid Interface Sci.* **1979**, *70*, 577.

[14] Frank, S. G.; Shaw, Y.-H.; Li, N. C. *J. Phys. Chem.* **1973**, *77*, 238.

[15] Zulauf, M.; Eicke, H.-F. *J. Phys. Chem.* **1979**, *83*, 480.

[16] Robinson, B. H.; Toprakcioglu, C.; Dore, J. C.; Chieux, P. J. *J. Chem. Soc., Faraday Trans.* **1984**, *80*, 13.

[17] Clarke, J. H. R.; Nicholson, J. D.; Regan, K. N. *J. Chem. Soc., Faraday Trans. 1* **1985**, *81*, 1173.

[18] Grand, D. *J. Phys. Chem. B* **1998**, *102*, 4322.

[19] Howe, A. M.; Toprakcioglu, C.; Dore, J. C.; Robinson, B. H. *J. Chem. Soc., Faraday Trans.* 1 **1986**, *82*, 2411.

[20] Bedwell, B.; Gulari, E. *J. Colloid Interface Sci.* **1984**, *102*, 88.

[21] Goffredi, M.; Liveri, V. T.; Vassallo, G. *J. Solution Chem.* **1993**, *22*, 941.

[22] Soma, J.; Papadopoulos, K. D. *J. Colloid Interface Sci.* **1996**, *181*, 225.

[23] O'Connor, C. J.; Seip, C. T.; Carpenter, E. E.; Li, S.; John, V. T. *Nanostruct. Mater.* **1999**, *12*, 65.

[24] Yener, D. O.; Giesche, H. *J. Am. Ceram. Soc.* **2001**, *84*, 1987.

[25] Zhang, Z. J.; Wang, Z. L.; Chakoumakos, B. C.; Yin, J. S. *J. Am. Chem. Soc.* **1998**, *120*, 1800.

[26] Moran, P. D.; Bartlett, J. R.; Bowmaker, G. A.; Woolfrey, J. L.; Cooney, R. P. *J. Sol-Gel Sci. Technol.* **1999**, *15*, 251.

[27] Yener, D. O.; Giesche, H. *Ceram. Trans.* **1999**, *94*, 407.

[28] Kumar, P.; Pillai, V.; Bates, S. R.; Shah, D. O. *Mater. Lett*. **1993**, *16*, 68.

[29] Pang, Y.-X.; Bao, X. *J. Mater. Chem*. **2002**, *12*, 3699.

[30] Hayashi, M.; Uemura, H.; Shimanoe, K.; Miura, N.; Yamazoe, N. *Electrochem. Solid State Lett*. **1998**, *1*, 268.

[31] Pillai, V.; Kumar, P.; Multani, M. S.; Shah, D. O. *Colloids Surf., A* **1993**, *80*, 69.

[32] Porta, F.; Bifulco, C.; Fermo, P.; Bianchi, C. L.; Fadoni, M.; Prati, L. *Colloids Surf., A* **1999**, *160*, 281.

[33] Lu, C.-H.; Wang, H.-C. *J. Mater. Chem*. **2003**, *13*, 428.

[34] Palla, B. J.; Shah, D. O.; Garcia-Casillas, P.; Matutes-Aquino, J. *J. Nanopart. Res*. **1999**, *1*, 215.

[35] Dong, R.; Hao, J. *Chem. Rev*. **2010**, *110*, 4978.

[36] Li, H.; Xin, X.; Kalwarczyk, T.; Kalwarczyk, E.; Niton, P.; Holyst, R.; Hao, J. *Langmuir* **2010**, *26*, 15210.

[37] Song, A.; Jia, X.; Teng, M.; Hao, J. *Chem.;Eur. J*. **2007**, *13*, 496.

[38] Dong, R.; Liu, W.; Hao, J. *Acc. Chem. Res*. **2012**, *45*, 504

[39] Tricot, Y. M.; Fendler, J. H. *J. Am. Chem. Soc*. **1984**, *106*, 7359.

[40] Korgel, B. A.;Monbouquette, H. G. *Langmuir* **2000**, *16*, 3588.

[41] Fan, H. *Chem. Commun*. **2008**, 1383.

[42] Du, J.; Tang, Y.; Lewis, A. L.; Armes, S. P. *J. Am. Chem. Soc*. **2005**, *127*,

17982.

[43] Wang, J.; Song, A.; Jia, X.; Hao, J.; Liu, W.; Hoffmann, H. *J. Phys. Chem. B* **2005**, *109*, 11126.

[44] Teng, M.; Song, A.; Liu, L.; Hao, J. *J. Phys. Chem. B* **2008**, *112*, 1671.

[45] Song, A.; Hao, J. *Curr. Opin. Colloid Interface Sci.* **2009**, *14*, 94.

[46] Kaler, E. W.; Herrington, K. L.; Murthy, A. K.; Zasadzinski, J. A. N. *Science* **1989**, *245*, 1371.

[47] Horbaschek, K.; Hoffmann, H.; Hao, J. *J. Phys. Chem. B* **2000**, *104*, 2781.

[48] Li, H.; Xin, X.; Kalwarczyk, T.; Kalwarczyk, E.; Niton, P.; Hozyst, R.; Hao, J. *Langmir* **2010**, *26*, 15210.

[49] Li, H.; Hao, J.; Wu, Z. J. *Phys. Chem. B* **2008**, *112*, 3705.

[50] Redel, E.; Petrov, S.; Dag, O.; Moir, J.; Huai, C.; Mirtchev, P.; Ozin, G. a *Small* **2012**, *8*, 68.

[51] Fendler, J. H. *J. Phys. Chem.* **1980**, *84*, 1485.

[52] Liu, J.; Liu, F.; Gao, K.; Wu, J.; Xue, F. *J. Mater. Chem.*, **2009**, *19*, 6073.

Chapter 2. Large-Scale Synthesis of Bioinert Tantalum Oxide Nanoparticles for X-ray Computed Tomography Imaging and Bimodal Image-Guided Sentinel Lymph Node Mapping

2.1 Introduction

Colloidal nanoparticles have been intensively investigated for their biomedical applications related to imaging, diagnostics, and therapeutics due to their unique electronic, optical, and magnetic properties.[1] Injected nanoparticles can evade phagocytosis of reticuloendothelial system (RES) and accumulate in targeted organs. Circulation time and interactions with various cells such as macrophages are highly dependent on the size and surface properties of nanoparticles. Consequently, there have been extensive efforts to develop effective nanobiomedical platforms based on inorganic nanoparticles.[2] For example, semiconductor nanoparticles, also known as quantum dots (QDs), have been extensively studied as fluorescent probes for optical imaging.[3] On the other hand, magnetic nanoparticles

have been used as contrast agents in magnetic resonance imaging (MRI).[4]

X-ray computed tomography (CT) is one of the most popular diagnostic imaging techniques in clinical use, owing to its merits such as cost effectiveness, high-contrast resolution, unlimited penetration depth, and facile image processing.[5] However, for accurate diagnosis, administration of a large amount of contrast agent is often required because sensitivity and soft tissue contrast are inherently low in X-ray CT imaging. Therefore, cost should be seriously considered in the design of new X-ray CT contrast agents.[6a-b] Currently, iodinated compounds are widely used as CT contrast agents with an emphasis on its cost-effectiveness and safety than its performance. However, small iodinated compounds are rapidly excreted via renal elimination, resulting in short circulation time that limits their applications for target-specific imaging and angiography.[6]

Recently, various nanoparticles have been introduced as potential candidates for X-ray contrast agents.[7] Compared to conventional iodine-based contrast agents, nanoparticle-based agents are characterized by superior contrast enhancement and prolonged blood circulation time. Furthermore, nanoparticles can be easily

functionalized with various biomolecules for tissue-specific uptake and multimodal imaging applications, resulting in more dependable diagnostic information.[8] However, dissolution or aggregation of the nanoparticles in blood vessels can cause severe toxicity or fatal embolism, respectively, and it can become even more serious when large dose is used during X-ray CT imaging. Therefore, colloidal stability of the nanoparticles has been the most important issue for their clinical applications. This requirement is also closely related to the surface chemistry of the nanoparticles. Consequently, the development of inexpensive and non-toxic nanoparticles with facile and reliable surface modification capability is highly desirable.

Until now, the most studied nanomaterials for X-ray contrast agents are nanoparticles of Au and Bi_2S_3.[7] Bi_2S_3 nanoparticles have apparent limitations due to the intrinsic toxicity of Bi. Although it is relatively easy to synthesize and functionalize Au nanoparticles, the cost of using gold as X-ray contrast agent is a huge obstacle to their clinical utilization. Tantalum is another strong candidate as a CT contrast agent due to its high X-ray attenuation coefficient and bioinertness.[9] Due to their relative non-toxicity, tantalum and tantalum oxide have been widely used in clinical applications as a part of radiographic markers,

implants, artificial joints, stents, and vascular clips.[9] Moreover, tantalum is much cheaper than gold while possessing a comparable X-ray attenuation coefficient (Ta: 4.3 and Au: 5.16 cm^2/kg at 100 eV). Very recently, water-soluble sub-10 nm tantalum oxide nanoparticles were synthesized for X-ray/CT imaging applications.[10] Although X-ray contrast was enhanced by the tantalum oxide nanoparticles, rapid renal filtration occurred. While rapid clearance of nanoparticles is desirable in some cases, the limited image acquisition time should be problematic for applications other than angiography. Herein, we report facile and large-scale synthesis of uniform-sized tantalum oxide (TaO_x) nanoparticles via microemulsion method under ambient conditions. The surface of the TaO_x nanoparticles was easily modified by silane derivatives. Surface modification with fluorophore or polymer allowed the nanoparticles to be successfully used as an in vivo X-ray CT contrast agent for angiography and bimodal image-guided lymph node mapping.[11] For the first time, in vivo toxicity of tantalum oxide nanoparticles was systematically examined. It was found that the nanoparticles did not cause any significant adverse effect on liver and other organs.

2.2 Experimental Section

2.2.1 Synthesis of TaO$_x$ nanoparticles in microemulsion.

Microemulsion (ME) was prepared by adding 0.25 mL of NaOH aqueous solution (75 mM) to oil phase composed of 2.3 g of Igepal CO-520 (Aldrich), ethanol (Samchun, 99.5%), and 20 ml of cyclohexane (Samchun, 99.5%). After 0.05 ml of tantalum(V) ethoxide (0.3 mmol, Strem, 99.8%) was added to the ME at room temperature, a resulting mixture containing tantalum oxide nanoparticles (designated as TaO$_x$-ME) was synthesized within 5 min. To control the size of the TaO$_x$ nanoparticles, the amount of ethanol was varied (0, 0.25, 0.5, and 0.75 mL).

2.2.2. One-pot surface modification of TaO$_x$ nanoparticles: Pegylation and rhodamine B isocyanate (RITC) functionalization of TaO$_x$ nanoparticles for bimodal imaging applications.

To prepare rhodamine B isocyanate (RITC)-functionalized silane, 110 μL of aminopropyltriethoxysilane (APTES, Aldrich) was reacted with 50 mg of RITC in 3.75 mL of ethanol at room temperature for 24 h. The resulting solution along with 12.5 mL of 2-

methoxy(polyethylenoxy)propyltrimethoxysilane (PEG-silane, Gelest, 596 ~ 725 Da) was added to 1 L of the as-prepared TaO_x-ME. The mixture was then stirred at room temperature for 24 h, becoming a red turbid solution. The resulting solution was evaporated at 60 ^{o}C until the solution became transparent, after which the functionalized TaO_x nanoparticles were precipitated by adding a mixed solution of 1:1 (v/v) ether/n-hexane. The precipitates were purified with ether and dispersed in ethanol. To this solution, 100 mg of methoxypoly(ethylene glycol) succinimidylglutarate (mPEG-SG, MW 2000, Sunbio) was added. The mixture was stirred overnight at 30 ^{o}C to conjugate PEG onto residual amine groups on the surface of the functionalized TaO_x nanoparticles. After washing several times with deionized water, the final product, designated as PEG-RITC-TaO_x, was dispersed in phosphate buffered saline (PBS) buffer.

2.2.3 X-ray CT and fluorescence imaging with PEG-RITC-TaO_x. Phantom Test.

Various concentrations of PEG-RITC-TaO_x (0.22, 0.45, 0.9, 1.8, 3.6, 7.2, 14.5, and 29 mg of Ta/mL) dispersed in deionized water were prepared in 1.5 mL microtubes. CT images were acquired using a dual-

source CT system (Somatom Definition, Simens). Imaging parameters were as follows: thickness, 1 mm; pitch, 1; 120 kVp, 90 mA; field of view, 84×84; gantry rotation time, 0.5 s; table speed, 6 mm/s.

Cell Culture. RAW264.7 (murine macrophage cell line) was grown in monolayers in Dulbecco's Modified Eagle's Medium (DMEM, WelGENE) supplemented with 10% (v/v) fetal bovine serum (FBS, Gibco) and penicillin/streptomycin (100 U/mL and 100 μg/mL, respectively, Gibco) in a humidified 5% CO_2 atmosphere at 37 °C.

Cellular Uptake. To observe cellular uptake of the TaO_x nanoparticles, 1×10^4 RAW 264.7 cells per well were cultured in an 8-well chamber slide (NalgenNunc, Naperville, IL) and incubated with PEG-RITC-TaO_x at various concentrations (0, 0.6, 1.2, and 2.4 mg of Ta/mL). After 24 hr, the cells were washed with PBS, fixed with 4% paraformaldehyde, and stained with 4′,6-diamidino-2-phenylindole (DAPI, 1 μg/mL in PBS, Roche). Fluorescence images were acquired by confocal laser scanning microscopy (CLSM) (LSM 510, Carl Zeiss, Germany).

Cell Viability Assay. The viability and proliferation of cells in the presence of TaO_x nanoparticles were evaluated by 3-[4,5-dimethylthialzol-2-yl]-2,5-diphenyltetrazolium bromide (MTT, Sigma)

assay. The assay was performed in triplicate in the following manner. RAW264.7 cells were seeded into 96-well plates at a density of 1×10^4 cells per well in 200 μL of media and grown overnight. The cells were then incubated with various concentrations of PEG-RITC-TaO$_x$ (0, 0.075, 0.15, 0.3, 0.6, 1.2, and 2.4 mg of Ta/mL) for 24 h. Following incubation, cells were incubated in media containing 0.1 mg/mL of MTT for 1 h. Thereafter, MTT solution was removed, and precipitated violet crystals were dissolved in 200 μL of DMSO. The absorbance was measured at 560 nm using a VersaMax™ microplate reader (Molecular Devices).

In Vitro CT Imaging. RAW264.7 cells were seeded onto culture dishes at a density of 1×10^6 cells per plate in 10 mL of media and grown overnight. Subsequently, various concentrations of PEG-RITC-TaO$_x$ (0, 0.63, 1.3, and 2.5 mg of Ta/mL) dispersion were added. After 24 h, the cells were washed twice with PBS to remove free nanoparticles and detached by the addition of 1 ml of trypsin/EDTA (Gibco). After centrifugation at 1500 rpm for 5 min, cells were dispersed in 1 mL of culture media and transferred to a 1.5 mL microtube. Cell pellets were prepared by centrifugation at 2000 rpm for 5 min. CT images were acquired using a dual-source CT system

(Somatom Definition, Simens). Imaging parameters were as follows: thickness, 1 mm; pitch, 1; 120 kVp, 90 mA; field of view, 84 × 84; gantry rotation time, 0.5 s; table speed, 6 mm/s.

In Vivo CT Imaging. CT images were acquired prior to injection of PEG-RITC-TaO$_x$ as well as at appropriate time points after administration. Rats were anesthetized by intraperitoneal injection of a mixture of Zoletil (1.92 mg/kg; Virbac, France), Rompun (0.48 mg/kg; Bayer Korea, Korea), and saline. Then, 1 mL of PEG-RITC-TaO$_x$ dispersion (840 mg/kg) was injected through the tail vein of the rat. For lymph node imaging, 100 μL of the PEG-RITC-TaO$_x$ solution was injected intradermally into the paws of rats, which were repeatedly imaged up to 2 h after injection. CT images were acquired using a Brilliance 64-slice CT Scanner (Philips Medical System). Imaging parameters were as follows: thickness, 0.1 mm; pitch, 0.648; 120 kVp, 192 mA; field of view, 108 × 108; matrix, 1024 × 1024 pixels; gantry rotation time, 0.75 s; table speed, 16.7 mm/s. Thin-section axial images were reformed to coronal images through a computational technique referred to as multiplanar-reconstruction (MPR). The three-dimensional (3-D) reconstructed images were obtained using OsiriX (Version 3.8.1; 32 bit; OsiriX foundation, Geneva).

In Vitro and In Vivo Fluorescence Imaging. In vitro and in vivo fluorescence images were acquired using a fluorescence imaging system at an excitation wavelength of 550 nm (Kodak IS4000MM pro, US).

2.3 Result and Discussion

2.3.1 Synthesis of TaO$_x$ nanoparticles

The overall synthetic process of the TaO$_x$ nanoparticles was adopted from the microemulsion synthesis of silica nanoparticles with some modifications (Figure 2.1).[12] We used 75 mM NaOH solution as a base catalyst for the sol-gel reaction of tantalum(V) ethoxide instead of typical ammonia catalyst used in silica sol-gel reactions since the reaction rate of tantalum(V) ethoxide is much faster than that of TEOS and ammonia catalyst would lead to uncontrolled agglomeration of nanoparticles. After emulsification of a mixture composed of cyclohexane, ethanol, NaOH, and Igepal CO-520 surfactant, tantalum(V) ethoxide was added to the emulsion. Controlled sol-gel reaction in the reverse micelles at room temperature led to the formation of uniform nanoparticles within 5 min. Transmission electron microscopy (TEM) image of the as-prepared TaO$_x$ nanoparticles in micelles (TaO$_x$-ME) showed that the size distribution of the nanoparticles was very narrow ($\sigma_r \leq 5\%$) (Figure 1a). X-ray diffraction (XRD), electron diffraction (ED), and X-ray photoelectron spectroscopy (XPS) data (Figure 2.3) revealed that the nanoparticles

were amorphous and composed of tantalum suboxides (TaO_x, $x \sim 1$).

The size of the nanoparticles could be controlled in the range of 5-15

nm by varying the amount of ethanol (Figure 2.4).[13] The increased

amount of ethanol seems to have resulted in decrease of hydrolysis rate

of tantalum ethoxide, which eventually led to production of large

nanoparticles.[14]
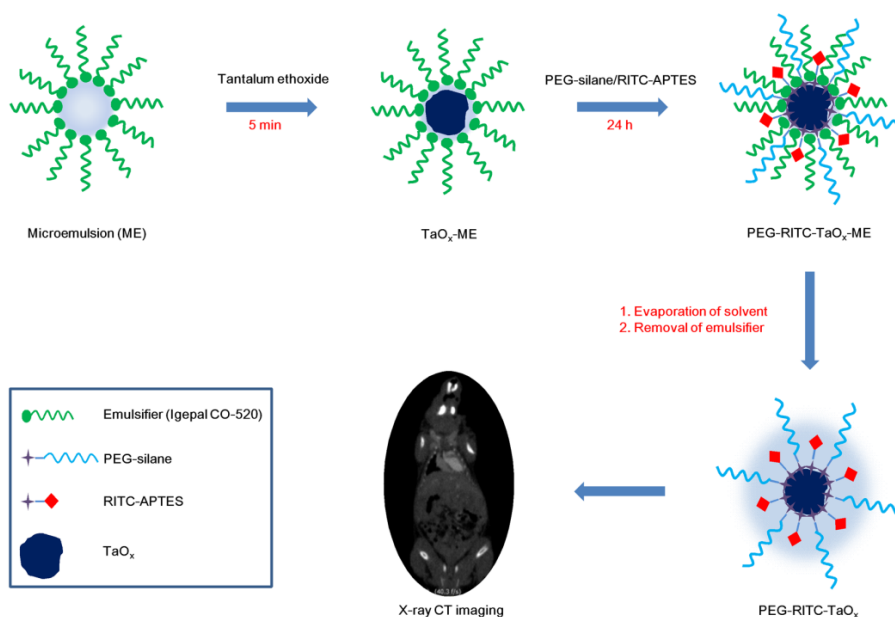
Figure 2.1. Schematic illustration of synthesis, surface modification of TaO$_x$ nanoparticles, and their applications to X-ray CT imaging.
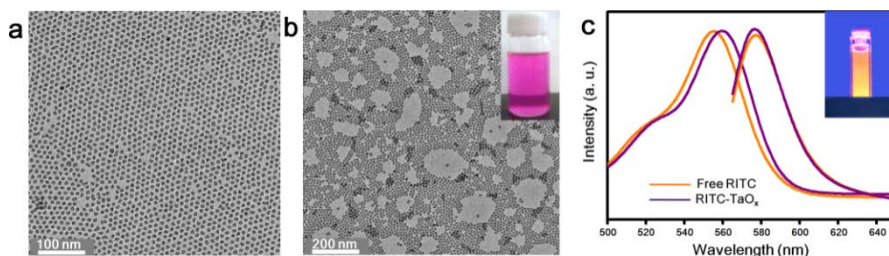
Figure 2.2. (a) TEM image of as-prepared TaO_x nanoparticles in microemulsions, and (b) TEM image of PEG-RITC-TaO_x dispersed in water (inset: photograph of the aqueous dispersion of nanoparticles). (c) Absorbance and fluorescence spectra of PEG-RITC-TaO_x and free RITC in PBS solution. Optical densities were equalized to match the number of RITC molecules in both samples ($\lambda_{ex} = 520$ nm, inset: photographic image of the fluorescent nanoparticles in PBS solution excited with UV light).
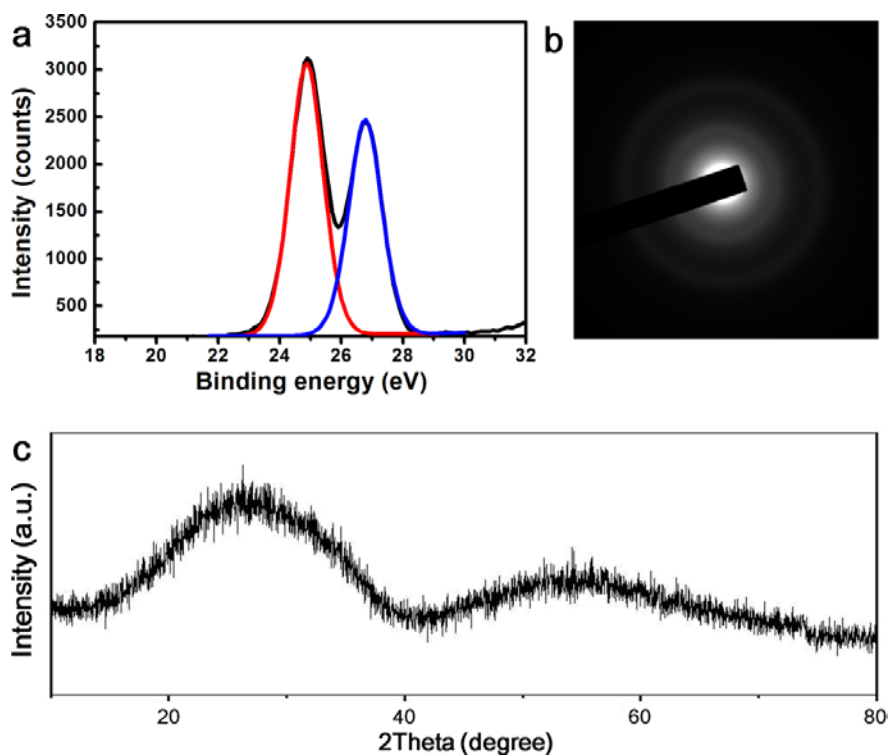
Figure 2.3. Characterization of 9 nm-sized TaO$_x$ nanoparticles. (a) XPS spectra showing characteristics of Ta 4f$_{7/2}$ (red) and Ta 4f$_{5/2}$ (blue) peaks, (b) ED pattern that reveals no apparent crystallinity, and (c) XRD pattern.
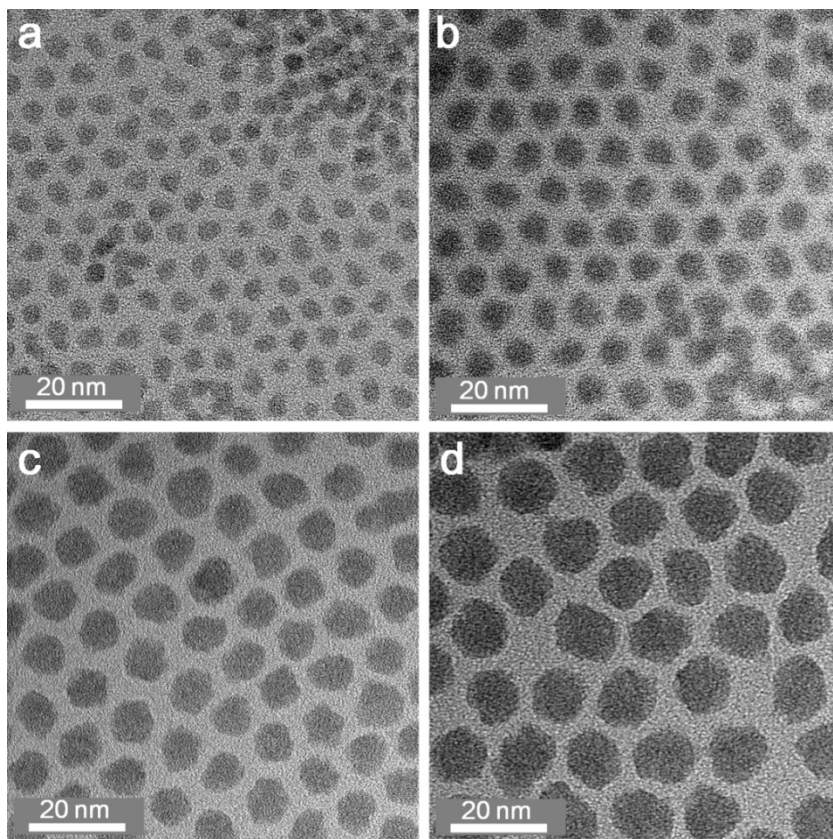
Figure 2.4. Size controlled synthesis of TaO$_x$ nanoparticles. (a-d) TEM images of 6, 9, 13, 15 nm-sized TaO$_x$ nanoparticles in microemulsions.

2.3.2 Surface modification of TaO$_x$ nanoparticles

Surface modification of the TaO$_x$ nanoparticles was directly performed using various silane agents without purification after the synthesis of the TaO$_x$-ME. Since the surface of unmodified TaO$_x$ nanoparticles is acidic and reactive toward condensation reactions, TaO$_x$ nanoparticles would be irreversibly aggregated without additional stabilization. Among the various silane moieties, PEG-silane and dye-conjugated silane were chosen since they are representative biocompatible polymer and fluorescent probe, respectively. Simple silica sol-gel reaction between the hydroxyl groups of the TaO$_x$-ME and silane reagents led to the formation of functionalized-silica-coated TaO$_x$ nanoparticles, which can be applied to multifunctional imaging platforms with multiple modality and/or targeting/therapeutic functions.[15]

Long-circulating nanoparticles are required for effective X-ray CT imaging, such as angiography and tissue specific imaging. To avoid rapid clearance from the blood stream by reticuloendothelial system (RES) uptake, PEG-silane was immobilized on the TaO$_x$ nanoparticles as an anti-fouling agent. For fluorescence imaging, rhodamine B isocyanate (RITC)-conjugated aminopropyltriethoxysilane (APTES)

was attached to the TaO$_x$ nanoparticles. RITC-conjugated-APTES and PEG-silane were simultaneously immobilized on the TaO$_x$-ME to produce tantalum oxide nanoparticles conjugated both with PEG and RITC, designated as PEG-RITC-TaO$_x$. TEM image of PEG-RITC-TaO$_x$ (Figure 2.2b) showed that the nanoparticles were well dispersed in water, whereas no agglomerated nanoparticles were observed. ^{29}Si NMR spectroscopy revealed a single band corresponding to T^2 bonding sites centered at $\delta \sim$ -55 ppm, demonstrating that PEG-silane formed on the surface of the nanoparticles[15] while no separate silica particle formed (Figure 2.5a).[16] As shown in the inset of Fig. 1c, PEG-RITC-TaO$_x$ was transparent, which is advantageous for fluorescence imaging. RITC-conjugated TaO$_x$ exhibited comparable photoluminescence to free RITC (Figure 2.2c), indicating that the conjugated dyes were stable and that their fluorescence was preserved even after the conjugation reaction. The hydrodynamic diameter (HD) of the particles as measured by dynamic light scattering (DLS) was approximately 19 nm, demonstrating that no aggregation occurred (Figure 2.5b), which matched very well with the TEM data.
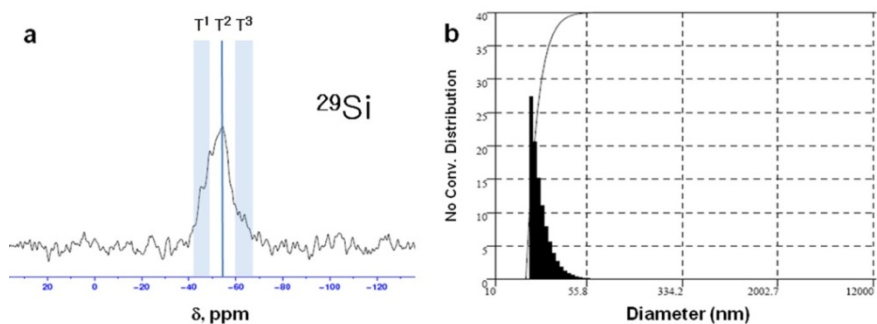
Figure 2.5. (a) ^{29}Si CP MAS NMR spectra of PEG-silane immobilized TaO$_x$ nanoparticles showing characteristics of T^2 bonding peak. (b) Size distribution of PEG-RITC-TaO$_x$ in PBS solution. Dynamic light scattering (DLS) measurement showed that average hydrodynamic diameter of the nanoparticles was 19 nm.
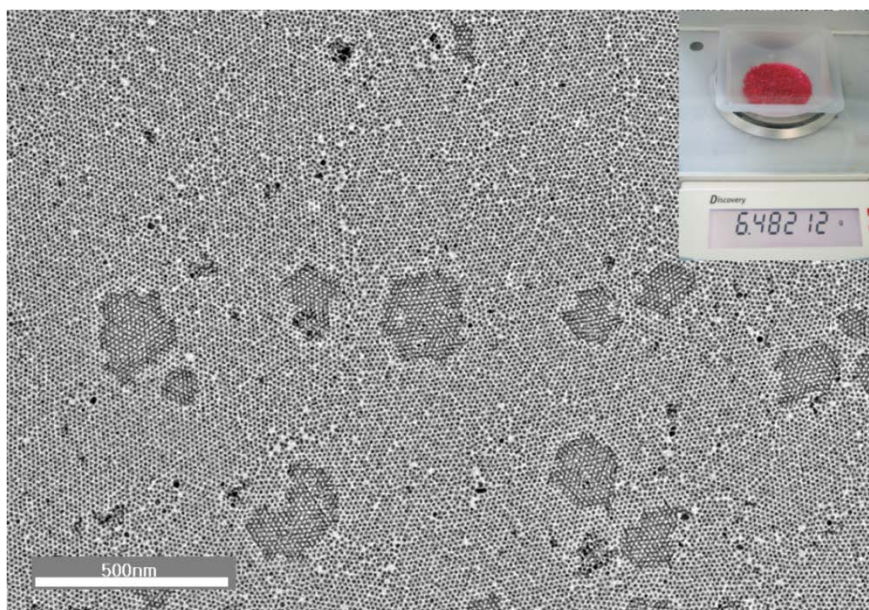
Figure 2.6. Low-magnification TEM image of 9 nm-sized PEG-RITC-TaO$_x$ nanoparticles synthesized in large-scale (inset: a photograph showing 6.48 g of the nanoparticles).

2.3.3 In vitro X-ray CT and optical imaging

X-ray CT phantom images were acquired using various concentrations of PEG-RITC-TaO$_x$ dispersed in deionized water. The CT numbers, called Hounsfield units (HU), increased linearly as the concentration of the nanoparticles increased (Figure 2.7a). Although the contrast enhancement of Ta atom is slightly smaller than that of Au atom in diagnostic X-ray spectra (4.302 and 5.158 cm^2/g, respectively, at 100 keV), the measured HU values of the TaO$_x$ nanoparticles were much higher than those of current iodine-based X-ray contrast agents.[6a,7a,10] MTT assay revealed that cell viability was not hindered by PEG-RITC-TaO$_x$ up to a concentration of 2.4 mg of Ta/mL (Figure 2.7b), which is an extremely high concentration. Cellular X-ray CT and fluorescence imaging were conducted to demonstrate dose-dependent uptake and in vitro multimodal imaging capability of PEG-RITC-TaO$_x$. Cellular uptake was investigated by incubating murine macrophage cells (RAW264.7) with different concentrations of nanoparticles in serum-containing media. The confocal laser scanning microscopy (CLSM) images in Figure 2.7c revealed that the nanoparticles were taken up by RAW264.7 cells via endocytosis. Fluorescence images of the cells after uptake of the nanoparticles show that the red

luminescence became more intense and that HU values increased as the concentration increased (Figure 2.7d). These fluorescence and X-ray CT results demonstrated in vitro bimodal imaging capability as well as dose-dependent uptake of the TaO_x nanoparticles by mammalian cells.
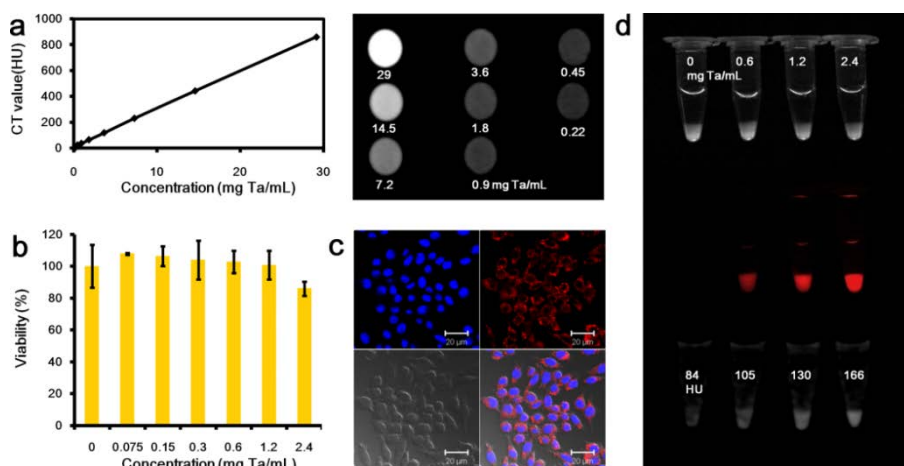
Figure 2.7. In vitro characterization of PEG-RITC-TaO$_x$. (a) HU measurements (left) and phantom CT image (right) of PEG-RITC-TaO$_x$ in water. (b) RAW264.7 cells (murine macrophages) were cultured with the nanoparticles of various concentrations. Cytotoxicity of the nanoparticles was determined by MTT assay. (c) CLSM images of RAW264.7 cells incubated with PEG-RITC-TaO$_x$ for 24 h (Scale bar: 20 μm). The nuclei were stained blue with 4'-6-diamidino-2-phenylindole (DAPI). (d) Cellular imaging results of RAW264.7 cells incubated with various concentrations of PEG-RITC-TaO$_x$. Bright field image (top), fluorescence image ($\lambda_{ex} = 550$ nm) (middle), and X-ray CT cell phantom image (numbers indicate CT values in HU) (bottom).

2.3.4 In vivo X-ray CT imaging

To perform in vivo X-ray CT imaging, PEG-RITC-TaO$_x$ (840 mg/kg) was injected intravenously into the tail vein of a rat. Distribution of the particles was tracked by X-ray CT imaging before injection as well as immediately, 5 min, 30 min, 1 h, 2 h, 3 h, and 24 h after injection (Figure 2.8a-b). Once the nanoparticles were injected, the vessels were preferentially enhanced, enabling spatially-described, volume-rendered images of the blood pool (Figure 2.8c and Supporting Information Movie 1). The enhancement continued for over 3 h, indicating long circulation of the particles. The nanoparticles eventually were accumulated by macrophages in the spleen and liver. The HU values of the blood vessels and heart reached maximum values immediately after injection and then decrease slowly, whereas the HU values of the liver and spleen gradually increased (Table 2.1).
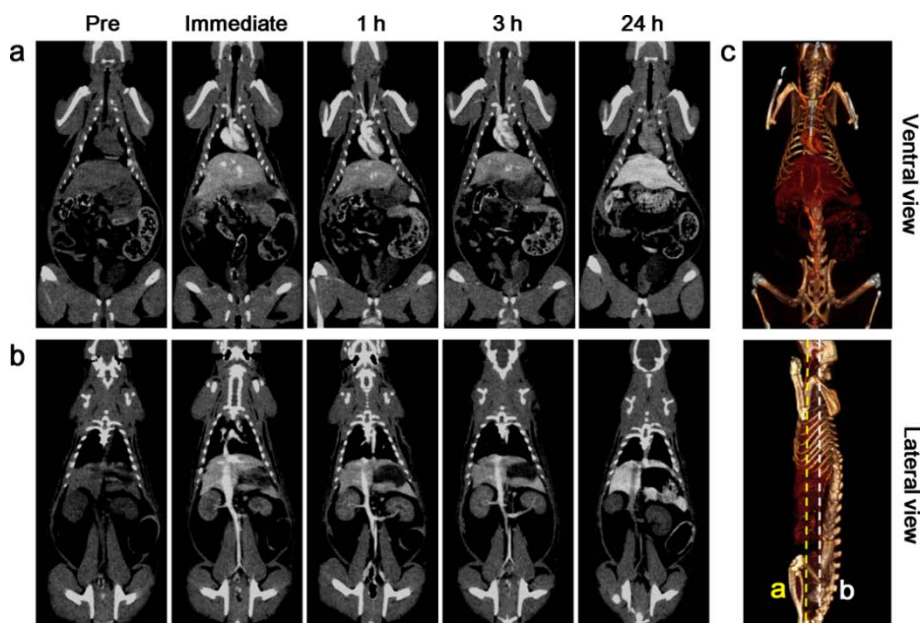
Figure 2.8. In vivo X-ray CT imaging. (a)-(b), Serial CT coronal views of a rat following injection of 1 mL of PEG-RITC-TaO$_x$ solution (840 mg/kg) into the tail vein. (a) heart and liver (coronal view cut along the yellow dotted line in (c)). (b) spleen, kidney, and inferior vena cava (coronal view cut along the white dotted line in (c)). (c) 3D-renderings of in vivo CT images reveal the ventral (top) and lateral (bottom) side of the heart and great vessels. The images were obtained immediately after injection.

	Previous	immediate	1 h	3 h	24 h
Heart	74	237	239	198	105
Liver	84	110	124	130	191
Kidney	61	95	80	93	80
Spleen	85	132	173	167	192
Inferior vena cava	64	232	234	217	103

Table 2.1. HU values of the heart, liver, kidney, spleen and inferior vena cava (IVC) before the injection (previous) and at indicated time intervals after the injection.

2.3.5 In vivo toxicity test

After 24 h of CT imaging, the rat was sacrificed, and the biodistribution of PEG-RITC-TaO$_x$ was visualized by fluorescence imaging of the dissected organs. CLSM images of the samples showed that most of the nanoparticles were found in the liver and spleen (Figure 2.9). To determine whether PEG-RITC-TaO$_x$ cause any harmful effects or any diseases in these organs, long term toxicity of the nanoparticles was investigated by monitoring histological changes in several organs, including the liver, spleen, heart, kidney and lung, for more than 2 weeks. Rats were dissected at 1 day, 3 day, 7 day, and 15 day after the injection of single dose (840 mg/kg) of PEG-RITC-TaO$_x$. hematoxylin and eosin (H&E) stains of their organs showed no evidence of adverse effect of the nanoparticles (Figure 2.10). Serum levels of alanine aminotransferase (ALT) and aspartate aminotransferase (AST) were also measured over time to determine the effect on liver function. The single dose injection induced transient increase of the serum level, which declined rapidly and returned to normal at day 3 (Figure 2.11).[17] These results demonstrate that tantalum oxide nanoparticles exhibit little toxicity on liver as well as other organs.
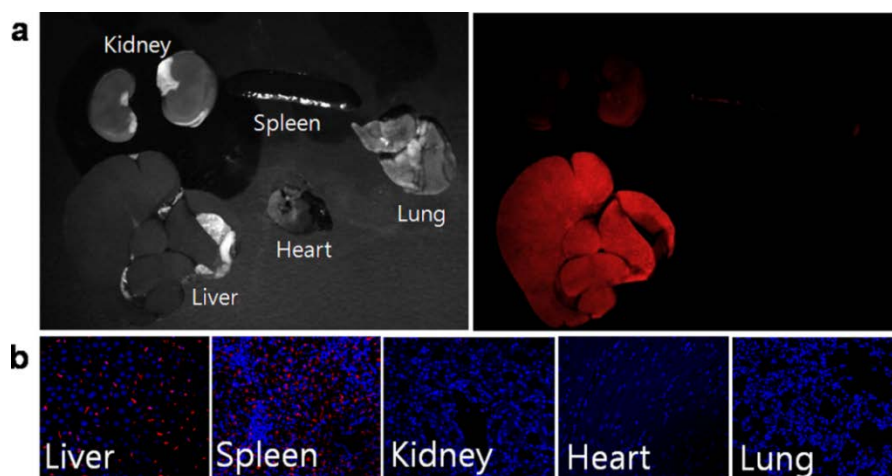
Figure 2.9. Biodistribution of PEG-RITC-TaO$_x$ by the fluorescence imaging of the liver, spleen, heart, kidney, and lung, harvested from the rat 24 h after intravenous injection. (a) photographic image (left) and corresponding fluorescence image (right) of the organs. (b) Confocal microscopy images of the corresponding tissue samples stained blue with 4'-6-diamidino-2-phenylindole (DAPI) showing existence of red-emitting PEG-RITC-TaO$_x$.
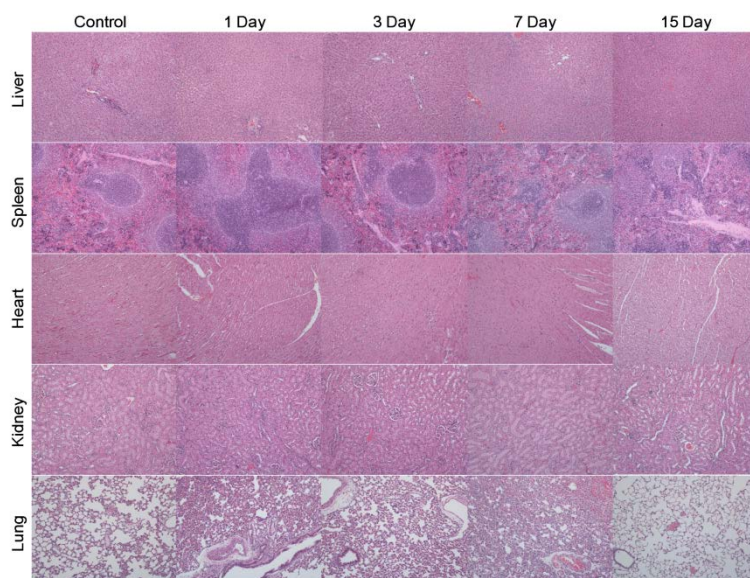
Figure 2.10. Time course of histological changes in the liver, spleen, heart, kidney, and lung of rats that received single intravenous injection of 1 ml of either PBS (control) or PEG-RITC-TaO$_x$ (840 mg/kg dose in PBS) followed by dissection at the indicated times. Sections were stained with H&E and observed under a light microscope at 100× magnification.
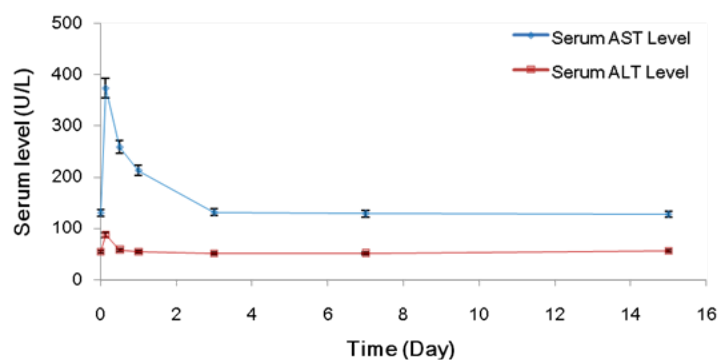
Figure 2.11. Changes in serum liver enzyme levels as a function of time. Time $= 0$ corresponds to the moment of single intravenous injection of PEG-RITC-TaO$_x$ in rats (840 mg/kg dose in 1 mL of PBS). Blue line indicates aspartate aminotransferase (AST) and red line shows alanine aminotransferase (ALT). Data presented as mean $\pm$ sem ($n = 4$). Data at time $= 0$ is saline control.

2.3.6 Sentinel lymph node imaging

Sentinel lymph node mapping is very important for the precise determination of tumor metastasis.[18] By precisely mapping the lymph nodes, unnecessary dissection from surgery can be avoided. To deliver the contrast agent to sentinel lymph nodes, 100 μL of PEG-RITC-TaO$_x$ solution was intradermally injected into the rats' paws. Two hours following injection, the locations of the lymph nodes were determined by X-ray contrast enhancement (Figure 2.12a). To investigate whether or not the resection of lymph nodes can be assisted by bimodal imaging, the locations of the lymph nodes were first determined using the volume-rendered CT images. Once a site was located, the area of the lymph nodes to be dissected was specified using fluorescence imaging during the operation, followed by successful extraction (Figure 2.12b). In the dissected lymph nodes, nanoparticles were found by fluorescence imaging, but no histological changes were observed by H&E staining (Figure 2.13).
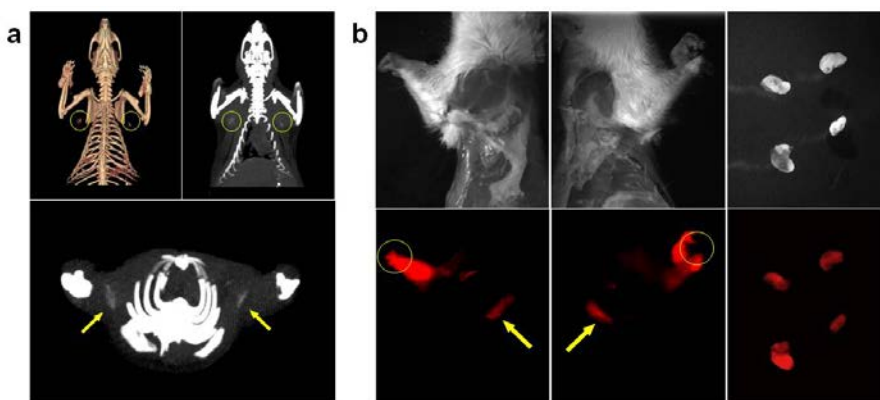
Figure 2.12. Sentinel lymph node mapping and resection. (a) In vivo CT volume-rendered (upper left) and maximum intensity projections (MIP) images (upper right and lower panels) of sentinel lymph node of the rat were obtained 2 hr after intradermal injection of 100 μL of PEG-RITC-TaO$_x$ solution (210 mg/mL) in both paws. The yellow circles and arrows indicate the locations of the lymph nodes. (b) White light photographs (upper panels) and fluorescence images (lower panels) of the rat injected intradermally with 100 μL of PEG-RITC-TaO$_x$ solution in both paws. Lateral views of the rat 2 h after injection show highly intense red emission from the lymph node and injected part (left and middle). Arrows and circles indicate the putative axillary sentinel lymph nodes and injection point, respectively. Sentinel lymph nodes of the two rats dissected by bimodal image-guided surgery (right).
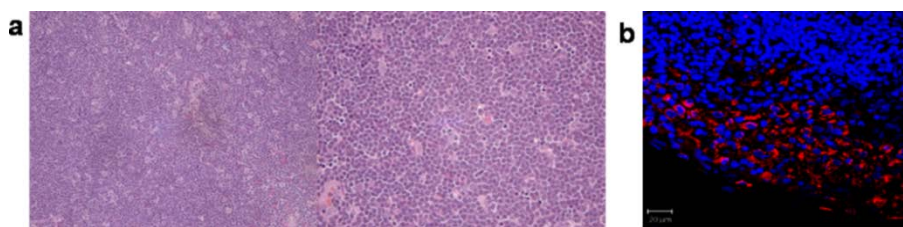
Figure 2.13. (a) Histological section of lymph node sample dissected by the bimodal image-guided surgery. Sections were stained with H&E and observed under a light microscope at 100× (left) and 400× (right) magnification. (b) Confocal microscopy image of the dissected lymph node stained blue with 4'-6-diamidino-2-phenylindole (DAPI) showing existence of PEG-RITC-TaO$_x$ emitting red fluorescence.

2.4 Conclusion

In conclusion, gram-scale synthesis of uniform-sized TaO_x nanoparticles was achieved using a simple microemulsion method. One-pot surface modification using various silane derivatives was successfully integrated to the microemulsion synthetic system, providing PEGylated and dye-immobilized TaO_x nanoparticles with anti-fouling and multimodal capabilities. In vivo X-ray CT imaging using RITC-conjugated and PEGylated TaO_x nanoparticles resulted in bright and well-resolved CT images with long circulation time. Time-course of histological studies and liver toxicity test revealed no adverse effect of the nanoparticles, possibly due to their bioinertness. Bimodal image-guided surgery using the particles was also advantageous in the resection of lymph nodes. These results clearly demonstrate that TaO_x nanoparticles can be used for various multifunctional medical applications. In terms of practical clinical application, tantalum oxide nanoparticles have potentials for angiography as well as RES-targeted imaging to improve the detection of metastases in the liver and limph nodes.

2.5 References

[1] (a) Alivisatos, A. P. *Nat. Biotechnol.* **2004**, *22*, 47. (b) Rosi, N. L.; Mirkin, C. A. *Chem. Rev.* **2005**, *105*, 1547. (c) Michalet, X.; Pinaud, F. F.; Bentolila, L. A.; Tsay, J. M.; Doose, S.; Li, J. J.; Sundaresan, G.; Wu, A. M.; Gambhir, S. S.; Weiss, S. *Science* **2005**, *307*, 538. (d) Weissleder, R.; Pittet, M. J. *Nature* **2008**, *452*, 580. (e) Selvan, S. T.; Patra, P. K.; Ang, C. Y.; Ying, J. Y. *Angew. Chem. Int. Ed.* **2007**, *46*, 2448. (f) Klostranec, J. M.; Chan, W. C. W. *Adv. Mater.* **2006**, *18*, 1953. (g) Kim, J.-W.; Galanzha, E. I.; Shashkov, E. V.; Moon, H.-M.; Zharov, V. P. *Nat. Nanotech.* **2009**, *4*, 688. (h) Lee, S.-M.; Park, H.; Yoo, K.-H. *Adv. Mater.* **2010**, *22*, 4049.

[2] (a) Barnett, B. P.; Arepally, A.; Karmarkar, P. V.; Qian, D.; Gilson, W. D.; Walczak, P.; Howland, V.; Lawler, L.; Lauzon, C.; Stuber, M.; Kraitchman, D. L.; Bulte, J. W. M. *Nat. Med.* **2007**, *13*, 986. (b) Choi, H. S.; Liu, W.; Liu, F.; Nasr, K.; Misra, P.; Bawendi, M. G.; Frangioni, J. V. *Nat. Nanotech.* **2010**, *5*, 42. (c) Kumar, R.; Roy, I.; Ohulchanskky, T. Y.; Vathy, L. A.; Bergey, E. J.; Sajjad, M.; Prasad, P. N. *ACS Nano* **2010**, *4*, 699. (d) Perrault, S. D.; Walkey, C.; Jennings, T.; Fischer, H. C.; Chan, W. C. W. *Nano Lett.* **2009**, *9*, 1909.

[3] (a) Larson, D. R.; Zipfel, W. R.; Williams, R. M.; Clark, S. W.; Bruchez, M. P.; Wise, F. W.; Webb, W. W. *Science* **2003***, 300*, 1434. (b) Medintz, I. L.; Uyeda, H. T.; Goldman, E. R.; Mattoussi, H. *Nat. Mater.* **2005**, *4*, 435. (c) Bakalova, R.; Zhelev, Z.; Aoki, I.; Kanno, I. *Nat. Photon.* **2007**, *1*, 487. (d) Bruchez Jr., M.; Moronne, M.; Gin, P.; Weiss, S.; Alivisatos, A. P. *Science* **1998**, *281*, 2013.

[4] (a) Bulte, J. W. M.; Kraitchman, D. L. *NMR Biomed.* **2004**, *17*, 484. (b) Laurent, S.; Forge, D.; Port, M.; Roch, A.; Robic, C.; Vander Elst, L.; Muller, R. N. *Chem. Rev*. **2008**, *108*, 2064. (c) Lin, W.; Hyeon, T.; Lanza, G. M.; Zhang, M.; Meade, T. J. *MRS Bull.* **2009**, *34*, 441. (d) Jun, Y.-W.; Lee, J.-H.; Cheon, J. *Angew. Chem. Int. Ed.* **2008**, *47*, 5122. (e) Na, H. B.; Hyeon, T. *J. Mater. Chem*. **2009**, *19*, 6267. (f) Na, H. B.; Song, I. C.; Hyeon, T. *Adv. Mater*. **2009**, *21*, 2133. (g) Jun, Y.-W.; Huh, Y.-M.; Choi, J.-S.; Lee, J.-H.; Song, H.-T.; Kim, S.; Yoon, S.; Kim, K.-S.; Shin, J.-S.; Suh, J.-S.; Cheon, J. *J. Am. Chem. Soc.* **2005**, *127*, 5732. (h) Lewin, M.; Carlesso, N.; Tung, C.-H.; Tang, X.-W.; Cory, D.; Scadden, D. T.; Weissleder, R. *Nat. Biotechnol.* **2000**, *18*, 410. (i) Lee, J.-H.; Huh, Y.-M.; Jun, Y.-W.; Seo, J.-W.; Jang, J.-T.; Song, H.-T.; Kim, S.; Cho, E.-J.; Yoon, H.-G.; Suh, J.-S.; Cheon, J. *Nat. Med.* **2007**, *13*, 95. (j) Gao, J.; Liang, G.; Cheung, J. S.; Pan, Y.; Kuang, Y.; Zhao, B. Z.; Zhang, X.; Wu, E. X.; Xu,

B. *J. Am. Chem. Soc.* **2008**, *130*, 11828.

[5] Schwenzer, N. F.; Springer, F.; Schraml, C.; Stefan, N.; Machann, J.; Schick, F. *J. Hepatol.* **2009**, *51*, 433.

[6] (a) Yu, S.; Watson, A. D. *Chem. Rev.* **1999**, *99*, 2353. (b) Frangioni, J. V. *Nat. Biotechnol.* **2006**, *24*, 909. (c) Gao, X.; Cui, Y.; Levenson, R. M.; Chung, L. W. K.; Nie, S. *Nat. Biotechnol.* **2004**, *22*, 969. (d) Xie, J.; Chen, K.; Lee, H.-Y.; Xu, C.; Hsu, A. R.; Peng, S.; Chen, X.; Sun, S. *J. Am. Chem. Soc.* **2008**, *130*, 7542. (e) Santra, S.; Bagwe, R. P.; Dutta, D.; Stanley, J. T.; Walter, G. A.; Tan, W.; Moudgil, B. M.; Mericle, R. A. *Adv. Mater.* **2005**, *17*, 2165. (f) Prencipe, G.; Tabakman, S. M.; Welsher, K.; Liu, Z.; Goodwin, A. P.; Zhang, L.; Henry, J.; Dai, H. *J. Am. Chem. Soc.* **2009**, *131*, 4783. (g) Sun, I.-C. et al. *Chem. Eur. J.* **2009**, *15*, 13341.

[7] (a) Kim, D.; Park, S.; Lee, J. H.; Jeong, Y. Y.; Jon, S. Y. *J. Am. Chem. Soc.* **2007**, *129*, 7661. (b) Rabin, O.; Perez, J. M.; Grimm, J.; Wojtkiewicz, G.; Weissleder, R. *Nat. Mater.* **2006**, *5*, 118. (c) Popovtzer, R.; Agrawal, A.; Kotov, N. A.; Popovtzer, A.; Balter, J.; Carey, T. E.; Kopelman, R. *Nano Lett.* **2008**, *8*, 4593. (d) Kattumuri, V.; Katti, K.; Bhaskaran, S.; Boote, E. J.; Casteel, S. W.; Fent, G. M.; Roberston, D. J.; Chandrasekhar, M.; Kannan, R.; Katti, K. V. *Small* **2007**, *3*, 333.

[8] (a) deKrafft, K. E.; Xie, Z.; Cao, G.; Tran, S.; Ma, L.; Zhou, O. Z.; Lin, W.

Angew. Chem. Int. Ed. **2009**, *48*, 9901. (b) Pan D.; Williams, T. A.; Senpan, A.; Allen, J. S.; Scott, M. J.; Gaffney, P. J.; Wickline, S. A.; Lanza, G. M. *J. Am. Chem. Soc.* **2009**, *131*, 15522. (c) Hyafil, F.; Cornily, J.-C.; Feig, J. E.; Gordon, R.; Vucic, E.; Amirbekian, V.; Fisher, E. A.; Fuster, V.; Fledman, L. J.; Fayad, Z. A. *Nat. Med.* **2007**, *13*, 636. (d) Alric, C.; Taleb, J.; Duc, G. L.; Mandon, C.; Billotey, C.; Meur-Herland, A. L.; Brochard, T.; Vocanson, F.; Janier, M.; Perriat, P.; Roux, S.; Tillement, O. *J. Am. Chem. Soc.* **2008**, *130*, 5908. (e) Bhang, S. H.; Won, N.; Lee, T.-J.; Jin, H.; Nam, J.; Park, J.; Chung, H.; Park, H.-S.; Sung, Y.-E.; Hahn, S. K.; Kim, B.-S.; Kim, S. *ACS Nano* **2009**, *3*, 1389. (f) Gao, J.; Zhang, B.; Gao, Y.; Pan, Y.; Zhang, X.; Xu, B. *J. Am. Chem. Soc.* **2007**, *129*, 11928. (g) Xu, C.; Xie, J.; Ho, D.; Wang, C.; Kohler, N.; Walsh, E. G.; Morgan, J. R.; Chin, Y. E.; Sun, S. *Angew. Chem. Int. Ed.* **2007**, *47*, 173. (h) Cheon, J.; Lee, J.-H. *Acc. Chem. Res.* **2008**, *41*, 1630.

[9] (a) Black, J. *Clin. Mater.* **1994**, *16*, 167. (b) Matsuno, H.; Yokoyama, A.; Watari, F.; Uo, M.; Kawasaki, T. *Biomaterials* **2001**, *22*, 1253. (c) Kato, H.; Nakamura, T.; Nishiguchi, S.; Matsusue, Y.; Kobayashi, M.; Miyazaki, T.; Kim, H.-M.; Kokubo, T. *J. Biomed. Mater. Res.* **2000**, *53*, 28. (d) Sharma, C. P.; Paul, W. *J. Biomed. Mater. Res.* **1992**, *26*, 1179. (e) Miller, A. C.; Fuciarelli, A. F.; Jackson, W. E.; Ejnik, E. J.; Emond, C.;

Strocko, S.; Hogan, J.; Page, N.; Pellmar, T. *Mutagenesis* **1998**, *13*, 643. (f) Johnson, P. F.; Bernstein, J. J.; Hunter, G.; Dawson, W. W.; Hench, L. L. *J. Biomed. Mater. Res.* **1977**, *11*, 637. (g) Zitter, H.; Plenk Jr., H. *J. Biomed. Mater. Res.* **1987**, *21*, 881. (h) Chen, J. Y.; Leng, Y. X.; Tian, X. B.; Wang, L. P.; Huang, N.; Chu, P.K.; Yang, P. *Biomaterials* **2002**, *23*, 2545. (i) Findlay, D. M.; Welldon, K.; Atkins, G. J.; Howie, D. W.; Zannettino, A. C. W.; Bobyn, D. *Biomaterials* **2004**, *25*, 2215.

[10] Bonitatibus Jr., P. J.; Torres, A. S.; Goddard, G. D.; FitzGerald, P. F.; Kulkarni, A. M. *Chem. Commun.* **2010**, *46*, 8956.

[11] (a) Kim, S.; Lim, Y. T.; Soltesz, E. G.; Grand, A. M. D.; Lee, J.; Nakayama, A.; Parker, J. A.; Mihaljevic, T.; Laurence, R. G.; Dor, D. M.; Cohn, L. H.; Bawendi. M. G.; Frangioni, J. V. *Nat. Biothechnol.* **2004**, *22*, 93. (b) Kobayashi, H.; Hama, Y.; Koyama, Y.; Barrett, T.; Regino, C. A. S.; Urano, Y.; Choyke, P. L. *Nano Lett.* **2007**, *6*, 1711.

[12] (a) Chang, C.; Fogler, S. *Langmuir* **1997**, *13*, 3295. (b) Arriagada, F. J.; Osseo-asare, K. *J. Colloid Interface Sci.* **1999**, *211*, 210..

[13] (a) Xu, C.; Tung, G. A.; Sun, S. *Chem. Mater.* **2008**, *20*, 4167. (d) Burns, A. A.; Vider, J.; Ow, H.; Herz, E.; Penate-Medina, O.; Baumgart, M.; Larson, S. M.; Wiesner, U.; Bradbury, M. *Nano Lett.* **2009**, *9*, 442. (c) Chithrani, B. D.; Chan, W. C. W. *Nano Lett.* **2007**, *7*, 1542.

[14] Ogihara, T.; Ikemoto, T.; Mizutani, N.; Kato, M. *J. Mater. Sci.* **1986**, *21*, 2771.

[15] (a) Tan, W.; Wang, K.; He, X.; Zhao, X. J.; Drake, T.; Wang, L.; Bagwe, R. P. *Med. Res. Rev.* **2004**, *24*, 621.(b) Ow, H.; Larson, D. R.; Srivastava, M.; Baird, B. A.; Webb, W. W.; Wiesner, U. *Nano Lett.* **2005**, *5*, 113. (c) Burns, A.; Ow, H.; Wiesner, U. *Chem. Soc. Rev.* **2006**, *35*, 1028. (d) Kim, J.; Kim, H. S.; Lee, N.; Kim, T.; Kim, H.; Yu, T.; Song, I. C.; Moon, W. K.; Hyeon, T. *Angew. Chem. Int. Ed.* **2008**, *47*, 8438. (e) Piao, Y.; Burns, A.; Kim, J.; Wiesner, U.; Hyeon, T. *Adv. Funct. Mater.* **2008**, *18*, 3745. (f) Kim, J.; Piao, Y.; Hyeon, T.; *Chem. Soc. Rev.* **2009**, *38*, 372. (g) Lee, J. E.; Lee, N.; Kim, H.; Kim, J.; Choi, S. H.; Kim, J. H.; Kim, T.; Song, I. C.; Park, S. P.; Moon, W. K.; Hyeon, T. *J. Am. Chem. Soc.* **2009**, *132*, 552.

[16] Schulz, H.; Pratsinis, S. E.; Rüegger, H.; Zimmermann, J.; Klapdohr, S.; Salz, U. *Colloids Surf. A* **2008**, *315*, 79.

[17] (a) Jain, T. K.; Reddy, M. K.; Morales, M. A.; Leslie-Pelecky, D. L.; Labhasetwar, V. *Mol. Pharm.* **2008**, *5*, 316. (b) Hainfeld, J. F.; Slatkin, D. N.; Focella, T. M.; Smilowitz, H. M. *Br. J. Radiol.* **2006**, *79*, 248.

[18] Harisinghani, M. G.; Barentsz, J.; Hahn, P. F.; Deserno, W. M.; Tabatabaei, S.; van de Kaa, C. H.; de la Rosette, J.; Weissleder, R. *N. Engl. J. Med.* **2003**, *348*, 2491.

Chapter 3. Multifunctional Fe_3O_4/TaO_x Core/Shell Nanoparticles for Simultaneous Magnetic Resonance Imaging and X-ray Computed Tomography

3.1 Introduction

Nanoparticles have been intensively studied for their scientific interests and for potential applications due to their unique electric, magnetic, and optical properties and their versatile functionality.[1] Biomedical applications of nanoparticles have attracted considerable attention because nanoparticles are expected to improve the medical diagnosis and treatment.[2] Properly stabilized nanoparticles smaller than 200 nm have prolonged circulation times, and they accumulate at tumors because of leaky vasculature and poor lymphatic drainage, which is referred to as the enhanced permeation and retention (EPR) effect.[3] Various nanoparticles have been used as imaging contrast agents for fluorescence imaging, magnetic resonance imaging (MRI), computed tomography (CT), photoacoustic tomography (PAT), and

surface-enhanced Raman scat-tering.[4] Each imaging modality has its own advantages and limitations.[5] For example, CT is advantageous in regards to its high resolution and ease of forming 3D visual reconstruction of tissues of interest, but its inherent low sensitivity results in poor soft tissue contrast. T_2-weighted MRI using magnetic nanoparticles as contrast agents exhibits high sensitivity and excellent soft tissue contrast,[6] but intrinsic dark signals of contrast agents are sometimes confused with other hypointense areas, such as those resulting from air, bleeding, calcification, and metal deposition.[7] Multimodal imaging can overcome these limitations by combining the advantages of each modality.[8] Because nanoparticles can be easily modified or immobilized with biomolecules, fluorescence dyes, and radioisotopes, multifunctional nanoprobes for multimodal imaging can be readily developed.[9] However, most of the previously reported multifunctional nanoprobes were used for simultaneous imaging of the same region of interest; complementary information of each modality has not yet been demonstrated.

A recently reported TaO_x nanoparticle-based CT contrast agent[10] is very promising for clinical applications compared to other nanoparticulate CT contrast agents such as Au and Bi_2S_3 because of its

low cost and high biocompatibility.[4c,11] In this paper, we report on the synthesis of multifunctional Fe_3O_4/TaO_x core/shell nanoparticles and bimodal CT-MR imaging using these nanoparticles. MRI enables sensitive imaging of the tumor microenvironment, whereas CT images display the tumor-associated blood vessels.

3.2 Experimental Section

3.2.1 Synthesis of Fe₃O₄ nanoparticles

Iron oxide nanoparticles were synthesized according to the previously reported procedure with a little modification.[22] 36 g of iron-oleate complex (40 mmol), 10.4 g of oleic acid (40 mmol, 90%, Aldrich), and 200 g of dioctyl ether (95%, Aldrich) were added in 1 L reactor and mixed at room temperature. The reaction mixture was degassed at 90 °C under vacuum for 2 h. The mixture was heated to 287 °C with a constant heating rate of 3.3 °C/min, and then kept at that temperature for 30 min under inert atmosphere. The resulting solution containing the nanoparticles was then slowly cooled to approximately 150 °C, and the solution was exposure to air to increase the crystallinity of the nanoparticles for 2 hr. Subsequently, 700 ml of acetone was added to the solution to precipitate the nanoparticles. The nanoparticles were separated by discarding supernatant and dispersed in hydrophobic solvent such as n-hexane or chloroform. Finally the iron oxide nanoparticles were redispersed in cyclohexane with concentration of 20 mg/ml.

3.2.2 Synthesis of Fe$_3$O$_4$/TaO$_x$ core/shell nanoparticles

Microemulsion was prepared by adding 5 ml of NaOH aqueous solution (75 mM) to the oil phase composed of 8 ml cyclohexane containing Fe$_3$O$_4$ nanoparticles, 46 g of Igepal CO-520 (Aldrich), 5mL of ethanol (Samchun, 99.9%), and 800 ml of cyclohexane (Samchun, 99.5%). After 1 mL of tantalum(V) ethoxide (0.3 mmol, Strem, 99.8%) was added to the mixture at room temperature, Fe$_3$O$_4$/TaO$_x$ core/shell nanoparticles were synthesized within 5 min.

To prepare rhodamine-B-isothiocyanate (RITC)-functionalized silane, 110 µl of aminopropyltriethoxysilane (APTES, Aldrich) was reacted with 50 mg of RITC in 3.75 ml of ethanol at room temperature for 24 h. The 1.5ml of resulting solution and 5 ml of 2-methoxy(polyethyleneoxy)propyl trimethoxysilane (PEG-silane, Gelest, 596-725 Da) was added to 1 L of the as-prepared mixture containing Fe$_3$O$_4$/TaO$_x$ core/shell nanoparticles. The mixture was then stirred at room temperature for 24 h, becoming a red turbid solution. The resulting solution was evaporated at 60 °C until the solution became transparent, after which the functionalized Fe$_3$O$_4$/TaO$_x$ core/shell nanoparticles were precipitated by adding a mixed solution of 1:1 (v/v) ether/n-hexane. The precipitates were purified with ether and dispersed

in ethanol. To this solution was added 40 mg of methoxypoly(ethylene glycol) succinimidylglutarate (mPEG-SG, MW 2000, Sunbio). The mixture was stirred overnight at 30 °C to conjugate PEG onto residual amine groups on the surface of the functionalized Fe_3O_4/TaO_x core/shell nanoparticles. After being washed several times with deionized water, the final product was dispersed in phosphate buffered saline (PBS) buffer.

3.2.3 Characterization of Fe_3O_4/TaO_x core/shell nanoparticles

Transmission electron microscopy (TEM) images were taken on a JEOL JEM-2010 electron microscope at 200 kV. The elemental mapping was performed using a FEI Technai F20 scanning transmission electron microscope equipped with EELS detector. Samples were prepared by dropping small volume of particle dispersion onto a carbon-coated copper grid. The hydrodynamic diameters of nanoparticles were measured with a particle size analyzer (ELS-Z2, Otsuka). M–H curves were obtained by the vibrating sample magnetometer (VSM, Quantum Design PPMS). The iron and tantalum concentrations of nanoparticles were measured with inductively coupled plasma atomic emission spectroscopy (ICP-AES, Optima-4300

DV, PerkinElmer).

3.2.4 CT/MR imaging of Phantom

Various concentrations of Fe_3O_4/TaO_x core/shell nanoparticles dispersed in deionized water were prepared in 1.5 ml microtubes. CT images were acquired using a dual-source CT system (Somatom Definition, Simens). Imaging parameters were as follows: thickness, 1 mm; pitch, 1; 120 kVp, 92 mA; field of view, 86×86; gantry rotation time, 0.5 s; table speed, 6 mm/s. T_2 values of nanoparticles were measured using the Carr-Purcell-Meiboom-Gill (CPMG) sequence with a head coil on a 3-T MR scanner (TrioTrim, Siemens): $T_R = 5000$ ms, $T_E = 16, 32, 48, 64, 20, 40, 60, 80, 50, 100, 150, 200$ ms. Fast spin echo T_2-weighted MR images of the phantom were acquired using the following parameters: flip angle = 120, ETL = 18, TR = 6000 ms, TE = 93 ms, field of view FOV = 108×180 mm^2, matrix = 384×640, slice thickness / gap = 2 mm / 2.6 mm, NEX = 1.

3.2.5 Cytotoxicity and cellular uptake of Fe_3O_4/TaO_x core/shell nanoparticles

RAW 264.7 murine macrophage cells were grown in Dulbecco's

Modified Eagle's Medium (DMEM, Welgene) supplemented with 10% (v/v) fetal bovine serum (FBS, Gibco) and penicillin/streptomycin (100 U/mL and 100 mg/ml, respectively, Gibco) at 37 $^{\circ}$C in humidified 5% CO_2 atmosphere.

The viability of the cells in the presence of Fe_3O_4/TaO_x core/shell nanoparticles was evaluated using 3-[4,5-dimethylthialzol-2-yl]-2,5-diphenyltetrazolium bromide (MTT, Sigma) assay. The assay was performed in triplicate in the following manner. For MTT assay, the cells were seeded into 96-well plates at a density of 1×10^4 per well in 200 μl of media and grown overnight. The cells were then incubated at various concentrations of media for 24 h. Following this incubation, the cells were incubated in media with 0.1 mg/ml of MTT for 1 h. Then the MTT solution was removed and the precipitated violet crystals were dissolved in 200 μl of DMSO. The absorbance was measured at 560 nm with VersaMax^{TM} microplate reader (Molecular Devices).

To observe cellular uptake of nanoparticles, the cells were cultured in a 4-well chamber slide (Nalgen Nunc, Naperville, IL) and incubated with Fe_3O_4/TaO_x core/shell nanoparticles. After 24 h, the cells were washed with phosphate buffered saline (PBS), fixed with 4% paraformaldehyde, and stained with 4′,6-diamidino-2-phenylindole

(DAPI, 1 µg/mL in PBS, Roche). The fluorescence images were acquired with confocal laser scanning microscopy (LSM 510, Carl Zeiss, Germany).

3.2.6 In vitro imaging

To label the cells with Fe_3O_4/TaO_x core/shell nanoparticles, the cells were seeded onto culture dishes in 10 ml of media and grown overnight. Subsequently, various concentrations of nanoparticles were added. After 24 h, the cells were washed twice with PBS and detached by adding 1 mL of trypsin/EDTA (Gibco). Cell pellets were prepared by centrifugation at 2000 rpm for 5 min. MR and CT imaging were performed using the same condition of the phantom.

3.2.7 In vivo imaging

All procedures were approved by the Institutional Animal Care and Use Committee (IACUC) of the Clinical Research Institute of Seoul National University Hospital, and all experimental procedures were performed according to IACUC guidelines. MAT B III rat mammary adenocarcinoma cells were cultured in sterile petri dishes containing RPMI-160 (Welgene) supplemented with 10% (v/v) fetal bovine serum

(FBS, Gibco) and penicillin/streptomycin (100 U/mL and 100 µg/ml, respectively, Gibco) at 37 $^{\circ}$C in humidified 5% CO_2 atmosphere.

MAT B III cells (5×10^5) in 100 µl of serum-free media were mixed with an equivalent volume of matrigel (BD Biosciences) at 4 °C, followed by subcutaneous injection into the flank of Fisher 344 rats. After 1~2 weeks, in vivo CT images and gradient T_2^*-MR images of the rat were acquired using a clinical CT scanner (Brilliance 64, Philips Medical System) and a 3-T MRI scanner (TrioTrim, Siemens) with a home-made 6-channnel animal coil before and after the injection of Fe_3O_4/TaO_x core/shell nanoparticles (840 mg/kg) into the tail vein. Imaging parameters of CT were as follows: thickness, 0.7 mm; pitch, 0.648; 120 kVp, 216 mA; field of view, 108×108; gantry rotation time, 0.75 s; table speed, 16.7 mm/s. Thin-section axial images were reformed to coronal images through a computational technique referred to as multiplanar reconstruction (MPR). The three-dimensional (3-D) reconstructed images were obtained using OsiriX (version 4.0; 32 bit; OsiriX foundation, Geneva). Imaging parameters of MR were as follows: flip angle = 12, ETL = 1, TR = 40 ms, TE = 22 ms, field of view FOV = 64×80 mm^2, matrix = 204×256, slice thickness / gap = 1 mm / 0 mm, NEX = 2.

3.2.8 Histochemical analysis

After CT/MR imaging, the rats were sacrificed under anesthetic conditions, and tissues of interest (tumor, kidney, liver, spleen, and heart) were excised and fixed in 10% neutral buffered formalin (10% NBF) for 1 week. For haematoxylin and eosin (H&E) staining, formalin fixed tissues from each organ were embedded into paraffin and paraffin-embedded tissues were sectioned into 4 μm thickness. Tissues samples were dewaxed, hydrated and standard H&E staining was performed to evaluate morphological features of each organs. Stained images were acquired with optical microscope (BX53P, Olympus, Japan). For fluorescence staining, tissues fixed with formalin were frozen with liquid nitrogen and cryosectioned into 10 μm thickness. Samples were immersed with 4'-6-diamidino-2-phenylindole (DAPI) for 5 minutes at room temperature to visualize the nucleus of cells and images were acquired with fluorescence microscope (Leica DM2500, Leica, Germany).

3.3 Result and Discussion

3.3.1 Synthesis and characterizartion of the Fe_3O_4/TaO_x core/shell nanoparticles

  The overall synthetic procedure of the Fe_3O_4/TaO_x core/shell nanoparticles is shown in Figure 3.1. Fe_3O_4 nanoparticles with average size of 8 nm, stabilized with oleic acid, were synthesized by thermal decomposition of iron oleate complex using the previously reported procedure with a slight modification (Figure 3.2a).[12] Subsequently, the nanoparticles were incorporated into the reverse micelles through mixing with cyclohexane, ethanol, NaOH, and Igepal CO-520. The addition of tantalum (V) ethoxide to the mixture initiated the controlled sol-gel reaction at room temperature and led to the formation of TaO_x shells within 5 min.[10] Finally, the nanoparticles were modified with rhodamine-B-isothiocyanate (RITC) functionalized silane and polyethylene glycol (PEG) silane via a sol-gel reaction between hydroxyl groups on the TaO_x surface and silane agents; this process endows the nanoparticles with fluorescence imaging capability, colloidal stability, and biocompatibility. Figure 3.2b presents a transmission electron microscopy (TEM) image of synthesized

Fe_3O_4/TaO_x core/shell nanoparticles. Because it is difficult to confirm the core/shell structure with normal TEM images owing to the high electron density of Ta, the Fe core was confirmed through electron energy-loss spectrum (EELS) mapping analysis.
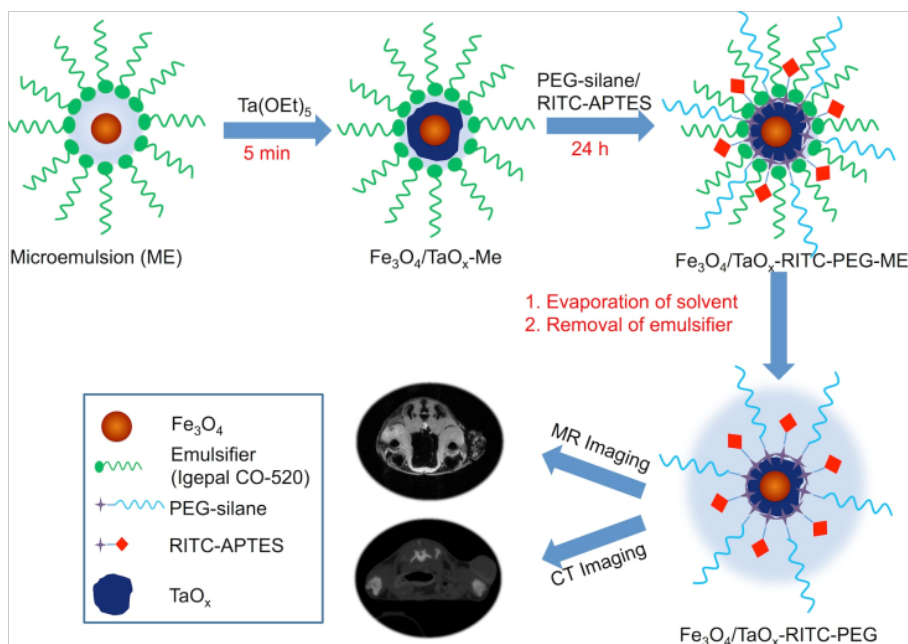
Figure 3.1. Schematic Illustration of Synthesis and Modification of Fe$_3$O$_4$/TaO$_x$ Core/Shell Nanoparticles.
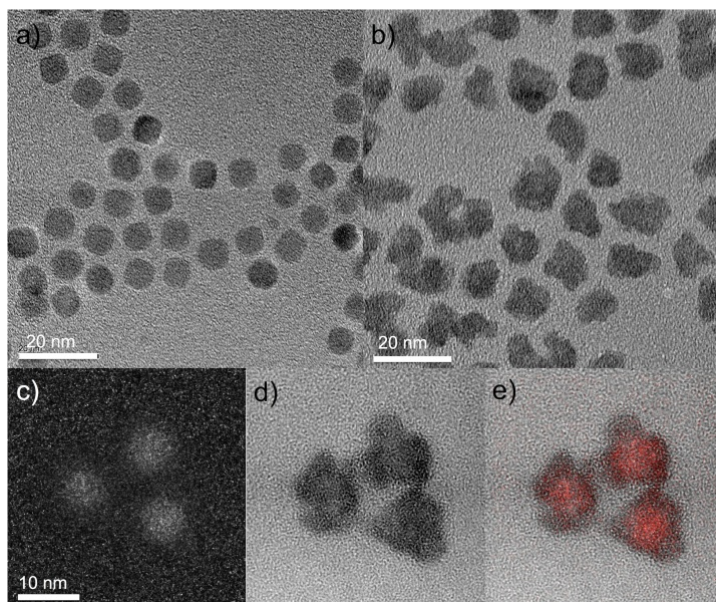
Figure 3.2. TEM images of Fe_3O_4 nanoparticles prepared via thermal decomposition of Fe-oleate complexes (a) and Fe_3O_4/TaO_x core/shell nanoparticles (b) prepared with Fe_3O_4 nanoparticles as cores. (c) Elemental mapping image for Fe. (d) Bright field TEM image of Fe_3O_4/TaO_x core/shell nanoparticles. (e) Overlay image of (c) and (d).

In the EELS-mapped image of Fe (Figure 3.2c), spherical nanoparticles with a size of 8 nm were observed, and this agreed very well with the TEM image of the Fe_3O_4 nanoparticles. The superimposed image (Figure 3.2e) of the elemental mapping image (Figure 3.2c) on the high resolution TEM image (Figure 3.2d) shows that Fe is present mainly in the core region. The incorporation of Fe_3O_4 nanoparticles into reverse micelles did not seem to affect the structure of the microemulsion, and the size and shape of the resulting nanoparticles were similar up to an Fe_3O_4 nanoparticle concentration of 0.4 mg/ml (Figure 3.3). Some free TaO_x nanoparticles that did not contain Fe_3O_4 nanoparticles were also obtained at low Fe_3O_4 nanoparticle concentrations (Figure 3.4). Because of the high sensitivity of MRI compared to CT, Fe_3O_4/TaO_x core/shell nanoparticles containing TaO_x nanoparticles that were synthesized at an Fe_3O_4 nanoparticle concentration of 0.2 mg/ml, were used for the subsequent studies.
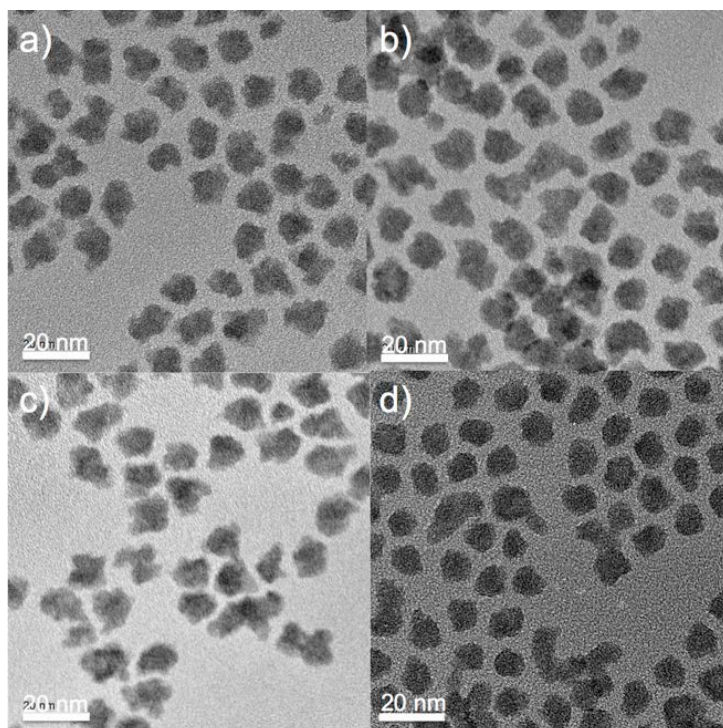
Figure 3.3. TEM images of Fe_3O_4/TaO_x core/shell nanoparticles synthesized with 0 (a), 0.05 (b), 0.1 (c), and 0.4 mg/ml (d) of Fe_3O_4 nanoparticles.
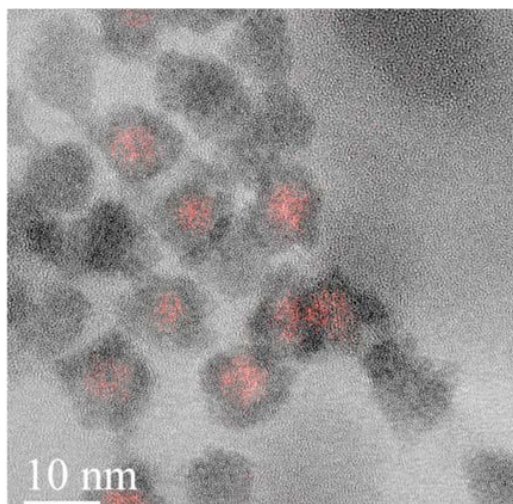
Figure 3.4. Overlay image of bright field TEM image and elemental mapping of Fe (red) for Fe_3O_4/TaO_x core/shell nanoparticles synthesized with 0.2 mg/ml of Fe_3O_4 nanoparticles. Some TaO_x nanoparticles that do not contain Fe core are observed.

The Fe_3O_4/TaO_x core/shell nanoparticles exhibited excellent colloidal stability in aqueous media owing to their stabilization by PEG. The hydrodynamic diameter of the nanoparticles measured using dynamic light scattering (DLS) was approximately 21 nm in water (Figure 3.5a), and no aggregation was observed over 1 month. The field-dependent magnetization curve of the Fe_3O_4/TaO_x core/shell nanoparticles shows that the nanoparticles are superparamagnetic at room temperature, which is an important characteristic for T_2 MR contrast agents (Figure 3.5b). The nanoparticles exhibit the emission peak of Rhodamine B at 580 nm, demonstrating their potential for fluorescence imaging (Figure 3.5c).
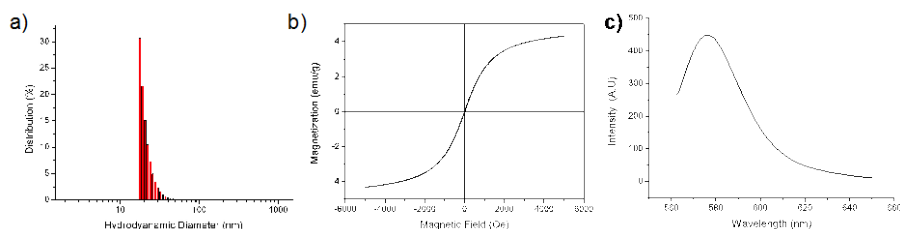
Figure 3.5. (a) Hydrodynamic diameter of Fe_3O_4/TaO_x core/shell nanoparticles in water. (b) Field-dependent magnetization of Fe_3O_4/TaO_x core/shell nanoparticles at room temperature. (c) Fluorescence spectrum of Fe_3O_4/TaO_x core/shell nanoparticles conjugated with RITC.

3.3.2 X-ray CT images and MR images of the phantom

    X-ray CT images and MR images of the phantom were obtained with various concentrations of Fe_3O_4/TaO_x core/shell nanoparticles dispersed in deionized water. In the CT images, the signal increased linearly as the concentration of nanoparticles increased (Figures 3.6a, 3.6b). T_2-weighted MR images of the same phantom were acquired using a 3-T MR scanner. As the concentration of the nanoparticles increased, their signal intensity significantly decreased (Figure 3.6c). The measured r2 value was 81.156 $mM^{-1}s^{-1}$ (Figure 3.6d). Whereas the signal intensity of the CT image continuously increased without saturation, the T_2 contrast effect of the nanoparticles saturated at a concentration of 0.05 mg Fe/ml and further signal attenuation was not observed above this concentration. However, sufficient T_2 contrast effect was observed at low concentration owing to the high sensitivity of MRI.
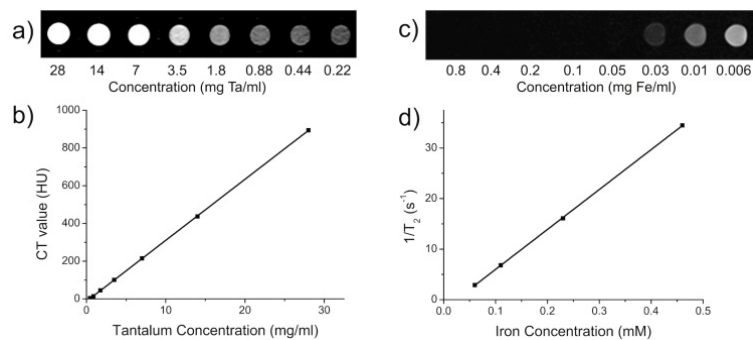
Figure 3.6. (a) CT phantom image of various concentrations of Fe_3O_4/TaO_x core/shell nanoparticles and (b) their HU values. (c) T_2-weighted MR image of the same phantom and (d) their R2 ($1/T_2$) values.

3.3.3 Cytotoxicity and cellular uptake of Fe₃O₄/TaOx nanoparticles

The cytotoxicity of Fe_3O_4/TaO_x nanoparticles was evaluated with a 3-[4,5-dimethylthialzol-2-yl]-2,5-diphenyltetrazolium bromide (MTT) assay using a murine macrophage cell line (RAW 264.7). The macrophage cell line was chosen because most administered foreign materials are cleared by professional phagocytes of the monocyte/macrophage lineage.[13] No appreciable toxicity was observed up to a concentration of 4.3 mg/ml (Figure 3.7a). This high biocompatibility is a great advantage of Fe_3O_4/TaO_x nanoparticles. Although FePt nanoparticles[14] and Gd-chelate coated gold nanoparticles[11c] were used for dual modal CT/MRI, these nanoparticles have inherent limitations in clinical applications because leached Pt or Gd ions are known to be toxic.[15,16] In contrast, Fe_3O_4 and TaO_x are biocompatible materials and have been clinically used as MR contrast agents and stents, respectively.[17]

Cellular uptake was investigated after incubating RAW 264.7 cells with Fe_3O_4/TaO_x core/shell nanoparticles for 24 h. The internalized nanoparticles were observed in the cytoplasm as red fluorescence (Figure 3.7b). After cellular uptake was confirmed, in vitro CT and MR images of the cells incubated with various concentrations of the

nanoparticles were obtained. As the concentration increased, the signals of the cells increased and decreased in CT images and MR images, respectively (Figures 3.7c, 3.7d).
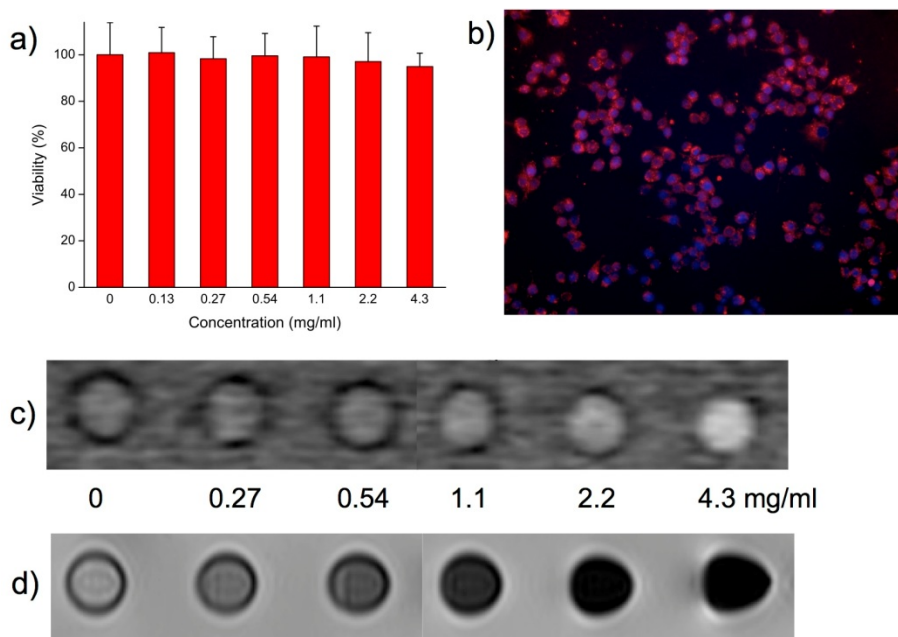
Figure 3.7. (a) Cytotoxicity of the nanoparticles determined by MTT assay (n=3). (b) Fluorescence microscope image of RAW 264.7 cells incubated with Fe_3O_4/TaO_x core/shell nanoparticles for 24 h. In vitro CT image (c) and MR image (d) of RAW 264.7 cells incubated with various concentrations of core/shell nanoparticles for 24 h.

3.3.4 In vivo bimodal CT/MR imaging of the tumor

To assess the feasibility of in vivo bimodal CT/MR imaging of the tumor, rats were subcutaneously inoculated with rat mammary adenocarcinoma cells (MAT B III). The tumors were allowed to grow to a size of approximately 1 cm in diameter, resulting in an inhomogeneous interior. Subsequently, Fe_3O_4/TaO_x core/shell nanoparticles (840 mg/kg) were injected intravenously into the tail veins of the rats. Dual MR/CT imaging was performed using a clinical CT and MR scanner before and after tail vein injection of the nanoparticles. After administration of the nanoparticles, preferential signal enhancement of blood vessels, including the tumor-associated vessel, was observed in volume-rendered CT images (Figures 3.8, 3.9). The signal of the blood vessels persisted for more than 2 h owing to the long circulation of the nanoparticles (Figures 3.8b, 3.8c). Three-dimensional imaging of the blood vessels using CT imaging is advantageous for tumor therapy because the tumor-associated vessel is one of the main targets in effective cancer treatment.[18] Despite the high sensitivity of T_2-weighted MR imaging, blood pool imaging is known to be difficult because T_2 contrast agents reduce the signal of the region of interest. The nanoparticles were accumulated at the tumor via

the EPR effect and cleared by reticuloendothelial systems (RES). Consequently, the HU values of blood vessels decreased slowly, while those of the tumor, liver, and spleen gradually increased (Table 3.1). However, in contrast with the liver and spleen, the exact shape and structure of the tumor were not revealed owing to the low sensitivity of CT and the inhomogeneous distribution of the nanoparticles.
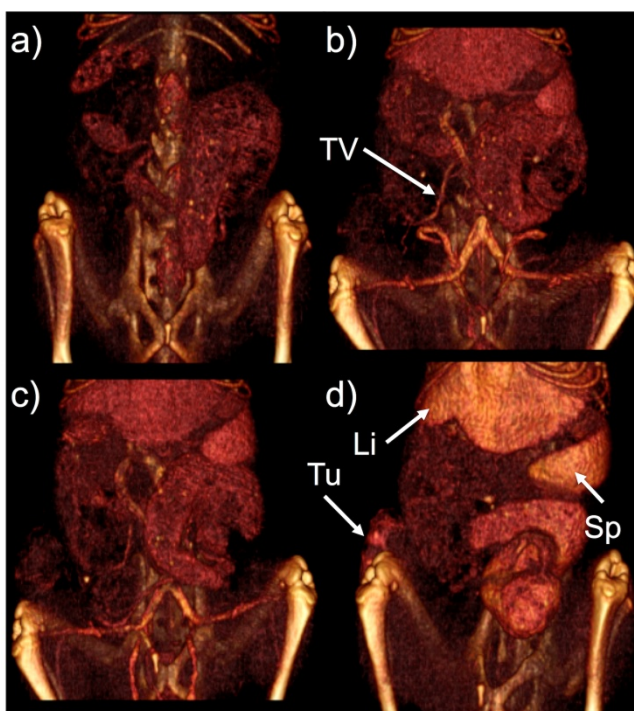
Figure 3.8. In vivo X-ray CT images of the rat before (a) and 1 h (b), 2 h (c), and 24 h (d) after the injection of Fe_3O_4/TaO_x core/shell nanoparticles (840 mg/kg). TV, Li, Tu, and Sp indicate the tumor-associated vessel, liver, tumor, and spleen, respectively.
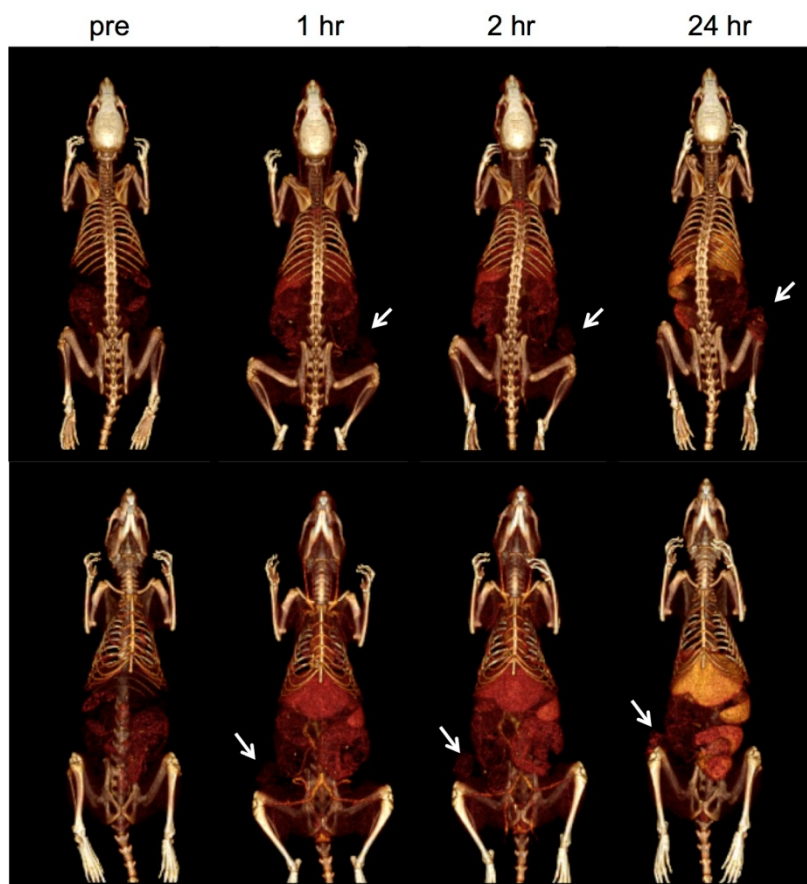
Figure 3.9. X-ray CT images of whole-body. White arrows indicate the tumor.

	Previous	**1 h**	**2 h**	**24 h**
Heart	63	228	212	81
Liver	82	155	154	223
Kidney	46	99	97	76
Spleen	66	163	175	240
Inferior vena cava	61	263	234	96
Tumor	53	85	88	98

Table 3.1. HU values of the heart, liver, kidney, spleen, inferior vena cava, and tumor before and after the injection of the Fe_3O_4/TaO_x core/shell nanoparticles.

MRI, on the other hand, was able to capture the detailed structure of the tumor. Before intravenous injection of the nanoparticles, the tumor appeared homogeneous and bright in T_2-weighted MR images (Figure 3.10a). After administration of the nanoparticles, the tumor appeared inhomogeneous, though the overall signal of the tumor was significantly attenuated (Figure 3.10). The signal reduction in the peripheral region of the tumor was so severe that this region appeared very dark, whereas the tumor core became gray in the MR images. Histological observation of the dissected tumor slice revealed that the inhomogeneous tumor consisted of a peripheral oxygenated region and a hypoxic core region (Figure 3.11).[19] The cells in the peripheral region seemed to be healthy owing to sufficient oxygen and nutrients supplied by peripheral vasculatures. When the tumor slices were observed using fluorescence microscopy, the nanoparticles were found mainly in these peripheral regions around the blood vessels (Figure 3.12). Because of limited vasculature, delivery of antitumor agents to a hypoxic tumor core is known to be very difficult.[20] This is problematic, since the surviving cells in the inaccessible hypoxic region can be the source of tumor recurrence after therapy.[21] Because the hypoxic region and the oxygenated region can be distinguished using MRI, the

Fe$_3$O$_4$/TaO$_x$ core/shell nanoparticles can help to determine an effective method of tumor treatment. In addition, no adverse effect from the nanoparticles was observed in hematoxylin and eosin (H&E) stained sections of the major organs, including the liver, spleen, kidney, and heart; this indicates high biocompatibility (Figure 3.13). The Fe$_3$O$_4$/TaO$_x$ core/shell nanoparticles that were synthesized with an increased amount of the Fe$_3$O$_4$ nanoparticles failed to produce appropriate MR images because the signals of most internal organs were severely reduced (Figure 3.14).
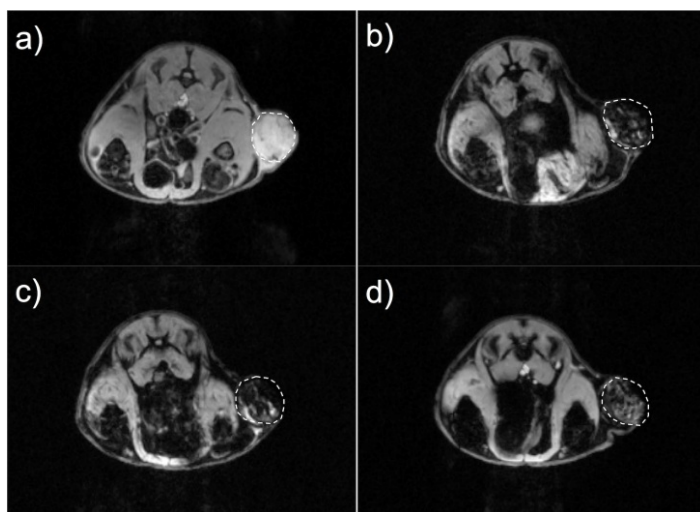
Figure 3.10. In vivo T_2-weighted MR image of the rat bearing MAT III
B tumor before (a) and 1 h (b), 2 h (c), and 24 h (d) after the injection
of Fe_3O_4/TaO_x core/shell nanoparticles (840 mg/kg).
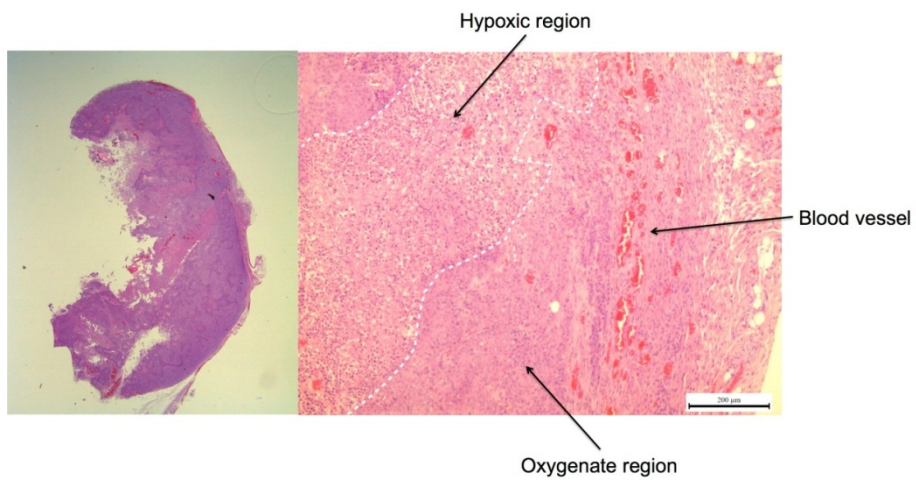
Figure 3.11. H&E stained section of the tumor. Whole-tumor image (left) shows that the interior is inhomogeneous. Magnified image (right) of tumor shows both hypoxic region and oxygenate region.

Red blood cells
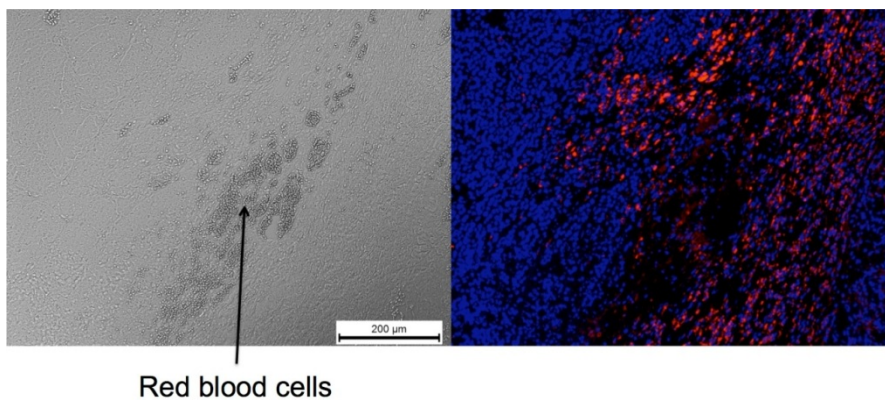
Figure 3.12. Bright field image (left) and fluorescence image (right) of the tumor. Red fluorescence around blood vessels represents Fe_3O_4/TaO_x core/shell nanoparticles.
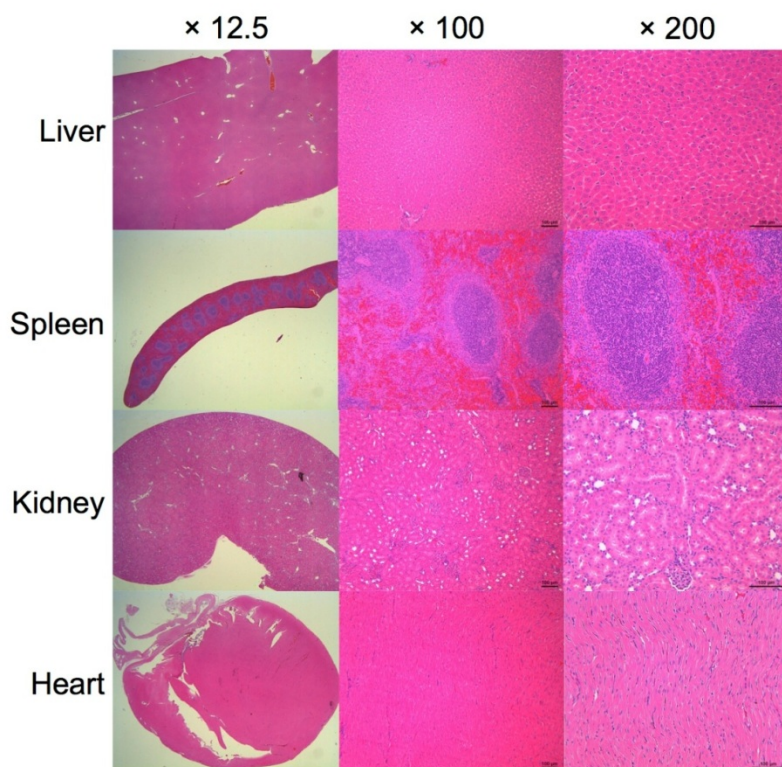
Figure 3.13. H&E stained sections of rat organs after intravenous administration of Fe_3O_4/TaO_x core/shell nanoparticles.
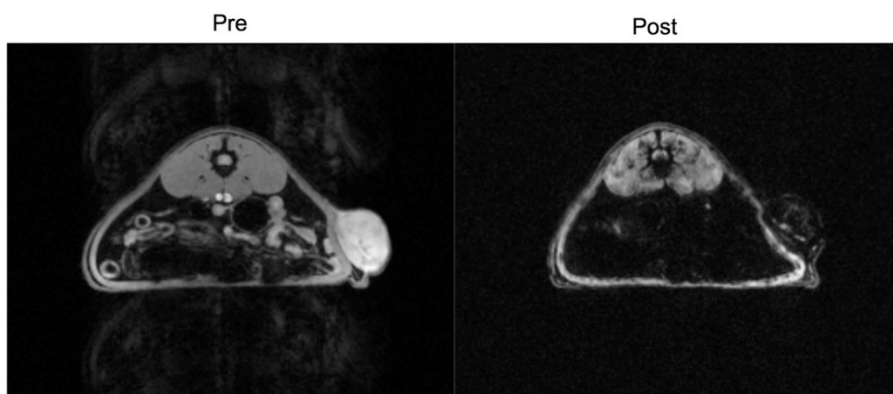
Figure 3.14. MR images of the rat before and after intravenous injection of the Fe_3O_4/TaO_x core/shell nanoparticles prepared at a concentration 0.4 mg/ml Fe_3O_4.

3.4 Conclusion

In conclusion, dual modal CT-MR imaging was successfully demonstrated using biocompatible Fe_3O_4/TaO_x core/shell nanoparticles. The multifunctional core/shell nanoparticles can provide complementary information of CT and MRI. Newly formed blood vessels to the tumors can be clearly imaged by CT, and the tumor microenvironment, including the hypoxic region and the oxygenated region can be evaluated using MRI. These core/shell nanoparticles have enormous potential for accurate cancer diagnosis through visualization of developed tumor vessels, monitoring of tumor status, and anticipation of therapy.

3.5 References

[1] (a) Klabunde, K. J., Ed. *Nanoscale Materials in Chemistry;* Wiley-Interscience: New York, 2001. (b) Ozin, G. A.; Arsenault, A.; Cademartiri, L. *Nanochemistry: A Chemical Approach to Nanomaterials Nanochemistry,* 2nd ed.; RSC Publishing: Cambridge, UK, 2008. (c) Schmid, G. *Nanoparticles: From Theory to Application;* Wiley-VCH: Weinheim, 2004. (d) Somorjai, G. A.; Frei, H.; Park, J. Y. *J. Am. Chem. Soc.* **2009**, *131*, 16589.

[2] (a) Niemeyer, C. M.; Mirkin, C. A. *Nanobiotechnology: Concepts, Applications and Perspectives;* Wiley-VCH: Weinheim, 2004. (b) Ho, D.; Sun, X.; Sun, S. *Acc. Chem. Res.* **2011**, *44*, 875. (c) Yoo, D.; Lee, J.-H.; Shin, T.-H.; Cheon, J. *Acc. Chem. Res.* **2011**, *44*, 863. (d) Bhirde, A.; Xie, J.; Swierczewska, M.; Chen, X. *Nanoscale* **2011**, *3*, 142. (e) Gao, J.; Xu, B. *Nano Today* **2009**, *4*, 37.

[3] (a) Gao, X.; Cui, Y.; Levenson, R. M.; Chung, L. W. K.; Nie, S. *Nat. Biotechnol.* **2004**, *22*, 969. (b) Perrault, S. D.; Walkey, C.; Jennings, T.; Fischer, H. C.; Chan, W. C. W. *Nano Lett.* **2009**, *9*, 1909.

[4] (a) Choi, H. S.; Liu, W.; Liu, F.; Nasr, K.; Misra, P.; Bawendi, M. G.; Frangioni, J. V. *Nat. Nanotechnol.* **2009**, *5*, 42. (b) Jun, Y.-w.; Lee, J.-H.; Cheon, J. *Angew. Chem. Int. Ed.* **2008**, *47*, 5122. (c) Rabin, O.; Perez, J.

M.; Grimm, J.; Wojtkiewicz, G.; Weissleder, R. *Nat. Mater.* **2006**, *5*, 118. (d) Kim, C.; Favazza, C.; Wang, L. V. *Chem. Rev.* **2010**, *110*, 2756. (e) Qian, X.; Peng, X.-H.; Ansari, D. O.; Yin-Goen, Q.; Chen, G. Z.; Shin, D. M.; Yang, L.; Young, A. N.; Wang, M. D.; Nie, S. *Nat. Biotechnol.* **2008**, *26*, 83.

[5] Willmann, J. K.; van Bruggen, N.; Dinkelborg, L. M.; Gambhir, S. S. *Nat. Rev. Drug. Discov.* **2008**, *7*, 591.

[6] Lee, N.; Kim, H.; Choi, S. H.; Park, M.; Kim, D.; Kim, H.-C.; Choi, Y.; Lin, S.; Kim, B. H.; Jung, H. S.; Kim, H.; Park, K. S.; Moon, W. K.; Hyeon, T. *Proc. Natl. Acad. Sci. U.S.A.* **2011**, *108*, 2662.

[7] Na, H. B.; Song, I. C.; Hyeon, T. *Adv. Mater.* **2009**, *21*, 2133.

[8] (a) Gao, J.; Gu, H.; Xu, B. *Acc. Chem. Res.* **2009**, *42*, 1097. (b) Kim, J.; Piao, Y.; Hyeon, T. *Chem. Soc. Rev.* **2009**, *38*, 372. (b) Lee, D.-E.; Koo, H.; Sun, I.-C.; Ryu, J. H.; Kim, K.; Kwon, I. C. *Chem. Soc. Rev.* DOI: 10.1039/c2cs15261d.

[9] (a) Lee, J. E.; Lee, N.; Kim, T.; Kim, J.; Hyeon, T. *Acc. Chem. Res.* **2011**, *44*, 893. (b) Selvan, S. T.; Patra, P. K.; Ang, C. Y.; Ying, J. Y. *Angew. Chem. Int. Ed.* **2007**, *46*, 2448. (c) So, M.-K.; Xu, C.; Loening, A. M.; Gambhir, S. S.; Rao, J. *Nat. Biotechnol.* **2006**, *24*, 339. (d) Choi, J.-s.; Park, J. C.; Nah, H.; Woo, S.; Oh, J.; Kim, K. M.; Cheon, G. J.; Chang,

Y.; Yoo, J.; Cheon, J. *Angew. Chem. Int. Ed.* **2008**, *47*, 6259. (e) Kim, D.; Yu, M. K.; Lee, T. S.; Park, J. J.; Jeong, Y. Y.; Jon, S. *Nanotechnology* **2011**, *22*, 155101.

[10] (a) Oh, M. H.; Lee, N.; Kim, H.; Park, S. P.; Piao, Y.; Lee, J.; Jun, S. W.; Moon, W. K.; Choi, S. H.; Hyeon, T. *J. Am. Chem. Soc.* **2011**, *133*, 5508. (b) Bonitatibus, Jr., P. J.; Torres, A. S.; Goddard, G. D.; FitzGerald, P. F.; Kulkarni, A. M. *Chem. Commun.* **2010**, *46*, 8956.

[11] (a) Kim, D.; Park, S.; Lee, J. H.; Jeong, Y. Y.; Jon, S. *J. Am. Chem. Soc.* **2007**, *129*, 7661. (b) Kinsella, J. M.; Jimenez, R. E.; Karmali, P. P.; Rush, A. M.; Kotamraju, V. R.; Gianneschi, N. C.; Ruoslahti, E.; Stupack, D.; Sailor, M. J. *Angew. Chem. Int. Ed.* **2011**, *50*, 12308. (c) Alric, C.; Taleb, J.; Le Duc, G.; Mandon, C.; Billotey, C.; Le Meur-Herland, A.; Brochard, T.; Vocanson, F.; Janier, M.; Perriat, P.; Roux, S.; Tillement, O. *J. Am. Chem. Soc.* **2008**, *130*, 5908. (d) Popovtzer, R.; Agrawal, A.; Kotov, N. A.; Popovtzer, A.; Balter, J.; Carey, T. E.; Kopelman, R. *Nano Lett.* **2008**, *8*, 4593. (e) Sun, I.-C.; Eun, D.-K.; Koo, H.; Ko, C.-Y.; Kim, H.-S.; Yi, D. K.; Choi, K.; Kwon, I. C.; Kim, K.; Ahn, C.-H. *Angew. Chem. Int. Ed.* **2011**, *50*, 9348.

[12] Park, J.; An, K.; Hwang, Y.; Park, J.-G.; Noh, H.-J.; Kim, J.-Y.; Park, J.-H.; Hwang, N.-M.; Hyeon, T. *Nat. Mater.* **2004**, *3*, 891.

[13] Pan, Y.; Neuss, S.; Leifert, A.; Fischler, M.; Wen, F.; Simon, U.; Schmid, G.; Brandau, W.; Jahnen-Dechent, W. *Small* **2007**, *3*, 1941.

[14] Chou, S.-W.; Shau, Y.-H.; Wu, P.-C.; Yang, Y.-S.; Shieh, D.-B.; Chen, C.-C. *J. Am. Chem. Soc.* **2010**, *132*, 13270.

[15] Gao, J.; Liang, G.; Zhang, B.; Kuang, Y.; Zhang, X.; Xu, B. *J. Am. Chem. Soc.* **2007**, *129*, 1428.

[16] Sieber, M. A.; Steger-Hartmann, T.; Lengsfeld, P.; Pietsch, H. *J. Magn. Reson. Imaging* **2009**, *30*, 1268.

[17] (a) Harisinghani, M. G.; Barentsz, J.; Hahn, P. F.; Deserno, W. M.; Tabatabaei, S.; van de Kaa, C. H.; de la Rosette, J.; Weissleder, R. N. Engl. J. Med. 2003, 348, 2491. (b) Chen, J. Y.; Leng, Y. X.; Tian, X. B.; Wang, L. P.; Huang, N.; Chu, P. K.; Yang, P. Biomaterials 2002, *23*, 2545.

[18] McDonald, D. M.; Choyke, P. L. *Nat. Med.* **2003**, *9*, 713.

[19] Harris, A. L. *Nat. Rev. Cancer* **2002**, *2*, 38.

[20] Primeau, A. J.; Rendon, A.; Hedley, D.; Lilge, L.; Tannock, I. F. *Clin. Cancer Res.* **2005**, *11*, 8782.

[21] Lewis, C.; Murdoch, C. *Am. J. Pathol.* **2005**, *167*, 627.

[22] Park, J.; An, K.; Hwang, Y.; Park, J.; Noh, H.; Kim, J.; Park, J.; Hwang, N.; Hyeon, T. *Nat. Mater.* **2004**, *3*, 891

Chapter 4. Galvanic Replacement Reactions in Metal Oxide Nanocrystals

4.1 Introduction

The chemical transformation of inorganic nanocrystals is a powerful tool for generating nanostructures with high structural and compositional complexities, and can thus be used to broaden the range of available nanostructured materials.[1-6] Among the various chemical transformation approaches, the galvanic replacement reaction is the most versatile method of preparing hollow metallic nanostructures with controllable pore structures and compositions.[7-12] These reactions involve a corrosion process that is driven by the difference in the electrochemical potentials of two metallic species. The hollow interior is generated from the oxidative dissolution of the metal nanocrystals that are used as reactive templates. Recent developments have enabled the production of highly complex, hollow nanostructures of metals and alloys.[12] However, the chemical transformation of ionic systems via galvanic reactions has remained elusive. Herein we demonstrate that a galvanic replacement reaction can occur in oxide nanocrystals as well,

and can produce hollow oxide nanostructures.

Hollow oxide nanocrystals have attracted a lot of interest owing to their potential for application in energy, medicine, and catalysis.[1,13] Even though considerable advances have been made in the synthesis of hollow nanocrystals of metallic oxides,[13-16] synthesizing hollow nanocrystals of multimetallic oxides still remains a challenge. In this study, we show that by using a nanoscale galvanic replacement reaction, monometallic oxide nanocrystals can be completely transformed into hollow multimetallic oxide nanostructures. Contrary to what is observed in the case of metallic systems, it was noticed that a redox-couple reaction between multivalent metallic ions took place during the process. The metal ions in the nanocrystals were replaced by the ions of another metal in the solution. We chose nanocrystalline manganese oxide (Mn_3O_4) as the starting material to show that hollow heterostructured nanocrystals of manganese oxide/iron oxide (Mn_3O_4/γ-Fe_2O_3) with a box-like shape ("nanoboxes") could be synthesized, and eventually transformed into cage-shaped iron oxide (γ-Fe_2O_3) nanocrystals ("nanocages").

We also demonstrate that these unique oxide nanostructures with a hollow structure and multimetallic composition exhibit synergistic

properties that make them attractive for anodes in lithium ion batteries (LIBs). Our results not only uncover a previously unknown pathway for the formation of hollow nanocrystals of multimetallic oxides, but also advance the understanding of the galvanic processes in nanocrystal transformations.

4.2 Experimental Section

4.2.1. Synthesis of Mn_3O_4 and Co_3O_4 nanocrystals

For synthesizing the Mn_3O_4 nanocrystals, 0.17 g of manganese(II) acetate (Aldrich), 0.67 g of oleylamine (Acros), and 0.14 g of oleic acid (Aldrich) were dissolved in 15 mL of xylene placed in a three-necked 50 mL flask that was equipped with a reflux condenser and a Teflon-coated magnetic stirring bar and slowly heated to 90 °C in air under magnetic stirring. 1 mL of deionized water was then rapidly injected into the flask using a pipette. The reaction mixture was further heated at 90 °C in air for 1.5 h.

For synthesizing the Co_3O_4 nanocrystals, 1 mmol of cobalt(II) perchlorate (Aldrich) was dissolved in 15 mL of octanol in a 100 mL flask equipped with a reflux condenser and sonicated for 10 min . 10 mmol of oleylamine and 1 mL of water were sequentially added into the flask at 60 °C in air under magnetic stirring. The reaction mixture was further heated at 160 °C in air for 6 h.

4.2.2. Galvanic replacement reactions

A typical procedure for the preparation of nanoboxes and nanocages

was as follows: 16 mL of the as-prepared suspension of the Mn_3O_4 was added to a three-necked 50 mL flask and the mixture was heated to 90 °C in air under magnetic stirring. Different samples of Mn_3O_4/γ-Fe_2O_3 and γ-Fe_2O_3 were prepared by adding either 1 mL of aqueous solutions of iron(II) perchlorate (Aldrich) of various concentrations (0.1–2.0 M) to the flasks by pipette.

Mn_3O_4/SnO_2 nanocages were prepared by adding 1.34 g of oleylamine and 0.5 mL of aqueous solutions of Sn(II) chloride of 2.0 M concentration, prepared with 0.4 ml of HCl solution (37%), to the suspension of Mn_3O_4 nanocrystals.

SnO_2 nanocages, using Mn_3O_4 nanocrystals as reactive template, were prepared by adding 0.67 g of oleylamine, 0.14 g of oleic acid, 0.2 mL of HCl, and 0.5 mL of the aqueous solutions of Sn(II) chloride, to the suspension of Mn_3O_4 nanocrystals.

Co_3O_4/SnO_2 nanocages were prepared by adding 1 mL of the aqueous solution of Sn(II) chloride of 2.0 M concentration, prepared with 0.6 ml of HCl solution (37%), to the suspension composed of 1 mmol of the Co_3O_4 nanocrystals, 2 g of oleylamine, 0.14 g of oleic acid, and 15 mL of xylene.

SnO_2 nanocages, using Co_3O_4 nanocrystals, were prepared by adding

1 mL of the aqueous solution of Sn(II) chloride of 2.0 M concentration, prepared with 0.4 ml of HCl solution (37%), to the suspension composed of 1 mmol of the Co_3O_4 nanocrystals, 0.67 g of oleylamine, 0.14 g of oleic acid, and 15 mL of xylene.

In the case of each sample, the reaction mixture was heated at 90 °C in air for 2 h and then cooled down to room temperature. The reaction product was then collected by centrifugation and washed several times with ethanol before being characterized.

4.2.3. Structural analysis

The transmission electron microscopy (TEM) images were captured using a JEOL EM-2010 transmission electron microscope, which was operated at 200 kV. The high-resolution TEM (HRTEM) was performed on a JEOL 2200FS transmission electron microscope at the University of Aveiro, Portugal, which was operated at 200 kV. The energy-filtered TEM images were recorded with a Tecnai F20 transmission electron microscope. Elemental analysis was performed via inductively coupled plasma-atomic emission spectroscopy (ICP-AES) (Shimadzu). X-ray diffraction patterns were obtained using a Rigaku D/max 2500 diffractometer equipped with a rotating anode and

a Cu Kα radiation source (λ = 0.15418 nm). Magnetization measurements were performed on a MPMS 5XL Quantum Design SQUID magnetometer. The Fe and Mn $L_{2,3}$-edge X-ray absorption spectroscopies (XAS) and the X-ray magnetic circular dichroism (XMCD) measurements were carried out at Beamline 2A at the Pohang Light Source at the Pohang Accelerator Laboratory. The nitrogen adsorption and desorption isotherms were measured at 77 K using a Micromeritics ASAP 2000 gas adsorption analyzer. The total surface area and pore volume was determined using the Brunauer-Emmett-Teller (BET) equation and the single-point method, respectively.

4.2.4. Electrochemical measurements

A typical procedure for the preparation of the samples for the electrochemical measurements was as follows: 0.5 ml of pyrrole (Aldrich) was added to 170 mL of the as-prepared suspension of the nanocrystals and the mixture heated to 60 °C in order to polymerize pyrrole on the surface of the nanocrystals. After being aged for a period of 6 h at the same temperature, the polypyrrole-coated nanocrystals were separated by centrifugation and washed with ethanol three times. In order to facilitate the carbonization of the layer of polypyrrole on the

surface of nanocrystals, the samples were heated at 500 °C for 2 h in an argon atmosphere. Then, the resulting powder was used as the active material for a working electrode. In order to prepare the working electrodes, the active material, conductive carbon black (Super P), and poly(vinylidene fluoride) were mixed in the weight ratio of 70:15:15 in the solvent N-methyl-2-pyrrolidone. This mixture was then coated on a piece of copper foil. After forming the working electrodes by drying this mixture at 120 °C for 8 h, coin-type half cells were assembled in an Ar-filled glove box.

The electrochemical measurements were carried out using the coin-type half cells with a WBCS3000 cycler (WonAtech) at room temperature. Two electrodes composed of Li foil were used as the counter and reference electrodes. Polyethylene film (Celgard 2300) was used as the separator, and 1.0 M LiPF6 dissolved in a 1:1 volume mixture of ethylene carbonate and diethyl carbonate was used as the electrolyte. The cells were charged and discharged for 50 cycles at a constant current density of 100 mA·g^{-1} and with the voltage ranging from 0.1 to 3.0 V (vs. Li+/Li).

4.3 Result and Discussion

4.3.1 Synthesis and characterizartion of Mn_3O_4/γ-Fe_2O_3 and γ-Fe_2O_3 nanoboxes and nanocages

Mn_3O_4 nanocrystals were prepared by slightly modifying a previously reported method.[17,18] Transmission electron microscopy (TEM) images of the as-prepared Mn_3O_4 nanocrystals showed that they were tetragonal shaped with sides of ~ 20 nm and a height of ~ 10 nm (Figures 4.1a, 4.1b).[18] A high-resolution TEM (HRTEM) image and the corresponding Fourier-transform (FT) pattern of the Mn_3O_4 nanocrystals revealed that the top and side surface of the nanocrystals were enclosed by {001} and {100} facets, respectively, and their corners and edges were slightly truncated.

The galvanic replacement reaction was initiated by adding an aqueous solution of iron(II) perchlorate into a suspension of the Mn_3O_4 nanocrystals in xylene and subsequently heating the reaction mixture at 90 °C for 1.5 h.[18] Figures 4.1c and 4.1d show the TEM and HRTEM images of the product derived from the galvanic replacement reaction between the Mn_3O_4 nanocrystals and 1 mL of 2.0 M aqueous solution of iron(II) perchlorate. The images show that the original nanocrystals

transformed completely into nanocages having a hollow interior and holes on their shell. The exterior shape of the nanocages was nearly the same as that of the original Mn_3O_4 nanocrystals. In addition, as can be noticed from the HRTEM image in Figure 4.1d, the shell of these nanocages had a single-crystalline structure with highly ordered continuous lattice fringes. Using inductively coupled plasma-atomic emission spectrometry (ICP-AES), the molar ratio of iron to manganese in the nanocages was found to be 91:9 (Figure 4.2a), showing that the manganese ions in the original nanocrystals were almost completely replaced by iron ions. It is known that the surface precipitation of iron oxide reduces the dissolution rate of manganese oxide by preventing the diffusion of ions/electrons to the surface of manganese oxide. [19] However, if the volume of manganese oxide is below a certain critical limit, its complete dissolution and thus the near-total replacement of manganese by iron could be achieved. Indeed, the ICP-AES results showed that the Mn molar ratio decreased to less than 0.1% when the Mn_3O_4 nanocrystals were treated with more concentrated 3.0 M iron(II) perchlorate solution. To further confirm whether the volume of manganese oxide had an effect on the transformation, the same reaction was performed using bulk Mn_3O_4 powder. It was observed that the

molar fraction of Fe in the thus-formed product was significantly lower (less than 25%) (Figure 4.2a). Powder X-ray diffraction (XRD) patterns of the reactant and the products, shown in Figure 4.2b, confirmed that the tetragonally distorted Mn_3O_4 spinel transformed into a cubic γ-Fe_2O_3 spinel as the concentration of the iron(II) perchlorate solution was increased. This observation was also supported by saturation magnetization curves obtained by a superconducting quantum interface device (SQUID) measurement, which showed that magnetization of the nanocrystals increased steadily with an increase in the Fe content (Figure 4.2c). Furthermore, we could also synthesize hollow nanocages of Mn_3O_4/SnO_2, Co_3O_4/SnO_2, and SnO_2 from the reactions of Mn_3O_4 and Co_3O_4 nanocrystals with aqueous Sn(II) chloride solutions (Figure 4.3a, 4.3b and Figure 4.4), demonstrating the generality of the transformation process.
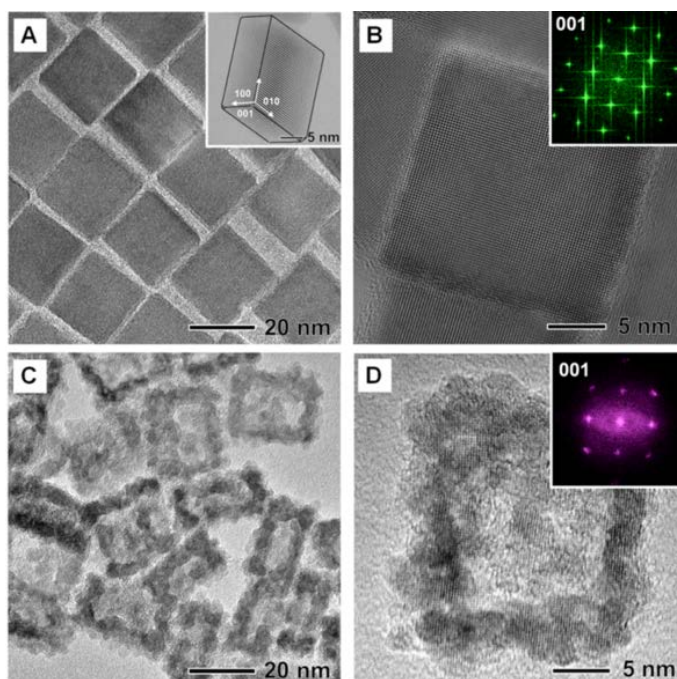
Figure 4.1. (a) TEM image of Mn_3O_4 nanocrystals synthesized by the reaction of manganese(II) acetate with water in the presence of oleylamine and oleic acid in a xylene solution. Inset shows the corresponding HRTEM image of a single nanocrystal recorded along the [111] axis. (b) HRTEM images of a single Mn_3O_4 nanocrystal recorded along the [001] axis, respectively. The inset shows the corresponding FT patterns. (c) TEM and (d) HRTEM images of the γ-Fe_2O_3 nanocages synthesized by reacting the Mn_3O_4 nanocrystals with 1 mL of 2.0 M aqueous iron(II) perchlorate solution.
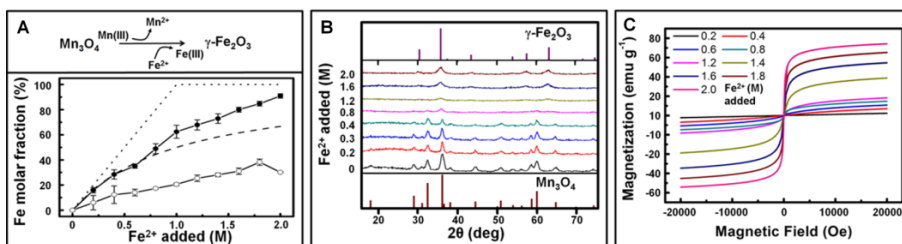
Figure 4.2. (a) ICP-AES data showing the molar fraction of Fe in the reaction product as a function of the amount of Fe(II) perchlorate added during the synthesis using the Mn_3O_4 nanocrystals (solid circle) and their bulk counterpart (open circle). The molar fractions expected in the cases of the complete replacement of Mn by Fe (dotted line) and the addition of Fe to Mn (dashed line) are also shown. (b) Powder XRD patterns of the original Mn_3O_4 nanocrystals and the $Mn_3O_4/\gamma\text{-}Fe_2O_3$ and $\gamma\text{-}Fe_2O_3$ nanocages. For comparison, the known XRD patterns of Mn_3O_4 and $\gamma\text{-}Fe_2O_3$ are also shown above and below the experimentally determined patterns, respectively. (c) Saturation magnetization curves obtained by the SQUID measurement.
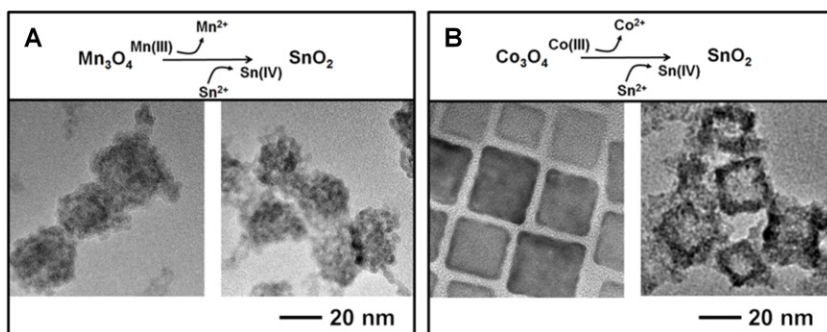
Figure 4.3. (a) TEM images of Mn_3O_4/SnO_2 nanocages (left) and SnO_2 nanocages (right) produced by reacting the Mn_3O_4 nanocrystals with 0.5 mL of 2.0 M aqueous Sn(II) chloride solutions in similar synthetic solutions. (b) TEM images of the Co_3O_4 nanocrystals (left) synthesized by the reaction of cobalt(II) perchlorate with water in the presence of oleylamine in an octanol solution, and SnO_2 nanocages (right) produced by reacting the Co_3O_4 nanocrystals with 1 mL of 2.0 M aqueous Sn(II) chloride solution.
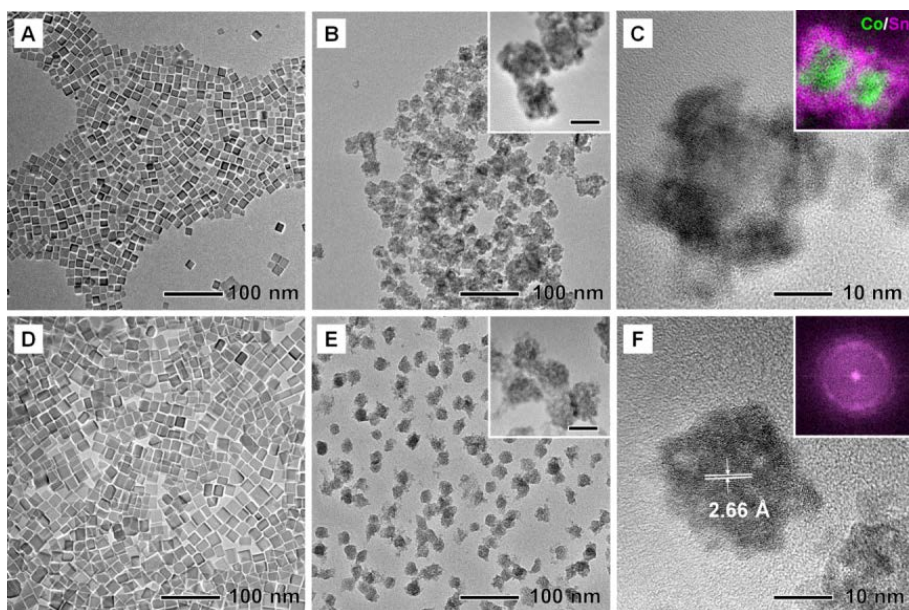
Figure 4.4. (a) TEM image of the Co_3O_4 nanocrystals synthesized by reaction of 1 mmol of cobalt(II) perchlorate with water in the presence of oleylamine in an octanol solution. (b) TEM image of the Co_3O_4/SnO_2 nanocages synthesized by the reaction of the Co_3O_4 nanocrystals with 1 mL of a 2.0 M aqueous Sn(II) chloride solution. The inset shows their corresponding high-magnification TEM image. Scale bar, 10 nm. (c) HRTEM image of a single Co_3O_4/SnO_2 nanocage. The inset shows an EFTEM image of the nanocages. (d) Mn_3O_4 nanocrystals synthesized by the reaction of 1 mmol of manganese(II) acetate with water in the presence of oleylamine and oleic acid in a

xylene solution. (e) TEM image of SnO_2 nanocages produced by the reaction of the Mn_3O_4 nanocrystals with 0.5 mL of 2.0 M aqueous Sn(II) chloride solution. The inset shows their corresponding high-magnification TEM image. Scale bar, 10 nm. (f) HRTEM image of a single SnO_2 nanocage. The inset shows the corresponding FT pattern.

4.3.2 Morphological evolution of the nanocage

The evolution of the internal hollow core was examined by reacting the Mn_3O_4 nanocrystals with aqueous iron(II) perchlorate solutions of various concentrations (Figure 4.5 and Figure 4.6). When a less concentrated solution was used, the cores of the Mn_3O_4 nanocrystals dissolved partially and nanoboxes with relatively thick walls were formed (Figures 4.5b,f and 4.5c,g). The HRTEM images displayed in Figures 4.5b and 4.5c show clearly that pinholes were formed on the surface of the nanoboxes.[18] These observations indicate that pores develop inside the nanocrystals by a mechanism analogous to pinhole corrosion, where pinholes serve as transport paths during the dissolution of the nanocrystal core. As the concentration was increased to 1.0 M, the pores increased further in size, and the nanoboxes evolved into nanocages with clear openings (Figure 4.5d,h). During the intermediate stages of the replacement reaction, both the nanoboxes and the nanocages exhibited continuous fringe patterns, indicating that the lattice orientations of the original Mn_3O_4 nanocrystals were preserved throughout the process. Figures 4.5b-e and their corresponding insets show that there was a slight increase in the interplanar distance between the (100) plane of the Mn_3O_4 crystals and

the (110) plane of the γ-Fe_2O_3 crystals. This change, however, did not alter the alignments of the lattices along the square basal planes of the nanocrystals. The preservation of the lattice alignments was suggestive of a topotactic transformation. The color-mapped energy-filtered TEM (EFTEM) image in Figure 4.5g shows the accumulation of Fe species in the shell region of the nanocages, whereas the image in Figure 4.5i shows the homogeneous deposition of the Fe species over the entire surface of the nanocages.
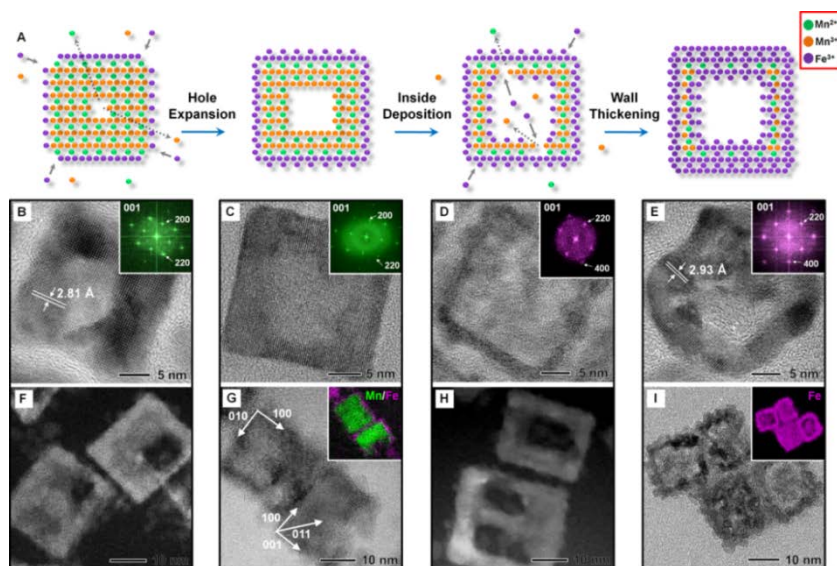
Figure 4.5. (a) Schematic illustration of the transformation of the Mn$_3$O$_4$ nanocrystals, showing evolution of their morphology via the localized dissolution of Mn$_3$O$_4$ and the surface precipitation of γ-Fe$_2$O$_3$. (b)–(e) HRTEM images of the hollow nanostructures synthesized by the reaction of the Mn$_3$O$_4$ nanocrystals with 1 mL of aqueous solutions of iron(II) perchlorate having different concentrations: (b) 0.4 M, (c) 0.6 M, (d) 1.0 M, and (e) 1.6 M. Insets show the corresponding FT patterns. (f) High-angle annular dark-field scanning TEM image of the nanoboxes shown in (B). (g) TEM image and a corresponding EFTEM image of the nanoboxes shown in (c). (h) High-angle annular dark-field scanning TEM image of the nanoboxes shown in (c). (i) TEM image and a corresponding EFTEM image of the nanocages shown in (e).
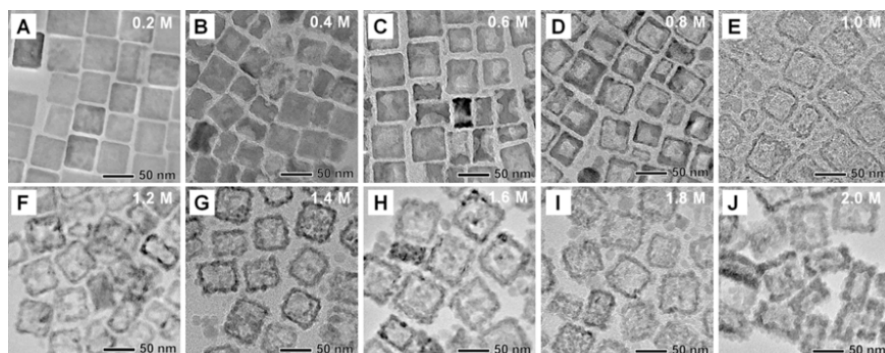
Figure 4.6. TEM overview images of the nanoboxes and nanocages synthesized by the reaction of the Mn_3O_4 nanocrystals with 1 mL of aqueous solutions of iron(II) perchlorate having different concentrations: (a) 0.2 M, (b) 0.4 M, (c) 0.6 M, (d) 0.8 M, (e) 1.0 M, (f) 1.2 M, (g) 1.4 M, (h) 1.6 M, (i) 1.8 M, and (j) 2.0 M.

4.3.3 X-ray absorption analysis for demonstration of galvanic replacement reaction

We performed X-ray absorption spectroscopy (XAS) and X-ray magnetic circular dichroism (XMCD) measurements at Beamline 2A of the Pohang Light Source to figure out the valence states of the transition-metal cations.[18] Figure 4.7a illustrates the evolution of the X-ray absorption spectra at the Mn $L_{2,3}$-edge with an increase in the molar ratio of iron to manganese. The Mn $L_{2,3}$-edge X-ray absorption spectra of the nanoboxes, shown in Figure 4.7a, are almost identical to that of the original Mn_3O_4 nanocrystals where both Mn^{3+} and Mn^{2+} ions were present and occupied octahedral and tetrahedral sites in the spinel structure, respectively. As can be seen in the X-ray absorption spectra **b–d** in Figure 4.7a, the peak corresponding to the Mn^{3+} ions gradually disappeared, and only the peaks of Mn^{2+} ions remained after the completion of the replacement reaction.[20] However, the decrease in the molar concentration of the Mn^{2+} ions to less than 9% (cf. ICP-AES data) suggested that most of the Mn^{2+} ions were also removed from the tetrahedral sites. Both the X-ray absorption and the XMCD spectra at the Fe $L_{2,3}$ edges of the nanocages were similar to those of γ-Fe_2O_3 (maghemite) that contains only Fe^{3+} ions, but not to those of Fe_3O_4

(magnetite) that contains both Fe^{3+} and Fe^{2+} ions (Figures 4.7b and 4.7c). These results suggested that Fe^{3+} ions were introduced at the octahedral sites of the spinel structure that were previously occupied by Mn^{3+} ions.
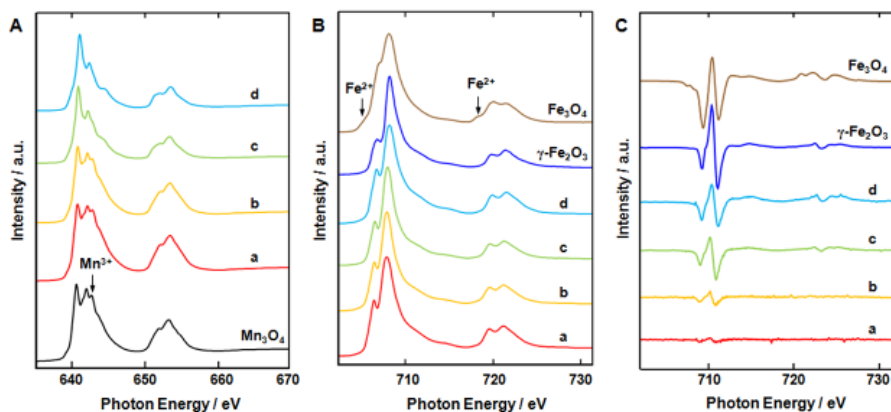
Figure 4.7. Results of the XAS and XMCD characterization of the hollow nanostructures synthesized by the reaction of the Mn_3O_4 nanocrystals with 1 mL of aqueous solutions of iron(II) perchlorate having different concentrations: **a** 0.4 M, **b** 0.8 M, **c** 1.6 M, and **d** 2.0 M. (a) X-ray absorption spectra at the Mn $L_{2,3}$-edges of the original Mn_3O_4 nanocrystals and the hollow nanostructures. (b) X-ray absorption spectra at the Fe $L_{2,3}$-edge and (c) the XMCD spectra of the hollow nanostructures compared with those of the bulk materials, γ-Fe_2O_3 and Fe_3O_4, for reference.

4.3.1 Mechanism in the galvanic replacement reaction

The galvanic reaction employed in this study could be explained on the basis of the difference in the standard reduction potentials of the Fe^{3+}/Fe^{2+} and Mn_3O_4/Mn^{2+} pairs. Since the standard reduction potential of the Fe^{3+}/Fe^{2+} pair (0.77 V relative to the standard hydrogen electrode (SHE)) is less than that of the Mn_3O_4/Mn^{2+} pair (1.82 V relative to the SHE),[21] Fe^{2+} is oxidized to Fe^{3+} while Mn_3O_4 is simultaneously reduced to Mn^{2+}. We also performed similar experiments using $FeCl_2$ or $FeCl_3$ in place of iron(II) perchlorate. The structural transformation of the Mn_3O_4 nanocrystals into hollow nanocages was observed when the nanocrystals were reacted with $FeCl_2$, but not when they were reacted with $FeCl_3$ (Figure 4.8).[18] These observations support our hypothesis that the Fe^{2+} ions serve as reducing agents for the selective reduction of the Mn^{3+} ions in the Mn_3O_4 nanocrystals. The oxidation of Fe^{2+} releases an electron, which, in turn, reduces Mn^{3+} to Mn^{2+}, thus giving rise to positive charge deficiencies at the octahedral sites in the Mn_3O_4 nanocrystals. These deficiencies are compensated by the substitution of the Mn^{2+} ions with Fe^{3+} ions. When the galvanic reaction is initiated, the reduced Mn^{2+} ions dissolve, leaving behind empty octahedral sites near the surface of the nanocrystals. At the same time, some of the

155

oxidized Fe^{3+} ions present in the solution diffuse to the surface of the nanocrystals and fill the readily accessible vacancies. The outward flow of the reduced Mn^{2+} ions and the accompanying topotactic precipitation of the oxidized Fe^{3+} ions from the solution to the surface of the Mn_3O_4 nanocrystals transform Mn_3O_4 into γ-Fe_2O_3, starting with the outermost shell of the nanocrystals. This prevents the outward diffusion of the underlying Mn^{2+} species. It was noticed that this transformation occurred preferentially around the edges of the shell (inset of Figure 4.5g). An increase in the number of empty octahedral sites owing to significant dissolution of the reduced Mn^{2+} ions can lead to the complete disruption of the remaining lattice that consists of tetrahedral Mn^{2+} ions and oxygen anions.[22,23] This process led to the formation of pinholes during the initial stage of reaction in the areas not covered by γ-Fe_2O_3 layer, i.e., in the middle of the basal plane. As the reaction progresses, the electrons released from the Fe^{2+} ions migrate inward and reduce the octahedral Mn^{3+} ions in the interior of the Mn_3O_4 nanocrystals. The pinholes formed during the initial stage of the reaction act as pathways for the continued transportation of the reduced Mn^{2+} ions out of the formed nanoboxes, thus facilitating the dissolution of the residual core species, i.e., the tetrahedral Mn^{2+} ions and oxygen

anions. The reaction continues until the core has been emptied and the side walls have been hollowed, resulting in the formation of heterostructured Mn_3O_4/Fe_2O_3 nanocages. At this stage, owing to the open structure of the nascent γ-Fe_2O_3 nanocages, precipitation of γ-Fe_2O_3 occurs in their hollow interior, leading to the further transformation of the γ-Fe_2O_3 nanocages. It was noticed that the perchlorate moiety in the aqueous iron(II) perchlorate solution did not contribute to the formation of the hollow structure because no morphological change was observed when the Mn_3O_4 nanocrystals were reacted with perchloric acid (Figure 4.9).[18] In addition, we found that cage-like structures with a different morphology could also be produced via the same method by using different-shaped Mn_3O_4 nanocrystals as the starting material (Figure 4.10).[18]
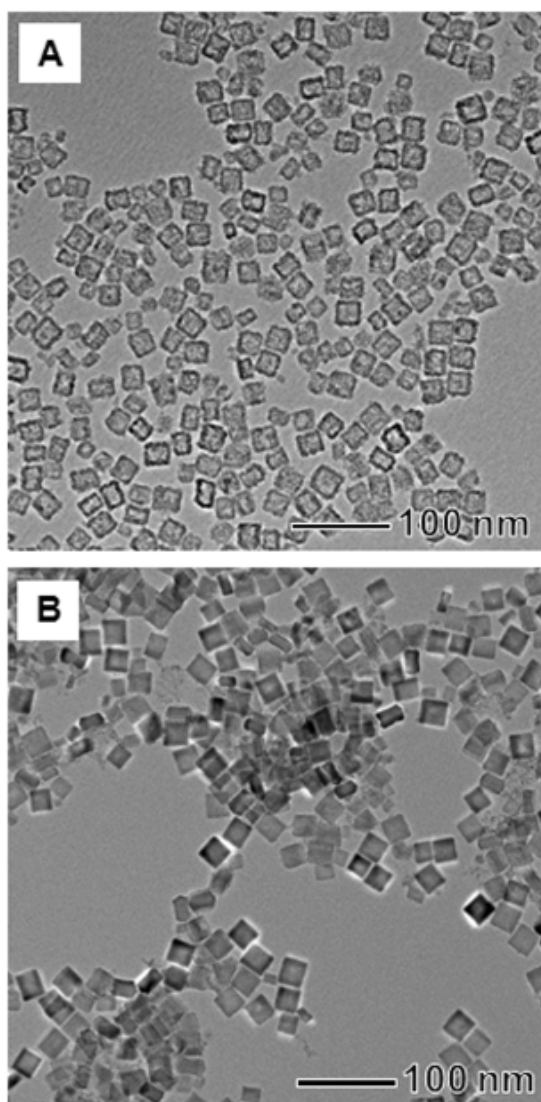
Figure 4.8. TEM images of the samples prepared under the same conditions as those shown in Figure 4.1d. However, for the samples shown in these images, the Mn_3O_4 nanocrystals were reacted with (a) $FeCl_2$ and (b) $FeCl_3$ instead of iron(II) perchlorate.
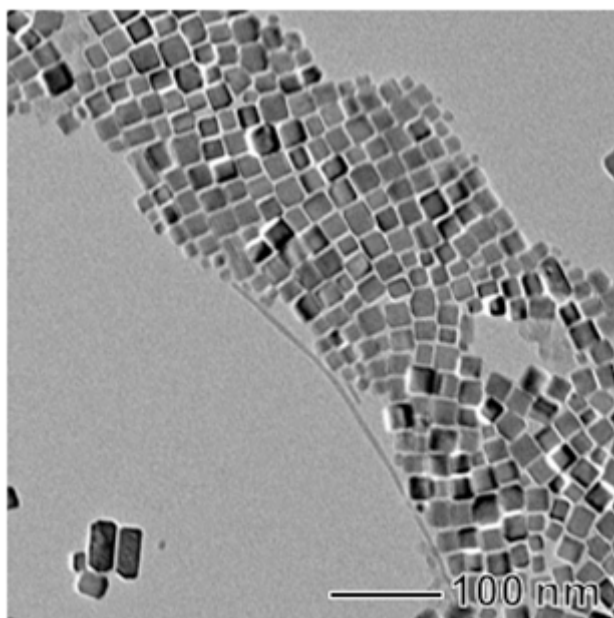
Figure 4.9. TEM image of a sample prepared under the same conditions as those shown in Figure 4.1d. However, for the sample shown in this image, the Mn_3O_4 nanocrystals were reacted with perchloric acid instead of iron(II) perchlorate.
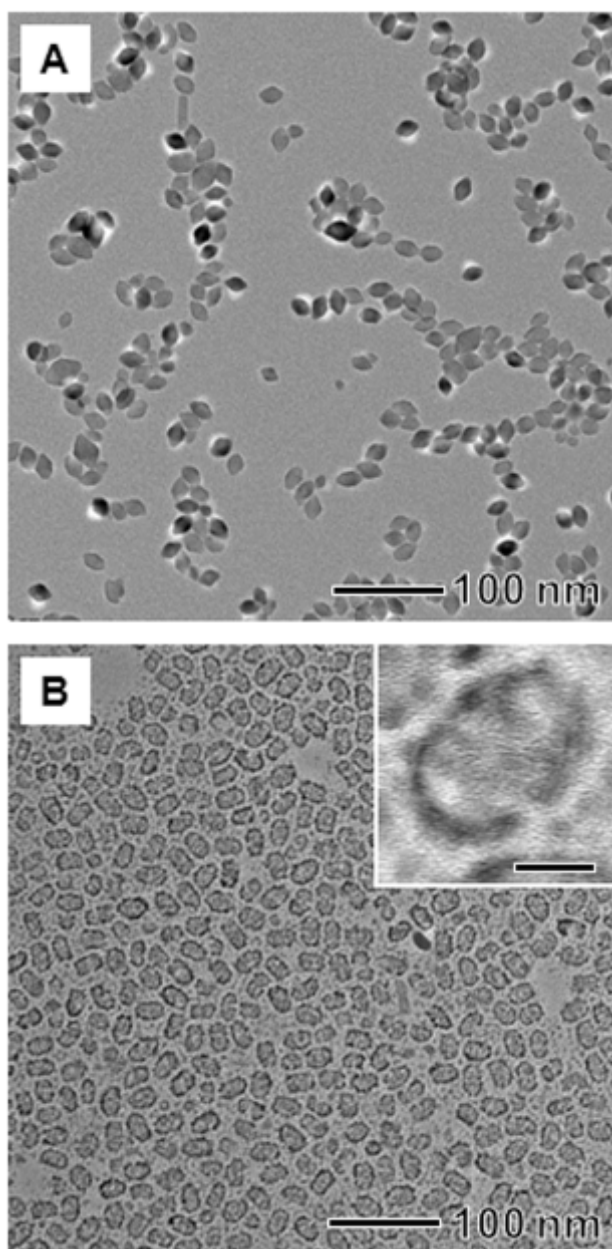
Figure 4.10. (a) TEM image of ellipsoidal Mn_3O_4 nanocrystals synthesized by the reaction of manganese(II) acetate with water in the

160

presence of oleylamine (0.41 g) and oleic acid (0.43 g) in a xylene solution. (b) TEM image of the nanocages synthesized by the reaction of the ellipsoidal Mn_3O_4 nanocrystals with 1 mL of a 2.0 M aqueous iron(II) perchlorate solution. The inset shows an HRTEM image of a single nanocage. Scale bar, 10 nm.

4.3.1 Lithium ion bettery application of nanoboxes and nanocages

Transition-metal oxides such as Mn_3O_4 and Fe_3O_4 are attractive anode materials for lithium ion batteries (LIBs) owing to their higher specific capacities compared to typical graphitic anodes. However, their capacities decrease drastically with cycling because of their severe volume changes during Li insertion/extraction and their consequent aggregation/pulverization.[24-26] Despite its theoretically high capacity (936 mAh·g^{-1}), Mn_3O_4 usually exhibits a much lower capacity ($\leq$ ~400 mAh·g^{-1}) because of its low electrical conductivity (~10^{-7}–10^{-8} S/cm).[25] The current galvanic replacement reactions in oxide nanocrystals can be a promising technique for engineering their structures and tuning their chemical compositions to improve their electrochemical properties for their applications to LIB anodes. A number of different samples, labeled as MF#, were prepared by varying the molar concentration (#) of iron(II) perchlorate. The test samples of MF0.6, MF0.8, MF1.0, and MF1.6 were coated with polypyrrole in situ in the reaction solution and carbonized at 500°C for 2 h in an Ar atmosphere.[18] As a result of this thermal treatment, the nanocrystals transformed into a solid solution of Mn_3O_4 and Fe_3O_4, while retaining their original shapes (Figure 4.11b and Figure 4.12). XRD patterns

revealed a cubic ferrite structure, which suggested that $Mn_{3-x}Fe_xO_4$ was gradually changed from $MnFe_2O_4$ to Fe_3O_4 as the Fe content increased (Figure 4.11a).

Two plateaus were observed around 0.55 and 0.68 V in the first discharge curve of the MF0.6 sample with a peak ratio of 2:1, as shown in the inset of Figure 4.11c. The MF0.8 and MF1.0 samples exhibited two plateaus at slightly higher voltages of around 0.59 and 0.73 V. The ratio of the plateau at the upper potential gradually increased with the Fe content of the sample. For the MF1.6 sample, the plateau around 0.60 V eventually disappeared and the upper-potential plateau shifted to 0.83 V, a value similar to that of commercially available Fe_3O_4 (Figure 4.11c), indicating that almost all Mn ions were replaced by Fe ions. The changes in the ratios and potentials of the two plateaus seem to be related to the content of substituted Fe in Mn_3O_4.

The potential of $Mn_{3-x}Fe_xO_4$ as a function of the Fe content was investigated through *ab initio* density functional theory calculations (see the computational part in the Supplementary Materials for details). The results of the *ab initio* calculations suggested that the solid solution of $Mn_{3-x}Fe_xO_4$ can occur between Mn_3O_4 and Fe_3O_4 (Figure 4.16) and their average voltages are proportional to the amount of the Fe_3O_4

component from 0.400 to 0.818 V at $0 \leq x \leq 3$ (table 4.2). In the initial stage of galvanic replacement reaction, the outer shell of the nanocrystals becomes Fe-rich phase of $Mn_{1-x}Fe_{2+x}O_4$. Thus, the plateau of the upper potential appears in the discharge curve of MF0.6 sample. However, the potential at this plateau was lower than that of Fe_3O_4, since overall concentration of Mn in MF0.6 sample was still high. As the galvanic replacement reaction progressed, the Fe-rich phase expanded inside the nanocrystals and the overall Fe concentration increased. Thus, the plateau of the upper potential became wider, and its value gradually increased to that of Fe_3O_4. On the other hand, the Mn-rich phase of $Mn_{1+x}Fe_{2-x}O_4$ in the inner shell of the nanocrystals exhibited a lower reduction potential than that of $MnFe_2O_4$. As the Fe concentration increased, more Fe ions diffused into the Mn-rich phase of $Mn_{1+x}Fe_{2-x}O_4$ during the thermal treatment, resulting in a slight increase in its potential. The Mn-rich phase gradually transformed into Fe_3O_4, and the plateau around 0.60 V eventually disappeared. These results show that the potentials of multicomponent spinel electrode materials can be easily tuned by a galvanic replacement reaction.

Figure 4.11d shows the cycling performance of MF0.6, MF0.8, MF1.0, and MF1.6 samples and commercially available Fe_3O_4

164

nanoparticles at a current density of 100 mA·g^{-1} with the voltage ranging from 3.0 to 0.01 V. The MF1.0 sample exhibited first discharge and charge capacities of 1339 and 984 mA·h·g^{-1}, respectively. The reversible capacities of MF0.6, MF0.8, and MF1.6 samples were comparable to those of MF1.0 sample. In addition, most of the samples showed markedly better capacity retention than that of similar-sized commercial Fe_3O_4 nanoparticles. For example, MF1.0 sample exhibited a high reversible capacity of ~1000 mAh/g with almost no fading up to 100 cycles. The good capacity retention of both the nanoboxes and the nanocages can be attributed to their hollow structure, which provides extra free space for alleviating the structural strain caused by the large volume change.[26] In addition, MF1.0 sample exhibited the highest rate capability (Figure 4.15), which is due to the improvement in its electronic conductivity resulting from the mixed valency of the multicomponent $Mn_{3-x}Fe_xO_4$ spinel structure,[27] which is similar to the improvement of electronic conductivity of $Li_4Ti_5O_{12}$ by ion doping.[28]
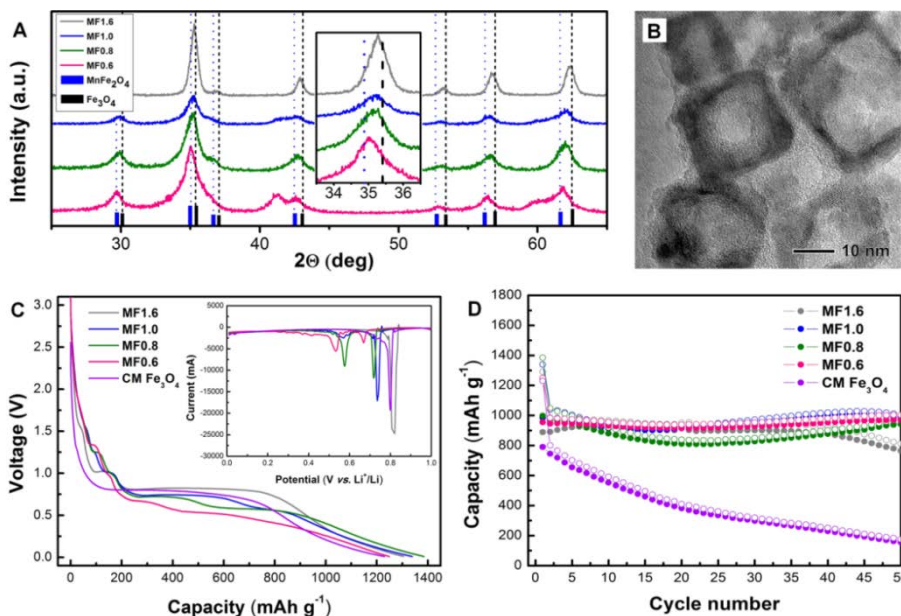
Figure 4.11. Carbon-coated nanoboxes and nanocages synthesized using iron(II) perchlorate solutions of different concentrations (MF0.6, MF0.8, MF1.0, and MF1.6). (a) XRD patterns showing that the crystal structures of these samples gradually changed from $MnFe_2O_4$ to Fe_3O_4 with an increase in the concentration of the Fe(II) perchlorate solution used. (b) TEM image of the carbon-coated MF1.0. (c and d) Electrochemical measurements of the samples and commercial Fe_3O_4 nanoparticles showing (c) first discharge curves and corresponding results of the dQ/dV analysis and (d) cycling performance, recorded at a current density of 100 mA·g^{-1} with the voltage in the range of 3.0 and 0.01 V.
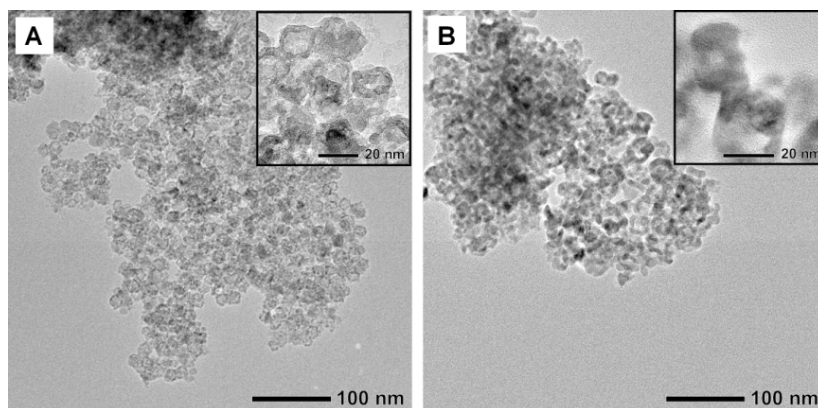
Figure 4.12. Carbon coating the intermediate product formed during the transformation process helped the products retain their shapes. (a) TEM image of polypyrrole-coated nanocages synthesized by the reaction of the Mn_3O_4 nanocrystals with 1 mL of a 1.0 M of aqueous iron(II) perchlorate solution and subsequent reaction with 50 μL of pyrrole at 60 °C for 6 h. (b) TEM image of the polypyrrole-coated nanocages carbonized at 500 °C for 2 h in an argon atmosphere. The insets show corresponding higher-magnification TEM images of the samples.
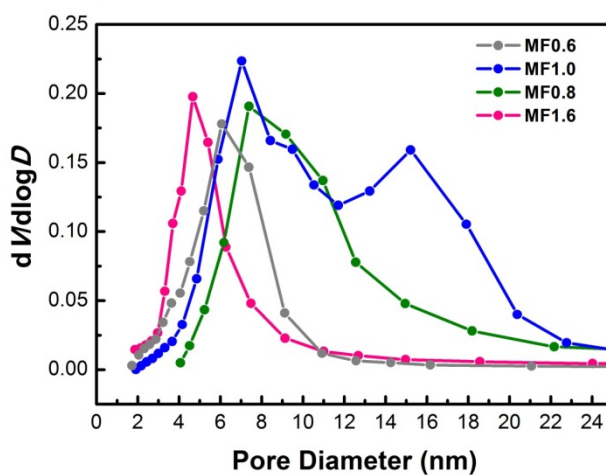
Figure 4.13. Pore size distributions of the (a) MF0.6, (b) MF0.8, (c) MF1.0, and (d) MF1.6 samples calculated using the Barrett-Joyner-Halenda method and the N_2 adsorption data.
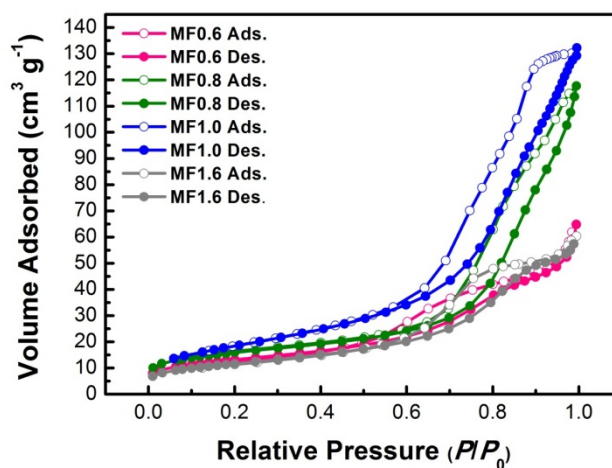
Figure 4.14. N$_2$ adsorption (solid circles) and desorption (hollow circles) isotherms of the (a) MF0.6, (b) MF0.8, (c) MF1.0, and (d) MF1.6 samples.
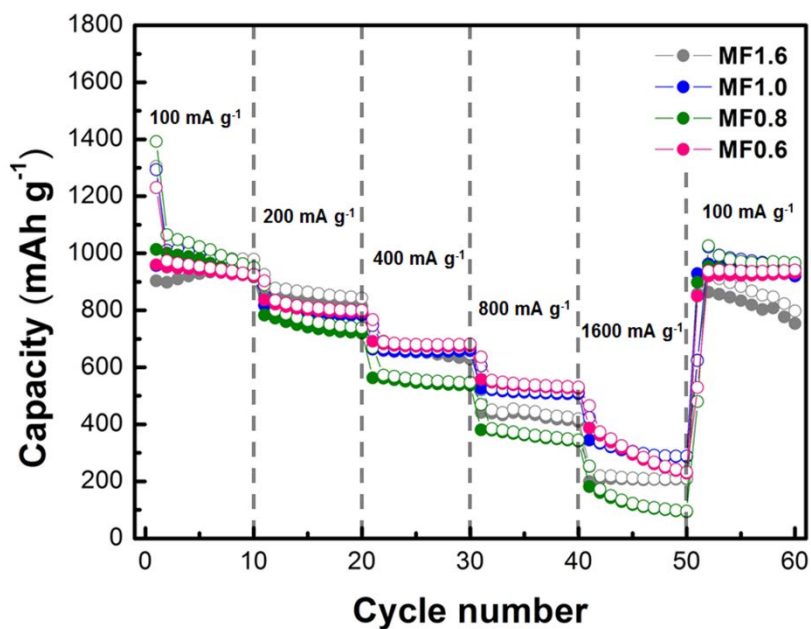
Figure 4.15. Rate performances of the MF0.6, MF0.8, MF1.0, and MF1.6 samples recorded over 50 cycles at variable current densities with the voltage in the range of 3.0 and 0.01 V.

4.2.5. *Ab initio* Density Functional Theory Study

Computational details.

We performed *ab initio* calculations on the basis of the spin-polarized density functional theory (DFT) using a generalized gradient approximation (GGA) within the Perdew-Burke-Ernzerhof (PBE) functional.[29] We used a plane-wave basis set and the projector-augmented wave (PAW) method as implemented in the Vienna *ab initio* simulation package (VASP).[30] We added the Hubbard parameter (GGA+U) to correct the incomplete cancelation of the self-interaction of the GGA.[31] A U value of 5 eV and J value of 1.0 eV were used for both Mn and Fe ion.[32] A plane-wave basis set with a kinetic-energy cutoff of 400 eV and $4 \times 4 \times 4$ Monkhorst-Pack k-point meshes were used to ensure that the total energies converged to less than 5 meV per formula unit (fu). All structures were fully relaxed with ferromagnetic orderings.

Phase stabilities of $Mn_{3-x}Fe_xO_4$ ($0 \leq x \leq 3$)

To investigate the phase stabilities of $Mn_{3-x}Fe_xO_4$ ($0 \leq x \leq 3$), we calculated all the possible Mn/Fe arrangements in octahedral and tetrahedral sites within the unit cell containing using the Cluster-

Assisted Statistical Mechanics (CASM) program.[33] Figure 4.17 shows the DFT formation energies of 153 configurations as a function of the Fe content. The dashed line shows the convex hull of $Mn_{3-x}Fe_xO_4$ ($0 \leq x \leq 3$) when Mn_3O_4 and Fe_3O_4 are considered as the end members. There were several ground states of $Mn_{3-x}Fe_xO_4$ on the convex hull, and these were $Mn_{2.875}Fe_{0.125}O_4$, $Mn_{2.75}Fe_{0.25}O_4$, $Mn_{2.625}Fe_{0.375}O_4$, $Mn_{2.125}Fe_{0.875}O_4$, $MnFe_2O_4$, $Mn_{0.5}Fe_{2.5}O_4$, and $Mn_{0.25}Fe_{2.75}O_4$. Other configurations of $Mn_{3-x}Fe_xO_4$ were also very close to the convex hull and the differences between their formation energies and that of the convex hull were very small. These differences can be easily overcome by thermal energy at room temperature (*ca*. 25 meV). These results indicated that the solid solution between Mn_3O_4 and Fe_3O_4 can feasibly occur at all compositions, a conclusion that was in good agreement with the experimental results.[34]

We checked the oxidation states of Mn and Fe ions in the ground-state structure of Mn_3O_4, $MnFe_2O_4$ and Fe_3O_4 with the spin integration.[35,36] Table 4.1 shows the integrated spin density within the Voronoi volume of each transition metal (TM) ion. This was comparable to a plateau value when the integrated spin density was plotted with a distance from a TM ion core in M_3O_4. The oxidation

state of each TM ion was determined by comparing the integrated spin densities of the TM ions in M_3O_4 (Table 4.1) and the unpaired electron spin count of the TM ions in tetrahedral and octahedral sites (Figure 4.17). Typically, the computed net moments are slightly lower. This is so for oxides owing to the transfer of the moment of the oxygen ions.[35,36] Mn_3O_4, $MnFe_2O_4$, and Fe_3O_4 have normal spinel arrangements in which divalent ions occupy all the tetrahedral sites (A sites) and trivalent ions occupy all the octahedral sites (B sites) as was determined computationally by Szotek *et al.*.[37] The normal spinel structure $MnFe_2O_4$ with all the A sites being occupied by divalent Mn ions and all the B sites being occupied by trivalent Fe ions is 500 meV per f.u. more stable than the inverse spinel structure $MnFe_2O_4$ (A sites: Fe ions, B sites: Mn and Fe ions).

Prediction of average voltages of conversion reactions

The prediction of the exact voltages of anode materials on the basis of the conversion reaction using *ab initio* calculations is not trivial. This is due to the conversion reaction pathways usually being unknown. Nevertheless, the average voltages of the conversion materials can be calculated with the total energy of the involved compounds.[38] The

overall conversion reaction of M_3O_4 can be written as

$$M_3O_4 + 8Li^+ + 8e^- \rightarrow 3M + 4Li_2O$$
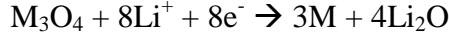
For this conversion reaction, the average voltages can be simply determined by using following equation:

$$\langle V \rangle = \frac{-[4E(Li_2O) + 3E(M) - E(M_3O_4) - 8E(Li)]}{8F}$$

where $E(Li_2O)$, $E(M_3O_4)$, $E(M)$, and $E(Li)$ are the DFT energies of each compound /elemental metal in their ground state structures and F is the Faraday constant.[39] Table 4.2 shows the calculated average voltages of stable $Mn_{3-x}Fe_xO_4$ compounds. These voltages are greater than those determined experimentally during a first discharge. This is because we combined the GGA and GGA+U energies to predict the voltages of the conversion reactions. The GGA methodology is more appropriate for calculating the energies of metallic systems such as Mn and Fe, owing the delocalized electronic states of their d orbital, whereas the GGA+U methodology is more appropriate for calculating the energies of metal oxide compounds such as Fe_3O_4 and Mn_3O_4, owing to their localized electronic states. In order to use the GGA and GGA+U energies together, the energies should be calibrated using a correction term because there is a discrepancy between the GGA and

GGA+U energies.[40] However, the calculated voltages of Mn_3O_4 and Fe_3O_4 are still higher than those determined experimentally using the correction term that was introduced by the Ceder group. This problem is also observed in other conversion reactions.[41] Nevertheless, their relative voltages are reasonable values because these are calculated taking into consideration the differences in the Gibbs free energy for the reduction reaction, which cancels out the artificial terms. After correcting the experimentally determined value of Mn_3O_4, the voltages of Mn_3O_4, $MnFe_2O_4$, and Fe_3O_4 were in good agreement with their experimental counterparts, as shown in Table 4.2. The results of out *ab initio* calculations showed that the average voltages of $Mn_{3-x}Fe_xO_4$ gradually increase with the Fe content, from 0.400 to 0.818 V at $0 \le x \le 3$.
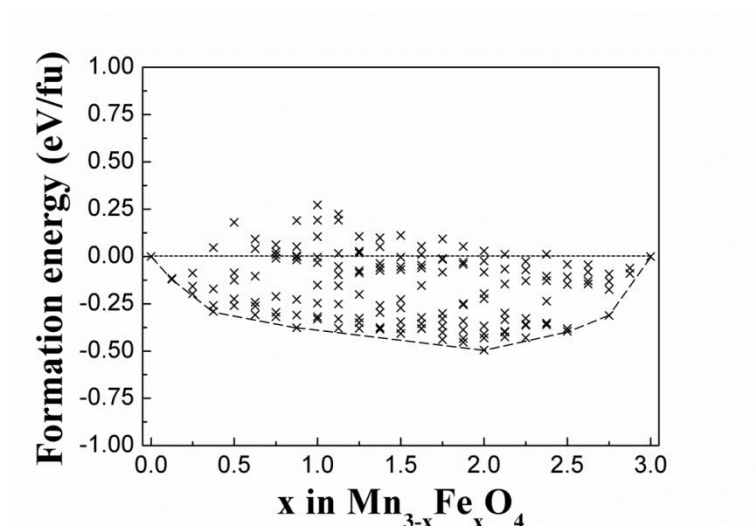
Figure 4.16. The DFT formation energies of the various configurations of $Mn_{3-x}Fe_xO_4$ as a function of its Fe content ($0 \leq x \leq 3$).
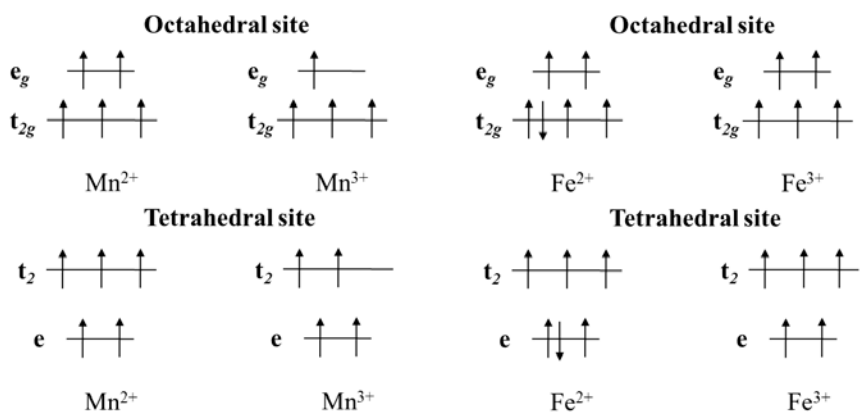
Figure 4.17. Schematics of the energy levels and occupied electrons of Mn and Fe ions in the octahedral site and the tetrahedral site.

Table 4.1. Calculated net moments of the Mn and Fe ions in Mn_3O_4, $MnFe_2O_4$, $Mn_{0.125}Fe_{2.875}O_4$, and Fe_3O_4 and the estimated oxidation states of the Mn and Fe ions.

Net moment (1/2 μm)	Fe_3O_4	Mn_3O_4	$MnFe_2O_4$
Octahedral site	4.19 ($Fe^{3-\delta}$)	4.22 (Mn^{3+})	4.29 (Fe^{3+})
Tetrahedral site	4.08 ($Fe^{2+\delta}$)	4.64 (Mn^{2+})	4.76 (Mn^{2+})

Table 4.2. Calculated average voltages of stable $Mn_{3-x}Fe_xO_4$ compounds. The experimentally reported plateau potentials of Mn_3O_4, $MnFe_2O_4$, and Fe_3O_4 during the first discharge are also presented. The corrected[1] voltages were calculated using the correction term suggested by the Ceder group and the corrected[2] voltages were scaled using experimentally determined values for Mn_3O_4.

Voltage (V)	GGA+U	Corrected[1]	Corrected[2]	Exp.
Fe_3O_4	2.420	1.769	0.818	~0.80
$Mn_{0.25}Fe_{2.75}O_4$	2.364	1.714	0.733	
$Mn_{0.5}Fe_{2.5}O_4$	2.301	1.690	0.699	
$Mn_{0.75}Fe_{2.25}O_4$	2.262	1.654	0.660	
$MnFe_2O_4$	2.225	1.616	0.623	~0.60[42]
$Mn_{2.75}Fe_{0.25}O_4$	2.015	1.575	0.413	
Mn_3O_4	2.002	1.381	0.400	~0.40

4.4 Conclusion

By taking advantage of the simplicity of this chemical transformation method, we were able to open a new and promising route for the development of oxide-based anodic materials that exhibit improved capacities and cyclic stabilities. Furthermore, our method enables the large-scale, low-cost synthesis of a wide variety of nanostructured hollow oxides having various chemical compositions and enhanced functionalities.

4.5 References

[1] Yin, Y.; Rioux, R. M.; Erdonmez, C. K.; Hughes, S.; Somorjai, G. A.; Aliviatos, A. P. *Science* **2004**, *304*, 711.

[2] Son, D. H.; Hughes, S. M.; Yin, Y.; Alivisatos, A. P. *Science* **2004**, *306*, 1009.

[3] Park, J.; Zheng, H.; Jun, Y.-w.; Alivisatos, A. P. *J. Am. Chem. Soc.* **2009**, *131*, 13943.

[4] Zhang, Q.; Wang, W.; Goebl, J.; Yin, Y. *Nano Today* **2009**, *4*, 494.

[5] Peng, Z.; You, H.; Wu, J.; Yang, H. *Nano Lett.* **2010**, *10*, 1492.

[6] Moon, G. D.; Ko, S.; Min, Y.; Zeng, J.; Xia, Y.; Jeong, U. *Nano Today* **2011**, *6*, 186.

[7] Sun, Y.; Xia, Y. *Science* **2002**, *298*, 2176.

[8] Métraux, G. S.; Cao, Y. C.; Jin, R.; Mirkin, C. A. *Nano Lett.* **2003**, *3*, 519.

[9] Sun, Y.; Xia, Y. *J. Am. Chem. Soc.* **2004**, *126*, 3892.

[10] Skrabalak, S. E.; Chen, J.; Sun, Y.; Lu, X.; Au, L.; Cobley, C. M.; Xia, Y. *Acc. Chem. Res.* **2008**, *41*, 1587.

[11] Macdonald, J. E.; Sadan, M. B.; Houben, L.; Popov, I.; Banin, U. *Nat. Mater.* **2010**, *9*, 810.

[12] González, E.; Arbiol, J.; Puntes, V. F. *Science* **2011**, *334*, 1377.

[13] Wang, Z.; Zhou, L.; Lou, X. W. *Adv. Mater.* **2012**, *24*, 1903.

[14] An, K.; Hyeon, T. *Nano Today.* **2009**, *4*, 359.

[15] Piao, Y.; Kim, J.; Na, H. B.; Kim, D.; Baek, J. S.; Ko, M. K.; Lee, J. H.; Shokouhimehr, M.; Hyeon, T. *Nat. Mater.* **2008**, *7*, 242.

[16] Peng, S.; Sun, S. *Angew. Chem. Int. Ed.* **2007**, *46*, 4155.

[17] Yu, T.; Moon, J.; Park, J.; Park, Y. I.; Na, H. B.; Kim, B. H.; Song, I. C.; Moon, W. K.; Hyeon, T. *Chem. Mater.* **2009**, *21*, 2272.

[18] Materials and methods are available as supporting material on Science Online.

[19] Villinski, J. E.; O'Day, P. A.; Corley, T. L.; Conklin, M. H. *Environ. Sci. Technol.* **2001**, *35*, 1157.

[20] Kang, J.-S.; Kim, G.; Lee, H. J.; Kim, D. H.; Kim, H. S.; Shim, J. H.; Lee, S.; Lee, H.; Kim, J. -Y.; Kim, B. H.; Min, B. I. *Phys. Rev. B* **2008**, *77*, 035121.

[21] Lide, D. R. *CRC Handbook of Chemistry and Physics* (CRC Press, Boca Raton, USA, ed. 76, 1978).

[22] Albering, J. H.; Grygar, T. *J. Solid State Electrochem.* **1999**, *3*, 117.

[23] Fetisov, V. B.; Kozhina, G. A.; Ermakov, A. N.; Fetisov, A. V.; Miroshnikova, E. G. *J. Solid State Electrochem.* **2007**, *11*, 1205.

[24] Kim, D. K.; Muralidharan, P.; Lee, H. -W.; Ruffo, R.; Yang, Y.; Chan, C. K.; Peng, H.; Huggins, R. A.; Cui, Y. *Nano Lett.* **2008**, *8*, 3948.

[25] Wang, H.; Cui, L. -F.; Yang, Y.; Casalongue, H. S.; Robinson, J. T.; Liang, Y.; Cui, Y.; Dai, H. *J. Am. Chem. Soc.* **2010**, *132*, 13978.

[26] Kim, H. S.; Piao, Y.; Kang, S. H.; Hyeon, T.; Sung, Y.-E. *Electrochem. Commun.* **2010**, *12*, 382.

[27] Miyata,N.; Ota, H.; Ishikawa, M. *App. Phys. Lett.* **2005**, *86*, 222504.

[28] Kim J.; Kim, S. -W.; Gwon, H.; Yoon, W. -S.; Kang, K. *Electrochim. Acta* **2009**, *54*, 5914.

[29] Perdew, J. P.; Burke, K.; Ernzerhof, M. *Phys. Rev. Lett.* **1996**, *77*, 3865.

[30] Kresse, G.; Furthmuller, J. *Comput. Mater. Sci.* **1996**, *6*, 15.

[31] Anisimov, V. I.; Aryasetiawan, F.; Lichtenstein, A. I. *J. Phys.-Condes. Matter* **1997**, *9*, 767.

[32] Wang, L.; Maxisch, T.; Ceder, G. *Phys. Rev. B* **2006**, *73*, 195107.

[33] Van der Ven, A.; Thomas, J. C.; Xu, Q.; Swoboda, B.; Morgan, D. *Phys. Rev. B* **2008**, *78*, 104306.

[34] Li, Y. H.; Kouh, T.; Shim, I.-B.; Kim, C. S. *J. Appl. Phys.* **2012**, *111*, 07B544.

[35] Gwon, H.; Seo, D.; Kim, S.; Kim, J.; Kang, K. *Adv. Funct. Mater.* **2009**, *19*, 3285.

[36] Seo, D.; Park, Y. -U; Kim, S. -U.; Park, I.; Shakoor, R. A.; Kang, K. *Phys. Rev. B* **2011**, *83*, 205127.

[37] Szotek, Z.; Temmerman, W. M.; Ködderitzsch, D; Svane, A.; Petit, L.; Winter, H. *Phys. Rev. B* **2006**, *74*, 174431.

[38] Li, H.; Balaya, P.; Maier, J. *J. Electrochem. Soc.* **2004**, *151*, A1878.

[39] Mason, T. H.; Liu, X.; Hong, J.; Graetz, J.; Majzoub, E. H. *J. Phys. Chem. C* **2011**, *115*, 16681.

[40] Jain, A.; Hautier, G.; Ong, S. P.; Moore, C. J.; Fischer, C. C.; Rersson, K. A.; Ceder, G. *Phys. Rev. B* **2011**, *84*, 045115.

[41] See "Lithium Battery Explorer Apps" in http://www.materialsproject.org/

[42] Jang, B.; Park, M.; Chae, O. B.; Park, S.; Kim, Y.; Oh, S. M.; Piao, Y.; Hyeon, T. *J. Am. Chem. Soc.* **2012**, *134*, 15010.

Bibliography

1. International Publications

1) **<u>Myoung Hwan Oh</u>**, Nohyun Lee, Hyoungsu Kim, Seung Pyo Park, Yuanzhe Piao, Jisoo Lee, Samuel Woojoo Jun, Woo Kyung Moon, Seung Hong Choi, and Taeghwan Hyeon

   "Large-Scale Synthesis of Bioinert Tantalum Oxide Nanoparticles for X-ray Computed Tomography Imaging and Bimodal Image-Guided Sentinel Lymph Node Mapping"

   Journal of American Chemical Society, **2011**, *133*, 5508-5515.

2) Nohyun Lee, Hye Rim Cho, **<u>Myoung Hwan Oh</u>**, Soo Hong Lee, Kangmin Kim, Byung Hyo Kim, Kwangsoo Shin, Tae-Young Ahn, Jin Woo Choi, Young-Woon Kim, Seung Hong Choi*, and Taeghwan Hyeon

   "Multifunctional Fe_3O_4-TaO_x Core-Shell Nanoparitlcles for Simultaneous Magnetic Resonance Imaging and X-ray Computed Tomography"

   Journal of American Chemical Society, **2012**, *134*, 10309-10312.

3) **<u>Myoung Hwan Oh</u>**, Taekyung Yu, Seung-Ho Yu, Byungkwon Lim, Kyung-Tae Ko, Marc-Georg Willinger, Dong-Hwa Seo, Byung Hyo Kim, Min Gee Cho, Jae-Hoon Park, Kisuk Kang, Yung-Eun Sung, Nicola Pinna, and Taeghwan Hyeon

   "Galvanic Replacemen Reactions in Metal Oxide Nanocrystals"

   Science, submitted.

4) Jae Sung Son, Moon Kee Choi, Mi-Kyung Han, Kunsu Park, Jae-Yeol Kim, Seong Joon Lim, **<u>Myunghwan Oh</u>**, Young Kuk, Chan Park, Sung-Jin Kim, and Taeghwan Hyeon

   "n-type Nanostructured Thermoelectric Materials Prepared from Chemically Synthesized Ultrathin Bi_2Te_3 Nanoplates"

   Nano Letter, **2012**, *12*, 640-647.

2. Internatrional Conferences

1) **<u>Myoung Hwan Oh</u>**, Nohyun Lee, Seung Hong Choi, and Taeghwan Hyeon

   "Large-Scale Synthesis of Bioinert Tantalum Oxide Nanoparticles

for X-ray Computed Tomography Imaging and Bimodal Image-Guided Sentinel Lymph Node Mapping"

Material Research Society (MRS) 2009 Fall Meeting, MRS, Hynes Convention Center, Boston, MA, USA, Nov. 29 - Dec. 4, 2010. (Oral Session)

2) **Myoung Hwan Oh**, Nohyun Lee, Seung Hong Choi, and Taeghwan Hyeon

"Multifunctional Fe_3O_4-TaO_x Core-Shell Nanoparitlcles for Simultaneous Magnetic Resonance Imaging and X-ray Computed Tomography"

4th HOPE meeting, Tsukuba International Congress Center, Tsukuba, Japan, March 7 - 11, 2012. (Poster Session)

2. Domestic Conferences

1) **Myoung Hwan Oh**, Nohyun Lee, Seung Hong Choi, and Taeghwan Hyeon

"Large-Scale Synthesis of Bioinert Tantalum Oxide Nanoparticles for X-ray Computed Tomography Imaging and Bimodal Image-

Guided Sentinel Lymph Node Mapping"

43rd Korean Society of Industrial and Engineering Chemistry Spring Meeting, International Convention Center JEJU, Jeju, Korea, May 11 - 13, 2011. (Oral Session)

2) **<u>Myoung Hwan Oh</u>**, Nohyun Lee, Seung Hong Choi, and Taeghwan Hyeon

"Large-Scale Synthesis of Bioinert Tantalum Oxide Nanoparticles for X-ray Computed Tomography Imaging and Bimodal Image-Guided Sentinel Lymph Node Mapping"

Korean Chemical Society Summer Symposium for Material Chemistry, Hillside hotel, Yongin, Korea, June 23 - 24, 2011. (Oral Session)

3) **<u>Myoung Hwan Oh</u>**, Nohyun Lee, Seung Hong Choi, and Taeghwan Hyeon

"Large-Scale Synthesis of Bioinert Tantalum Oxide Nanoparticles for X-ray Computed Tomography Imaging and Bimodal Image-Guided Sentinel Lymph Node Mapping"

Pioneer Nano Seoul Forum, Seoul National University, Korea,

Nov, 1, 2011. (Poster Session)

3. Patent

Taeghwan Hyeon, **<u>Myoung Hwan Oh</u>**, Surface-Modified Tantalum Oxide Nanoparticles, Method for Preparation Thereof, and Contrast Agent for X-ray Computed Tomography and High-k Dielectric Film Using the Same (2010.02.23)

4. Press

"A better imaging agent for heart disease and breast cancer"
ACS News Service weekly press pack, April, 27, 2011
American Chemical Society introduced Tantalum oxide nanoparticles studied on my first research as a promising X-ray contrast agent for practical diagnosis of heart disease and breast cancer. This was released on various international science journals.

4. Expeience in Oversea

Visiting Researcher (Supervisor: Pro. Nicola Pinna), Department of Chemistry and CICECO, Univerisity of Aveiro, Portugal, July 15 - Aug. 20, 2011.

초 록

최근 산화물 나노입자의 용액기반 합성법에 있어 괄목할 만한 진전이 있었다. 입자의 크기, 구조, 모양, 성분비를 조절하는 합성 가용성이 대폭 증대됨에 따라 벌크에 비해 매우 다양하고 독특한 성질을 가진 나노입자를 생산할 수 있게 되었다. 그러는 동안에 졸-겔 화학은 금속 전구체를 금속 산화물로 전환시키기에 가장 유용하고 필수적이며 모든 금속에 적용이 가능한 방법으로서 인식되어왔다. 그러나 미세구조와 더불어 나노입자의 크기/모양 의존적 성질을 정밀하게 제어하기 위해서는 졸-겔 공정을 거치는 동안 화학적, 물리적, 또는 기술적인 조율이 필요하다. 예를들어 나노입자의 성장속도를 제어하기 위해 무수화 졸-겔 화학이 제시되었고, 양친성 분자를 유기조립체나 구조제어제로 사용하는 연질주형법은 나노입자의 성장을 나노규모에 제한시키기 위해 도입되었다.

그동안 균일한 나노입자를 합성하는 연구 분야에서 수계 졸-겔 반응은 회피되었다. 물에 의해 일어나는 무기중합반응은 비가역적인 응집현상이나 성장반응이

‘올리고’ 물질에 정체되는 현상을 막기에는 너무 빠르기 때문이다. 그래서 무수화 졸−겔 반응에 의한 합성이 주도적으로 진행되었고, 균일성과 대량생산성이 우수하였다. 그러나 수계 졸−겔 반응은 산화물 나노입자를 형성시키는데 있어 더욱 쉽고 친환경적일 뿐만 아니라 저온, 저비용 공정이 가능하게 한다. 물의 독특한 용매화 능력은 균질한 합성용액의 형성과 높은 수율의 이온결정을 얻기에 유리하다. 게다가 수용액에서는 산과 염기 또는 용존 산소에 의한 산화/환원 전위의 조절이 가능한데, 이는 금속산화물 나노입자의 침전과 용해를 결정하는 중요한 요소이다. 무수화 졸−겔 화학에서 필수인 금속−유기 복합체의 역할이 반투과성 연질 주형에 의해 물에서도 활용될 수 있다. 이러한 멤브레인은 여러가지 형태의 주형이 가능하고, 온화한 반응조건에서 간단한 방법으로 생산할 수 있으며, 결과물에 손상을 입히지 않고 쉽게 제거할 수 있는 장점이 있다. 미셀, 베지클, 액정, 에멀젼 방울, 리피드 나노튜브와 같은 여러가지 종류의 유기 분자 조립체는 단단한 물질의 성장이나 배열을 조절하기 위해 주형이나 구조형성제로 사용되어왔다. 연질 주형은 반투과성과 반강직성으로 인해 나노크기를 유지하면서 입자들의 이종퇴적 현상이나 용해 현상을 유발시키기에 매우 적합하다. 특히, 그

191

나노크기의 독특한 모양과 성질을 가진 주형들로 인해 비평형 구조의 기능성 나노물질들이 생산되었다. 결과물인 다공성구조, 할로우구조, 코어–쉘구조, 요크–쉘구조, 이중접합구조는 촉매와 에너지, 생체의약품 분야에서 각광받는 후보물질이다. 우리는 연질 주형을 이용한 졸–겔 방법을 이용한 새로운 기능성 금속 산화물 나노입자의 합성을 연구하였고, 다중조영제와 리튬이온전지의 음극으로서 유용한 물질들을 찾아내었다. 산화탄탈륨과 산화탄탈륨/산화철 코어–쉘 나노입자를 마이크로에멀젼 방법으로 합성하였고 X–ray 단층영상과 자기공명영상에 다중조영제로 응용하였다. 그 결과 훌륭한 촬영 효과와 생체 안정성을 확인하였다. 역베지클 용액 내에서 금속산화물 나노입자와 이종 금속 이온 간의 갈바닉 교환 현상을 최초로 관찰하였다. 결과물은 리튬이온 전지에서 음극활물질로 사용되었다. 이론 값에 가까운 높은 용량과 충/방전 안정성을 나타내었다. 본 연구에서, 마이크로에멀젼과 역베지클 용액에서 수계 졸–겔 반응으로 합성 된 모든 다기능성 산화물 나노입자들은 간단하고 온화한 조건에서 대량생산 되었다.

주요어: 졸–겔 합성, 금속산화물 나노입자, 연질주형, X–ray

CT 조영제, 자기공명촬영, 리튬 이온 전지.

학번: 2010−31327